Magnetic Pose Estimation and Robotic Manipulation of Magnetically Actuated Capsule Endoscopes

By

Addisu Zerihun Taddese

Dissertation

Submitted to the Faculty of the

Graduate School of Vanderbilt University

in partial fulfillment of the requirements

for the degree of

DOCTOR OF PHILOSOPHY

in

Electrical Engineering

August 10, 2018

Nashville, Tennessee

Approved:

Ákos Lédeczi, Ph.D.

Pietro Valdastri, Ph.D.

Keith L. Obstein, M.D., M.P.H., F.A.S.G.E., F.A.C.G.

D. Mitch Wilkes, Ph.D.

Xenofon Koutsoukos, Ph.D.

Copyright © 2018 by Addisu Zerihun Taddese
All Rights Reserved

ACKNOWLEDGMENTS

First, I would like to thank God for giving me the capacity and strength to pursue this endeavor. Without His help through many answered prayers, this would not have been possible. To Him be the glory.

I owe a great deal of gratitude to several people that have helped, mentored, and encouraged me during my time at Vanderbilt. First, I want to thank Professor Ákos Lédeczi, my advisor and chair of my dissertation committee, for always looking out for my interests and my future as he advised and guided me throughout my tenure at Vanderbilt. His patient, but persistent, nudging is the only reason I was able to complete this dissertation. I am also grateful for Professor Pietro Valdastri and Dr. Keith Obstein who directed the lab in which I did my research during my dissertation. Specifically, Professor Valdastri co-advised me for part of my dissertation and taught me the underpinnings of academic research. His style of guidance struck a balance between giving sufficient research directions while providing enough independence for me to come up with new ideas. When he left for Leeds, Dr. Obstein took the helm and continued to lead the lab despite his busy schedule as a gastroenterologist. For that, I am deeply grateful. Dr. Obstein's immense medical expertise was valuable in providing medical insight, understanding and context to problems we were trying to solve at the STORM Lab.

Thanks to the following funding agencies for their support that made my research possible: the National Institute of Biomedical Imaging and Bioengineering, USA of the National Institutes of Health under award no. R01EB018992, the National Science Foundation, USA under grant no. CNS-1239355 and no. IIS-1453129, the National Science Foundation Graduate Research Fellowship Program under grant no. 1445197.

I would not be at Vanderbilt if it was not for Professor Alan Peters. Thank you for believing in me and pushing to get me accepted into the school. Thank you to

Professor Julie Adams for advocating for me and giving me wise advice when I had to make a difficult decision about my future research direction.

I am grateful for all the past and present members of the STORM Lab with whom I had the privilege of working. I am thankful for their friendship, their help in research and the fruitful discussions. I learned a lot from these conversations. I am especially grateful for Piotr Slawinski for his close collaboration on the MAC project. His help in brainstorming ideas, writing papers, and running experiments was invaluable. I will always remember his kindness and never-failing willingness to help even without being asked.

To our small group, thank you for the love, friendship, encouragement, and prayers throughout the last few years.

I am thankful for the group of friends that we affectionately call "Akos's students" for their friendship. I highly value our time together cultivating our passions for research, programming, Linux and all the tools of our craft.

I am deeply grateful for my family and feel extremely blessed to have their love, encouragement, and support. Thank you for your never-ceasing prayers, and your constant willingness to listen and sympathize with my grad school difficulties. Spending time with you always gave me perspective when things were tough.

And finally, and most importantly, I want to express my deepest gratitude for my wife, Andrea. She has been the source of my joy and strength throughout this dissertation. She patiently reminded me of the value of my work when I lost perspective. When, at times, I was overwhelmed with all that needed to be done, hers was the voice of calm. Her help in organizing my thoughts, my tasks and my time when writing this dissertation was invaluable. The fact that I can have technical conversations with her about my research was always a source of amazement. In all of this, she made sure that we carved out time for ourselves, friends and family.

TABLE OF CONTENTS

Page

LIST OF TABLES

Table Page

LIST OF FIGURES

LIST OF ABBREVIATIONS

ADC analog to digital. 11, 142

AMR Anisotropic Magnetoresistive. 51, 52, 55–57, 142

AOA angle of arrival. 45, 142

CE capsule endoscope. x, xi, 6, 7, 9, 15, 23–32, 34–42, 44–46, 54–56, 58, 63, 105, 106, 139, 142

CFM constraint force mixing. 122, 142

CRC colorectal cancer. 2, 142

DOF degrees of freedom. 12, 34, 35, 38–41, 51, 53–56, 58–60, 65, 86, 98, 107, 108, 110, 111, 114, 119, 128, 142

EPM external permanent magnet. xii–xiv, 7, 11, 13, 55, 60, 65–75, 77, 81–83, 86, 88, 89, 92–102, 104–109, 114, 118, 119, 121, 125, 132, 135, 137, 141, 142

ERP error reduction parameter. 122, 142

FDA Food and Drug Administration. 23, 141, 142

GI gastrointestinal. 1, 2, 6, 23, 25, 29, 32, 33, 38, 41, 45, 46, 50, 106, 139, 142

IBD inflammatory bowel disease. 4, 142

IMU inertial measurement unit. xii, 12, 68, 86, 88, 91, 142

IPM internal permanent magnet. 11, 12, 56, 59, 92, 142

LCP linear complementarity problem. 122, 142

LM Levenberg Marquardt. 51–54, 58, 60, 142

MAC Magnetically Actuated Capsule. x, xii, 9, 11–13, 63, 87, 106, 111, 124, 137, 139–142

MPC model predictive control. 141, 142

MRI magnetic resonance imaging. 36, 37, 40, 46, 142

NdFeB Neodymium-Iron-Boron. 11, 37, 86, 89, 142

ODE Open Dynamics Engine. 122–124, 142

PET positron emission tomography. 46, 142

PI proportional-integral. 112, 113, 142

RF radio frequency. 45–47, 142

ROS Robot Operating System. 121, 123, 133, 142

RSSI received signal strength indicator. 45, 46, 142

SMA shape memory alloy. 26, 27, 142

TOA time of arrival. 45, 142

WCE wireless capsule endoscope. 24, 142

WDLS weighted damped least-squares. 114–117, 142

CHAPTER 1

Introduction

It is well established that writing instruments such as the pen and paper are extensions of the human memory and cognition system. These technologies allow one's ever evolving thoughts to be externalized so as to relieve the burden of memory. Machines on the other hand can be thought of as extension of the human motor system. They allow us, humans, to do things that require energy and accuracy above our natural abilities. These two notions are combined with intelligent robots which can be programmed with the logic and algorithms that represent human memory and cognition and execute tasks with high precision tirelessly.

Robots have found widespread use in industrial settings since the 1960s. They have been used to automate manufacturing leading to increased productivity and precision. Moreover, jobs that require exposure to harmful conditions for humans are increasingly being replaced by robots. In the world of medicine, robotic systems such as the Da Vinci by Intuitive Surgical have enabled highly precise surgeries by utilizing motion scaling and tremor filtering technologies. Truly remote widespread surgeries are now in the realm of possibility, which are desperately needed in order to improve patient outcomes and extend the reach of modern medicine to rural areas around the world. In the same token, other areas of medicine stand to benefit from robotic automation. One such area is gastrointestinal (GI) endoscopy, where physicians visually explore the GI tract for diagnosis and treatment. Although still in its early stages, researchers have demonstrated that robotic systems have the potential to assist physicians in performing endoscopies. A variety of robots have been developed to augment the use of conventional endoscopes by providing better control for manipulation and autonomous locomotion through the GI tract [178].

1.1 Clinical Motivation

The large intestine, or colon, is known for diseases such as colorectal cancer (CRC), Ulcerative Colitis (UC) and Crohn's disease (CD). In particular, cancers of the GI are among the three leading causes of death in many parts of the world [134, 157, 66]. These diseases are commonly diagnosed using GI endoscopy where a combination of visual inspection and biopsy analysis is performed by physicians. For diseases such as CRC, early screening using colonoscopy can be critical to survival—the five year survival rate of colon cancer detected in its early stage is 90% but drops to 5% if detected at its late stage [134, 165]. Therefore, screening using colonoscopy is highly recommended by physicians.

Figure 1.1: Example of a conventional flexible endoscope.

The conventional device in common use today for such screenings is called the flexible endoscope (Figure 1.1). Even though the word "flexible" appears in the name, it is only there to emphasize the difference in rigidity compared to prior endoscopes that were completely rigid tubes [54]. The current standard flexible endoscope is a semi-rigid tube of about 180 cm in length. Its rigidity is required in order to transmit enough force and torque from the base of the instrument (from which it is operated) to the tip, which is inserted into the patient. The rigidity has a negative side effect

of causing tissue stretching and a phenomenon called "looping" where inserting more of the instrument from the base side does not advance the tip more proximally along the colon. Instead, as shown in Figure 1.2, the tube of the endoscope starts forming a loop that stretches and potentially perforates the colon wall. If the wall is perforated,

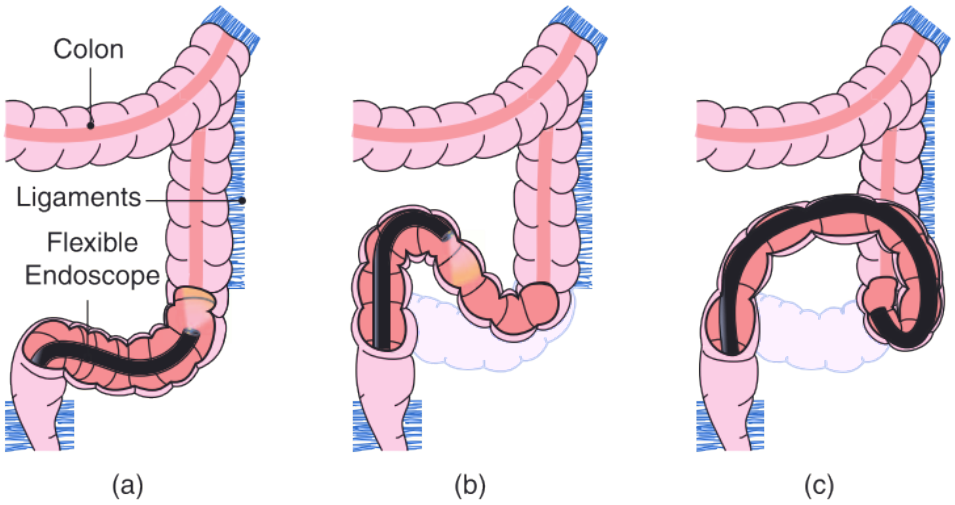

Figure 1.2: Drawbacks associated with the rigidity of endoscopes. (a) Ideal scenario where endoscope is following the path of the lumen. (b) Tissue stretching as the endoscope relies on the resistance force of the colon wall to negotiate turns. (c) Occurrence of "Looping" where inserting more of the instrument does not advance the tip more proximally along the colon. *Reproduced with permission from [88] © 2010 IEEE.*

it could lead to the leakage of fecal material into other nearby organs (peritoneal soilage), resulting in severe complications [110]. On the other hand, stretching of the colon wall is one of the causes of pain for people that get colonoscopies. To avoid this pain people either avoid getting colonoscopies altogether or opt for sedation. An estimated 22 million people in the United States choose to avoid colonoscopies partly due to the perceived pain with which it is associated [18]. For those who heed the recommended screenings and get colonoscopies, sedation is common. Sedation, however, can cause complications for certain patients. A 2016 study reported a 13 % increase in the risk of complications within a 30 day period after colonoscopy for patients undergoing colonoscopy with anesthesia services [174]. While this percentage

is modest, for sufferers of diseases such as inflammatory bowel disease (IBD), where frequent colonoscopies are necessary, the chance of getting a complication increases dramatically over the course of their lifetime.

In order to increase participation in screening procedures and reduce the use of sedation, the pain and discomfort associated with endoscopy needs to be mitigated. This limitation of endoscopy is primarily caused by the actuation and navigation mechanisms of the flexible endoscope, which have made little technological progress since their introduction [164]. The state of the art before the invention of the flexible endoscope was a device composed of a chain of lenses resulting in a rigid tube. Physicians using this device could only examine organs that are accessible via a straight line of sight. A new era in gastroenterology was marked when the first flexible endoscope was introduced in 1954 by H. H. Hopkins [54, 10]. The flexibility was achieved by using a bundle of very thin fiber glass rods arranged such that light could be transmitted with marginal losses. Since then, the technological advances in the device have mainly been in improving illumination and image quality. Great strides have been made since the 1950s with current endoscopes comprising bright LEDs and miniature cameras at the tip with HD and ultra HD (4k) resolutions. Additional sensors such as narrow band imaging and Endoscopic Ultrasound (EUS) have also been developed to improve diagnostics. The actuation and navigation mechanisms, however, have remained by and large the same. The current mode of operation of the device involves the physician performing a combination of twisting and pushing to advance the endoscope while watching the video from the camera on a display monitor. Angulation of the tip is similarly performed by operating the knobs (angulation knob in Figure 1.3) on the handle of the endoscope. In order to turn a corner, the physician would angulate the tip to point in the direction of the lumen and push against the colon wall to bank the endoscope. This, in turn, causes tissue stretching.

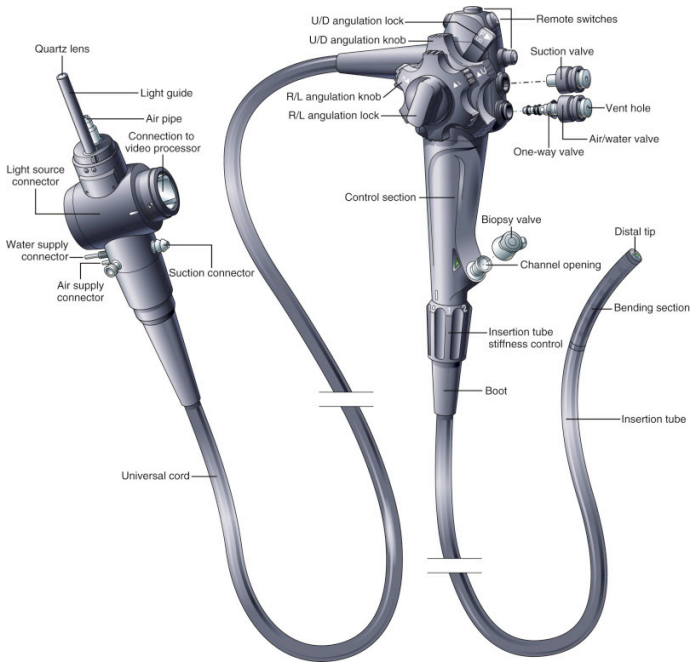

Figure 1.3: Diagram showing the basic components of a conventional flexible endoscope. *Reproduced with permission from [47] © 2011 Elsevier.*

It is natural to expect that highly experienced endoscopists can perform endoscopies with much less pain and discomfort for the patient when compared with novices. However, several years of training is required to master endoscopy due to the difficulty of navigating the colon that is exacerbated by the counter intuitive user interface. This is another limitation that needs to be addressed in order to expand the reach of colonoscopy screenings.

Several research and commercial entities are investigating new devices and systems that reduce discomfort and tissue damage while increasing ease of use for the physician. The Aer-O-Scope system (GI View Ltd., Ramat Gan, Israel), for example, uses CO_2 pressure gradients to advance a custom endoscope constructed with an inflated balloon at each end of the endoscope [169]. In a clinical study, the Aer-O-Scope was shown to be skill independent and less likely to cause tissue damage due its advancing mechanism and electronic pressure regulation. However, since it is a diagnostic only device, it does not have an instrument channel. Another system, the

Endotics, has a locomotion mechanism inspired by inch worms. The locomotion is achieved by a cyclic sequence of steps where proximal and distal clampers are used to anchor the device when its flexible body is shrunk or elongated. In a clinical trial, the device was compared to a conventional endoscope where the metric was the rate of cecal intubation (reaching the cecum) [161]. While the system showed promise in terms of reduced patient discomfort and autonomous locomotion, cecal intubation and procedure times were significantly better with the conventional endoscope.

Yet another approach that has been enabled by recent advances in miniaturization technology is the development of capsule endoscopes (CEs). CEs are perhaps the least invasive alternative to the conventional endoscope. While they still require GI preparation, patients are not sedated and can carry on their regular tasks while the CE traverses through their GI. The motion of CEs relies on peristalsis, the natural contraction and relaxation of the GI necessary to transport food elements. CEs take pictures as they move along the GI, which are later assembled to create a video for the physician to examine. A few limitations prevent CEs from being the ideal alternatives to conventional endoscopy. One major limitation is that they are passive. The physician has no control over the position and orientation of the capsule as it moves. Thus, there are no means for further investigation of a suspicious area. Another limitation is that, without an instrument channel, it is impossible to take biopsies or perform therapy. As this is a common occurrence for colonoscopy, the physician has to fall back to the conventional endoscope to perform these activities.

1.2 Magnetic Capsule Endoscopy

In order to mitigate these limitations, researchers are investigating the use of magnetic fields as means for wirelessly transmitting forces and torques that in turn translate and manipulate capsule endoscopes. In this dissertation, one specific system that uses this approach is studied. The system shown in Figure 1.4, which will be

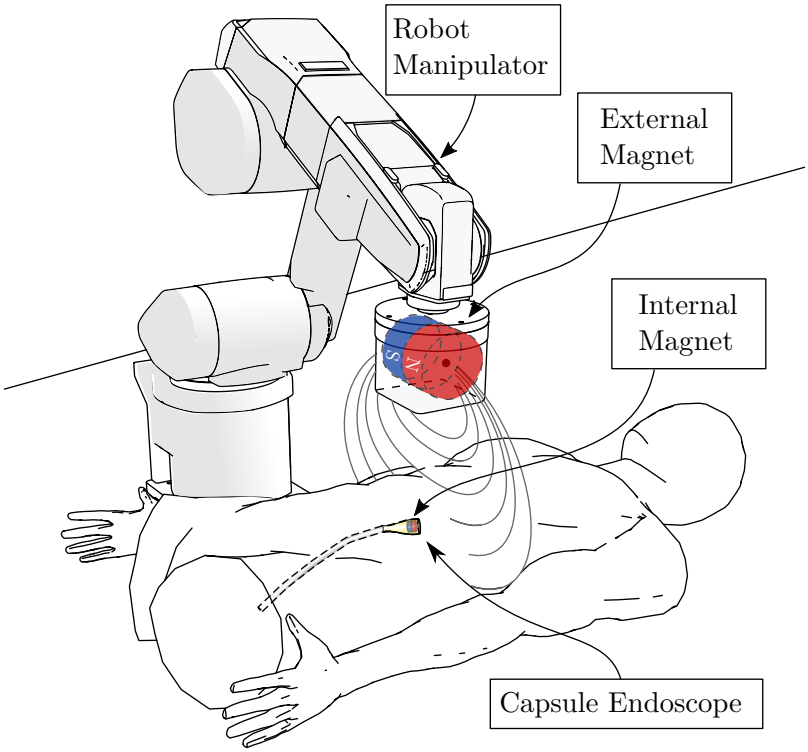

Figure 1.4: Schematic of Magnetic Capsule Endoscopy.

described in more detail in Chapter 2, consists of a soft-tethered capsule that contains a small permanent magnet and an external actuating permanent magnet held by a robotic manipulator. The external permanent magnet (EPM) is used to remotely and wirelessly manipulate the position and orientation of the capsule endoscope thereby overcoming the passive locomotion limitations of CEs while the soft-tether is used to provide an instrument channel through which the physician can perform biopsies and various therapies. The soft-tether also enables the use of high quality video cameras as opposed to the still pictures available in current CEs. Other components include electrical connection so as to not depend on batteries, a channel for water, used for irrigation and cleaning the camera, and gas for insufflation. Since the tether is soft, pushing from the base of the capsule endoscope is not a feasible means of locomotion. Instead, magnetic attraction is used to advance the capsule forward in

a manner akin to front wheel drive. We hypothesize that this would eliminate the looping phenomenon mentioned earlier.

Due to the counter intuitive nature of magnetic field interactions, it is difficult to successfully manipulate the endoscope by manually positioning the actuating magnet, although it has been tried previously [16, 22]. Instead, a robotic arm is used, which has several added benefits:

- Precise motion: The robot can respond to sensory feedback on the pose (position and orientation) of the capsule to correct for any deviations from desired motion.
- Remote operation: The use of the robot opens up the possibility of using the system in a truly remote fashion where the physician and the patient can be in separate locations.
- Physician assistance: The robot can assist the physician during a procedure. Examples of these include automation of repetitive tasks such as retroflexion and stabilization of the capsule endoscope while performing other tasks such a taking biopsies via the tool channel
- Positive patient perception: For some patients, the involvement of robotics technology might remove the stigma associated with conventional endoscopies.

1.3 Contributions

The contributions described in this dissertation focus on two fundamental problems in robotically guided magnetic capsule endoscopy. The first problem pertains to obtaining accurate pose estimation of the capsule inside the patient relative to the actuating magnet. This is required in order compute the appropriate pose of the actuating magnet that would induce the desired forces and torques on the capsule. Since the capsule is inside the patient, methods that do not rely on line of sight must

be used. Imaging modalities such as X-rays and CT scans can be used, but they expose the patient to unnecessary radiation, in the case of X-rays, and the update rates are too slow in CT scans for interactive or real-time control. Here, we examine the possibility of using magnetic fields for pose estimation as it requires no line of sight and can produce pose estimates at interactive rates. While many types of magnetic pose estimation exist, schemes that utilize the same source of magnetic field already present in the system are ideal.

The second problem has to do with using the computed pose estimates as sensory feedback to compensate for deviation of the capsule's pose from the desired or commanded pose, thus achieving closed-loop operation. The solutions to this problem form the algorithmic building blocks for the development of a magnetic guidance system with an intuitive tele-operation interface. Open-loop control with a robot was attempted in [4], but the results showed that the procedure took significantly longer to complete than using a conventional endoscope. Therefore, since tele-operation is the overarching goal, closed-loop control in this context must be efficient so as to operate at interactive or real-time rates.

1.4 Organization of Dissertation

The dissertation is organized as follows. A system description of the Magnetically Actuated Capsule (MAC) is first given in Chapter 2 to provide the context in which the contributions of the dissertation are implemented. Then a survey of related systems is given Chapter 3 highlighting the various approaches pursued by other research groups and commercial entities to improve the state of the art in traditional endoscopy, capsule endoscopy, and magnetic guidance. Chapters 4 and 5 discuss the contributions of this dissertation in pose estimation and closed-loop control for magnetically actuated CE, respectively. Finally, conclusions and directions for future work are given in Chapter 6.

CHAPTER 2

The MAC: Magnetically Actuated Capsule

Since this dissertation is based on the implementation of various technologies for the Magnetically Actuated Capsule (MAC), we provide a description of the system here.

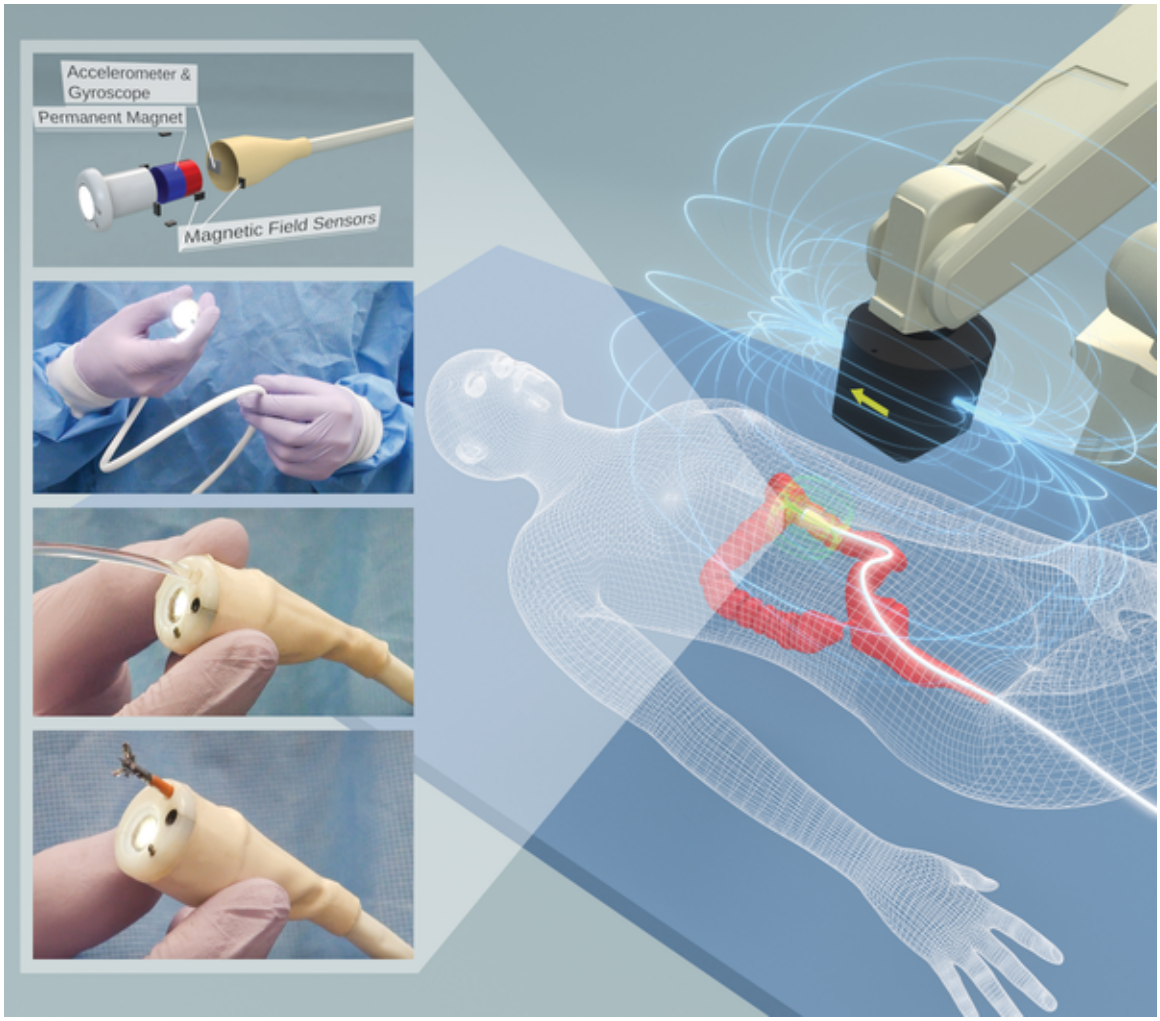

Figure 2.1: The Magnetically Actuated Capsule System.

2.1 System Overview

The Magnetically Actuated Capsule (MAC) system consists of a soft-tethered capsule, a robot manipulator, and a control system with a user interface. It is inspired by the magnetic-air-capsule developed by Valdastri et al. [164] with a design that preserves the capabilities of traditional endoscopes: vision, illumination, passage of endoscopic tools, irrigation and insufflation. The system is mainly designed for applications in the colon as an alternative for colonoscopy. With an internal permanent magnet (IPM) embedded in the capsule and an external permanent magnet (EPM) carried by a robot manipulator, the MAC forms a direct propulsion magnetically actuated system. In its current state, the system is controlled by a gastroentrologist who uses the user interface to control the end effector motion of the robot. The EPM, being attached to the end effector of the robot, moves accordingly and its motion induces forces and torques on the capsule. A schematic of system can be seen in Figure 2.1.

2.2 Subsystem 1: Capsule

The capsule (20 mm diameter, 22 mm length) as shown in Figure 2.2a has a soft-tether that enables functionalities that are commonly found in a traditional endoscope such as vision, illumination, insufflation, irrigation and the passage of endoscopic tools for biopsy and administration of therapy. The soft-tether is also used as a channel for electrical wires connecting the internal sensors of the capsule to a signal acquisition unit. The capsule itself contains a small axially magnetized cylindrical Neodymium-Iron-Boron (NdFeB) permanent magnet (N52 grade, 11.11 mm diameter and length, D77-N52, K&J Magnetics, USA) with a magnetic remanence of 1.48 T housed in a 3D printed enclosure as shown in Figure 2.2b. An analog to digital (ADC) converter (AD7689, Analog Devices) is used to convert the analog output of the Hall sensors

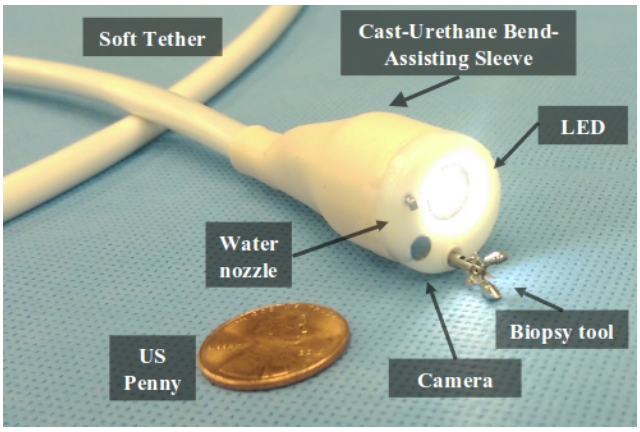

(a) Functionalities of the MAC.

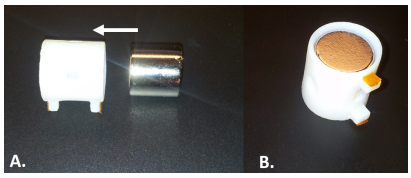

(b) The axially magnetized cylindrical magnet is housed in a 3D printed enclosure.

Figure 2.2: The MAC soft-tethered capsule.

(A1391, Allegro Microsytems) to 16-bit digital values. The inertial measurement unit (IMU) (LSM330DLC, ST Microelectronics) is composed of an accelerometer and a gyroscope, both of which are 3-axis. The sensors and the ADC are mounted on a flexible circuit that is wrapped around the IPM as shown in shown in Figure 2.3. The Hall sensors are placed around the magnet so as to approximate two triaxial Hall sensors separated by a constant distance. Their location is also strategically chosen to ensure that they are not saturated by the magnetic field from the internal magnet.

2.3 Subsystem 2: Robotic Manipulator

The external permanent magnet (N52 grade, 101.6 mm diameter and length, ND N-10195, Magnetworld AG, Germany) that couples with the internal capsule magnet is mounted on the end effector of an industrial 6 degrees of freedom (DOF) Mitsubishi robot (RV-6SDL, Mitsubishi, Inc., Japan). The robot is controlled joint position mode using the Robot Operating System [120].

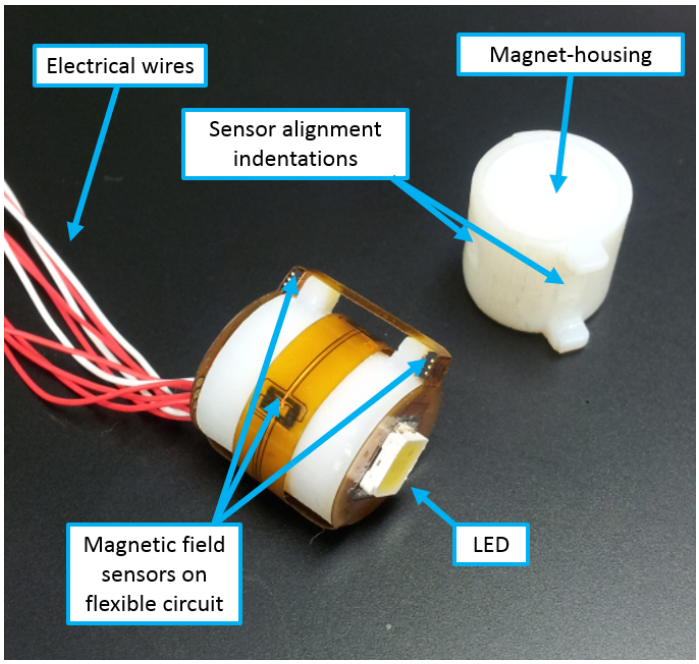

Figure 2.3: The magnetic field sensors and other electronic components are mounted on a flexible circuit that is wrapped around as the magnet housing.

2.4 Subsystem 3: Controller

The controller consists of the PC, user interface, software, and data interfacing components of the system. The PC runs the Linux operating system and various ROS nodes that work in concert to collect sensor data, run localization and control algorithms and visualize the state of the system. The input user interface is a 3D mouse (SpaceMouse Pro), which connects to the PC via USB and provides translational and rotational control of the EPM that is attached to the end effector of the robot manipulator. The data interface communicates with the capsule's sensors via Serial Peripheral Interface and relays the information to the PC via USB.

2.5 Subsystem 4: Pose Estimation System

The MAC uses a real-time magnetic pose estimation system developed by Di Natali et al. [34]. The algorithm solves the inverse problem of finding the position

given magnetic field readings by searching through a look-up table that maps positions in cylindrical coordinates to magnetic field vectors. Due to magnetic symmetry of cylindrical magnets, the azimuthal component of the magnetic field is identically zero reducing the look-up table to a plane. Additionally, the quadrants of the look-up table are reflections of each other further reducing the look-up table to a single quadrant. The details of the algorithm can be found in Section 3.4.3.3.

CHAPTER 3

Related Systems

3.1 Improving Conventional Endoscopes

Work on improving the current state of endoscopes is taking place in multiple avenues. We organize these avenues in three overarching categories although some systems have overlapping categories. The first set of systems aim to improve upon the conventional endoscope with electromechanical structures designed to work with existing endoscopes. The second category includes systems that are significant modifications of the conventional endoscope, and thus, are considered endoscopic systems of their own. Finally, the last category consists of systems that utilize capsule endoscopes (CEs).

In this chapter, we highlight notable systems from each category but delve deeper in the third category where magnetically actuated capsules are included. More extensive reviews can be found in [156, 165, 103, 139, 136, 137, 140, 24, 178].

3.1.1 Electromechanical Control of Conventional Endoscopes

These systems work in tandem with existing endoscopes and generally provide a better user interface for the physician. As Figure 3.1 shows, with a conventional endoscope, a physician controls the bending of the tip of the endoscope by rotating the control wheels at the base of the endoscope. To advance the tip forward, the same physician manually pushes the endoscope shaft. This control interface is cumbersome and contributes to the difficulty of using endoscopes. It has also been associated with musculoskeletal problems as evidenced by the increased complaints of physicians in this field compared to other specialties [133]. However, while improving the user interface is beneficial to the physician, these new systems do not directly mitigate

Figure 3.1: The user interface of the conventional endoscope. A physician controls the bending of the tip of the endoscope by rotating the control wheels at the base of the endoscope.

the issues related with patient comfort. Some examples from this category include the Robotic Steering and Lumen Centralization (RS-ALC) [119, 123], the Endoscopic Operating Robot (EOR) [79] and the Invendoscope [122].

Robotic Steering and Lumen Centralization

In this system (Figure 3.2), the control wheels of a conventional endoscope are attached to a remote drive unit that can be controlled with a joystick [119, 123]. The motion of the tip of the endoscope, in response to the manipulation of the joystick, is displayed on a screen for visual feedback. In addition, a computer vision algorithm was used to determine the center of the lumen by detecting dark regions of the endoscopic image and provide a means for automatically steering the tip to the identified center. A randomized study with a bench-top colon model showed that the system greatly helped novices in reaching the cecum, but had much lesser benefit for experts.

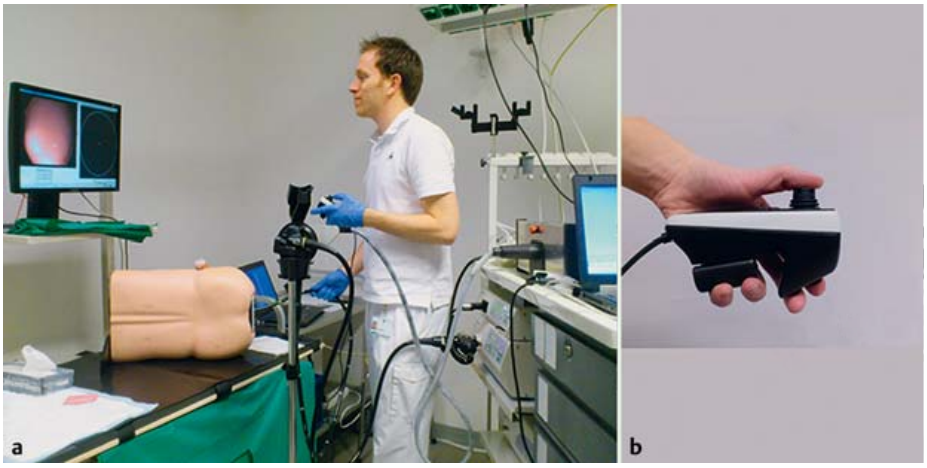

Figure 3.2: (a) The Robotic Steering and Lumen Centralization being used in an experiment. (b) Joystick user interface. *Reproduced with permission from [119] © 2015 Georg Thieme Verlag KG.*

Endoscopic Operating Robot

Using a joystick and a rotating handle, instead, this system aims to provide a way to operate a conventional endoscope using one hand [79]. This would allow the physician to perform other tasks. The system (Figure 3.3) consists of a master unit with a user interface that has been instrumented with force sensors and a slave unit in which a conventional endoscope can be secured. The force sensors are used to provide haptic feedback to the user. The joystick is used to angulate the endoscope tip up-down or left-right. The rotating handle has the dual function of rotating the endoscope and advancing or retracting it. Propulsion of the endoscope is achieved by a linear actuator that is coupled to the handle.

Invendoscope

The design of this system (Figure 3.4) differs from the previous two in that it uses a custom made single-use endoscope [122]. The endoscope has a 10 mm inner sheath with an inverted sleeve. The endoscope is mounted inside a driving unit that has 8 drive wheels. When propulsion is desired, the wheels rotate in a manner that

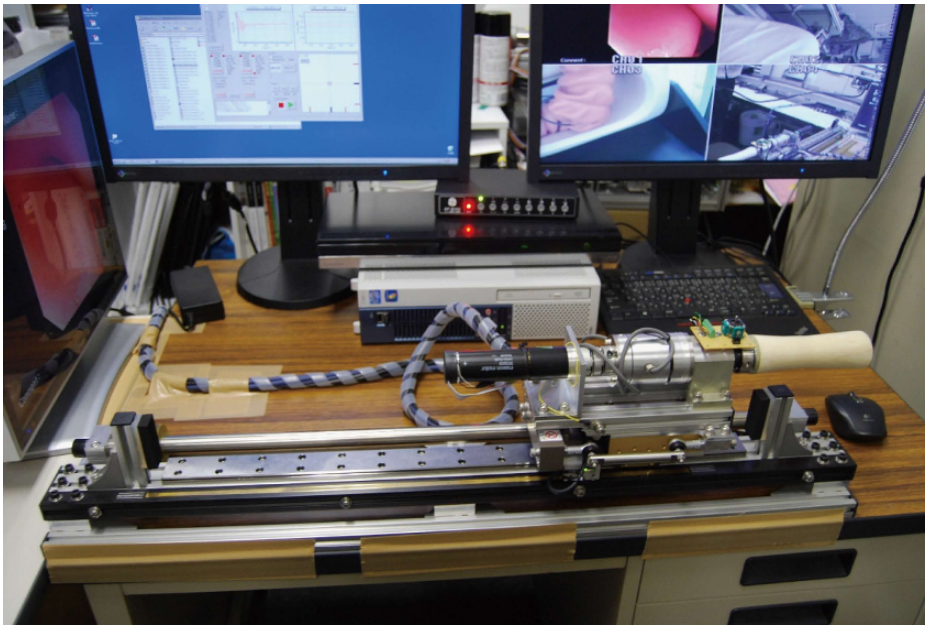

Figure 3.3: Endoscopic Operating Robot v3. The system consists of a master unit with a joystick user interface that and a slave unit in which a conventional endoscope can be secured. The joystick is used to angulate the endoscope tip up-down or left-right. The rotating handle has the dual function of rotating the endoscope and advancing or retracting it.*Reproduced with permission from [79] © 2015 Georg Thieme Verlag KG.*

unfolds the sleeve causing the inner sheath to translate forward or backward. Due to this propulsion mechanism, there is no relative movement between the endoscope and the colon wall. As a result, the forces exerted on the colon wall are minimized. The system is fully controlled by a hand held joystick interface that incorporates other endoscopic software functions. In a human clinical study, the Invendoscope achieved a promising cecal intubation rate of 82 % [122]. However, despite the unique propulsion mechanism, two patients experienced severe pain. More recent results have shown better intubation rates, but it remains to be seen if this system is successful in reducing pain for patients [122]. The latest generation of the system will be commercially available in the US and Europe in 2018 [62].

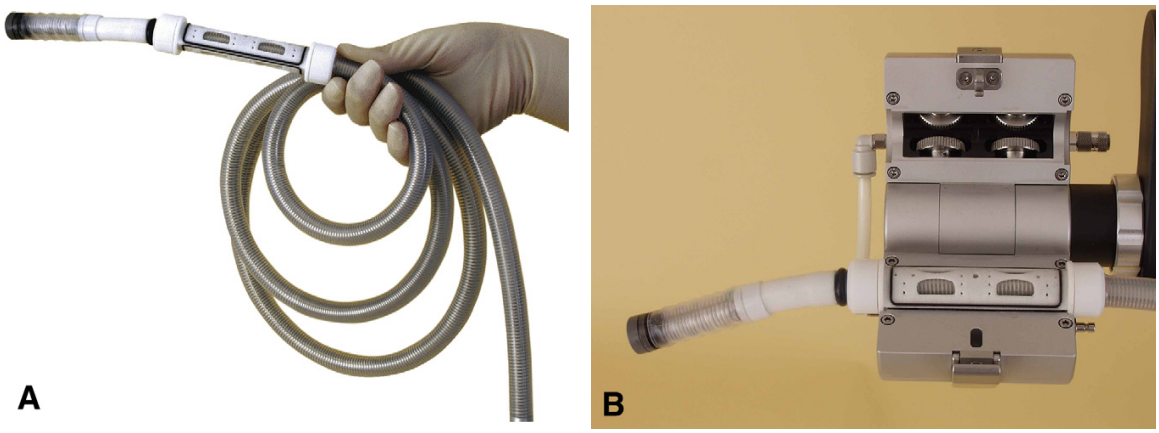

(a) The Invendoscope SC40.

(b) The driving unit.

Figure 3.4: The Invendoscope, a single-use custom endoscope that is propelled by a driving unit that unfolds an inverted sleeve. *Reproduced with permission from [122] © 2008 Elsevier.*

3.1.2 Advanced Endoscopes with Alternative Locomotion Mechanisms

Neoguide

This system (Figure 3.5) uses a type of continuum robot for its endoscopic shaft. The robot is autonomously controlled to conform to the shape of the colon by having each of its 16 successive segments assume the shape that the tip had when it was at a given insertion depth [40]. In essence, the motion of the segments follows the "follow-

Figure 3.5: The continuum robot based endoscopic shaft of the Neoguide system. *Reproduced with permission from [40] © 2006 Georg Thieme Verlag KG.*

the-leader" principle. In doing so, the Neoguide reduces the lateral forces applied

on the colon wall. Moreover, the system includes the ability to display a real-time 3D map of the colon traversed by the endoscope. In a clinical study with a total of 10 patients, this system had a cecal intubation rate of 100 %. However, looping was reported in 4 cases. In addition, further studies are needed to determine if the procedure can be done without sedation.

Aer-O-Scope

The Aer-O-Scope (Figure 3.6), as the name suggests, uses air pressure gradients for propulsion [169]. The system consists of a rectal introducer, a supply cable, and a vehicle balloon that encompasses an endoscopic camera. Another balloon at the rectal introducer is used to form a tight seal at the anus to prevent any gas from leaking. Similarly, the vehicle balloon, which is at the distal end, is inflated to form a seal against the colon wall. Propulsion is then achieved by inflating the air between the two balloons with CO_2 gas. The pressure difference created between the two spaces separated by the vehicle balloon causes the endoscope tip to advance along with the balloon. The vehicle balloon conforms to the shape of the colon as it moves along the lumen while maintaining the seal with the colon wall. The pressure created by the gas insufflation is monitored to prevent excessive pressures that could lead to pain. The user interface is a set of buttons that allow the operator to move the endoscope forward or backward as well as pause or stop the operation. Thus the system is skill-independent, self-propelling, and self-navigating. However, since no instrument channels are available, through which therapeutic instruments could be passed, the system can only be used for diagnostic purposes. In a preliminary animal study, the Aer-O-Scope demonstrated a cecal intubation rate of 83 %. Further study is required to determine if the novel propulsion mechanism and pressure regulation found in this system could potentially reduce pain in human colonoscopies.

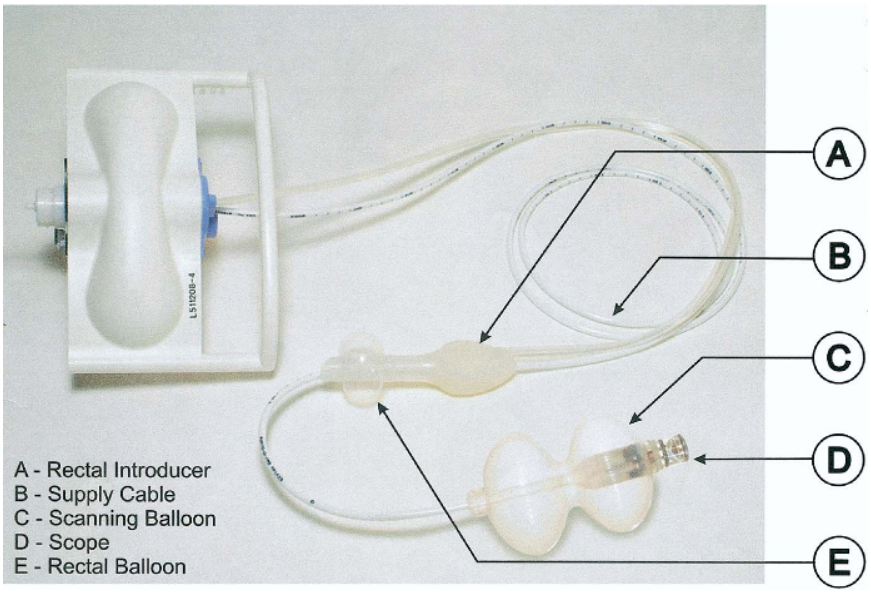

Figure 3.6: The Aer-O-Scope disposable unit. Propulsion achieved by inflating the air between the scanning and the vehicle balloons with CO_2 gas. *Reproduced with permission from [169] © 2006 Elsevier.*

Endotics

The propulsion mechanism of the Endotics system (Figure 3.7) is inspired by inchworms. The system consists of a disposable probe which contains a steerable tip, a flexible body and pneumatic extensors and two clampers that carry out inchworm like movements [112]. The tip has LEDs for illumination and a miniature camera. The two clampers are located at the two ends of the probe and they adhere to the colon wall by creating localized vacuum regions. The extensor uses a system of bellows to elongate the middle part of the probe using pneumatics. During propulsion, the system carries out a semi-automatic cycle of clamping the distal end, elongation, clamping the proximal end and releasing the distal end, and retraction of the distal end. Of these, the elongation is performed with the control of the operator [26]. A human study [161] was conducted with a total of 71 patients to compare the diagnostic accuracy of the Endotics system to that of the conventional endoscope. The system had a cecal intubation rate of 81.6 % which was significantly lower than the conventional endoscope.

(a) The Endotics disposable probe.

(b) The Endotics system.

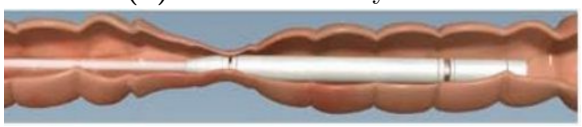

(c) The clamping mechanism adhering to the colon wall by creating localized vacuum regions.

Figure 3.7: The Endotics system is a novel disposable endoscope. Two clampers and a pneumatic extensor perform locomotion inspired by inchworms. *Reproduced with permission from [11] © 2013 Elsevier.*

Furthermore, the average time to complete the procedure was significantly longer for the Endotics (45.0 ± 18.5 min) than for conventional endoscopy (23.7 ± 7.2 min). The findings showed that the diagnostic accuracy of the Endotics system was on par with conventional endoscopy. However, in 13 cases (18 %), the device was not able to reach the cecum. Notably, the study showed that sedation was not required for patients during examination using the Endotics system. A more recent retrospective study [160] on patients who had conventional endoscopy but had failed cecal intubation has shown that the Endotics system was successful in 93.1 % of the cases. This is a very positive result, but further studies are needed to directly compare the system with conventional endoscopes. Furthermore, the study used an earlier version of the system which did not have an instrument channel for passing therapeutic tools, and thus was diagnostics only, suggesting further study.

3.2 Capsule Endoscopy

Advances in miniaturization technology over the past two decades have given rise to a new class of endoscopic devices that enable visualization of the entire gastrointestinal (GI) tract, including the small bowel, in a manner not possible before. CEs are small enough to be swallowed and can travel through the GI tract either passively via peristalsis or actively through various modes of locomotion. With the exception of bowel preparation, which is also necessary for conventional endoscopy, CEs offer the least discomfort and pain while allowing direct visualization of the GI tract. Since their introduction in 2000 [61], and commercialization in 2001 [136], they have found widespread use in clinical settings, especially for the small intestine, a part of the GI tract difficult to access using conventional endoscopes.

In order to capture and transmit high quality video for a long period of time as it travelled through the GI tract without using fiber-optic bundles or external wires, the first CE made use of three enabling technologies: complementary metal oxide silicon (CMOS) image sensors, application-specific integrated circuit (ASIC) devices, and white-light emitting diode (LED) illumination [61]. Images captured at 2 frames per second were transmitted using UHF-band radio-telemetry to antennae attached to the patient [148]. The first human studies using this device showed that it was easy to swallow and caused no discomfort. The capsule moved through the GI tract with the help of peristalsis and the average time between ingestion and evacuation was 24 hours. During this period, the capsule transmitted up to 6 hours of video [61].

The success of the first CE led to a commercial device by Given Imaging Ltd. (Yokneam, Israel) marketed as the M2A and later as PillCam SB. The latest version, PillCam SB3, obtained clearance from the Food and Drug Administration (FDA) in 2013 [139] for sale in the USA. The SB3 brings many improvements over the original CE. With improvements in CMOS technology and precision optics, the SB3 is capable of detecting objects up to 0.1 mm in diameter [139]. In addition, it dynamically

adjusts the video frame rates so as to conserve energy while providing higher frame rates when passing through regions of interest. The images recorded by the capsule are compiled and presented to the physician for analysis. Since it can be tasking for the physician to look through all the images, Given Imaging provides an image analysis software that automatically identify pathologies and reduce the number of images to be presented to the physician.

In addition to the SB3, the Pillcam product line includes the ESO3 and the COLON 2 for esophageal and colon examinations respectively. Other wireless capsule endoscopes (WCEs) on the market include the MiroCam (Intromedic Co., Seoul, Korea), the EndoCapsule series (Olympus Inc., Tokyo, Japan), OMOM (ChongQing JinShan Science and Technology Co, Ltd., Chongqing, China) and CapsoCam (CapsoVision Inc., Saratoga, CA, USA). These WCEs offer similar functionalities with varies improvements in field of view, image quality and transmission technology.

(a) Pillcam, (Given Imaging Ltd., Yokneam, Israel)

(b) MiroCam (Intromedic Co., Seoul, Korea)

(c) EndoCapsule series (Olympus Inc., Tokyo, Japan)

(d) OMOM (ChongQing JinShan Science and Technology Co, Ltd., Chongqing, China)

Figure 3.8: Various commercially available capsule endoscopes. *Adapted with permission from [24] © 2016 Springer-Verlag Berlin Heidelberg.*

In terms of medical practice, CEs are far more successful for the small bowel than for the stomach, esophagus or colon. The fact that the small bowel is very difficult to access using conventional endoscopes has made CEs the gold standard for

small bowel screening. A study has demonstrated that CEs have a higher sensitivity (90.6 % vs. 65.6 %) and diagnostic yield[1] (71 % vs 65 %) in the small bowel than balloon enteroscopy [69]. For other parts of the GI tract, the advantage of CE has not outweighed its limitations. For example, the Pillcam Colon 2 was specifically designed for the colon with two cameras and a wide angle view. However, a study with 100 patients showed that the capsule had a sensitivity of 84 % and specificity of 64 % for polyps larger than 6mm and a sensitivity of 88 % and specificity of 95 % for polyps larger than 10mm whereas both sensitivity and specificity are well above 90 % for conventional endoscopes in the colon.

While various factors exist as to why capsules do not perform as well as conventional endoscopes in other parts of the GI, the main limitation stems from the lack of active locomotion. All commercially available CEs currently move along the GI tract passively being guided by the flow of nutrients due to peristalsis. Thus, there is no means for a physician to see a particular area from different points of view or manipulate the capsule to move in certain directions to get a better understanding of the nature of a lesion.

To this end, many researchers are working towards active locomotion of CEs [164, 139, 136, 140]. The types of actuation used to induce forces and torques on the capsule can be classified into those that use electromechanical systems and those that use external magnetic fields.

3.2.1 Electromechanical Actuation

Researchers in the past two decades have proposed various electromechanical actuation schemes for CE including locomotion inspired by inchworms, crawling using miniature legs or paddles, and swimming via propellers.

[1]The likelihood that a test will provide the information needed to establish a diagnosis

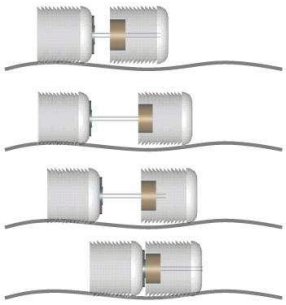

(a) Inchworm capsule by Kim et al. [73]. Impact-based piezo actuators and clamping devices create cycles of elongation, clamping and retraction.

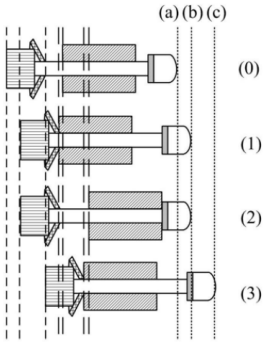

(b) Inchworm capsule by Wang and Meng [170]. A plunger attached to the solenoid moves the capsule forward while the cone shaped polymer prevents motion in the reverse direction.

Figure 3.9: CEs that use inchworm locomotion. *Reproduced with permission from [73, 170] © 2005, 2006 IEEE.*

Inchworm locomotion generally involves repeated executions of anchoring and forward motion. In 2004, Kim et al. [72] developed an inchworm-like microrobot using a pair of spring-type shape memory alloy (SMA) actuators. The same authors, in 2005 [73], developed a mechanism that made use of impact-based piezo actuators and clamping devices that mimic claws of insects. A saw tooth shaped voltage input was applied to the piezo actuators to create cycles of elongation, clamping and retraction (Figure 3.9a). In 2006, Wang and Meng [170] developed a capsule that used a solenoid, a permanent magnet and a cone shaped polymer for inchworm-like locomotion. In this device, an alternating current is applied to the solenoid creating an alternating attractive and repulsive force against the permanent magnet. A plunger attached to the solenoid moves the capsule forward while the cone shaped polymer prevents motion in the reverse direction (Figure 3.9b).

Legged capsule locomotion was first proposed in 2004 by Menciassi et al. [95]. While the authors did not develop a fully functional capsule, they provided analysis on the requirements for a legged locomotion and provided a SMA based solution for the design of a single leg. The same research group later developed legged capsules

moving away from SMA actuators due to their low generated force and practical issues with heat transfer and power consumption [121]. Variants of the legged capsule with 4, 8 and 12 legs were developed where increasing the number of legs helped to prevent back slippage and allowed for more propulsive force [28, 121, 166]. The 4-legged capsule in [28] moved all legs simultaneously while the 8 and 12-legged capsules each had two sets of legs where each set was controlled independent of the other. The capsule presented in [166] (Figure 3.10a) used a novel slot follower and lead screw mechanism with two sets of six legs leading to a compact mechanism that resulted in a capsule with similar dimensions as commercially available CE. Lin and Yan used the inchworm scheme of locomotion on a capsule with three legs for anchoring creating a hybrid locomotion CE.

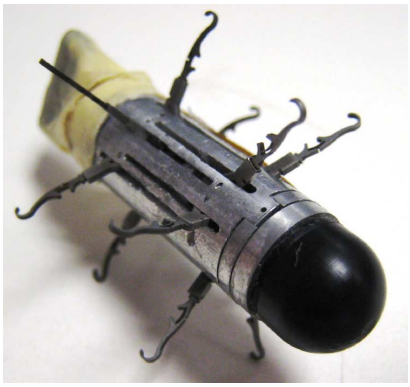

(a) 12 legged capsule by Valdastri et al. [166]. The capsule had two sets of six legs that were controlled independently.

(b) Paddling capsule by Park et al. [106]. A linear actuator moves the legs up and down the length of the capsule much like paddles of a canoe.

Figure 3.10: Legged and paddling type CEs. *Reproduced with permission from [166, 106] © 2009, 2007 IEEE.*

Park et al. [106] introduced paddling as an alternative means of locomotion where the legs of the capsule serve as the paddles of a canoe. A linear actuator (made using micro motor and a lead screw) moves the legs up and down the length of the capsule (Figure 3.10b). During propulsion, the legs protrude out making a clamping contact with the lumen. After the propulsion phase is completed, the legs are retracted and

moved to the front of the capsule without moving the capsule itself. This locomotion scheme overcomes the problem of back slippage that exists with legged capsules. However, animal trials have shown that it could cause mucosal injuries [74].

A propeller based swimming CE was developed by Tortora et al. [158] in 2009 for applications in a liquid filled stomach. The capsule was 15 mm in diameter and 30 mm in length and contained a wireless microcontroller and a small battery. The capsule's four propellers were operated by four separate motors, which allowed the generation of forward propulsion without inducing a rolling torque on the capsule. The capsule was controlled wirelessly via a joystick.

Electromechanical Actuation Summary

CEs with electromechanical actuation require that the actuation mechanism be mounted on the capsule. Unlike electronic components, miniaturization of electromechanical actuators is difficult and requires careful design in order to achieve the required forces and torques without increasing the size and weight of the CE. The complexity of the resulting capsule leads to increased cost, which could prevent the clinical success of electromechanically actuated CEs. Furthermore, the relatively high power requirements of the actuation mechanisms limit the amount of time these capsules can operate from the small batteries found in the capsules. Consequently, electromechanically actuated CEs have only been limited to research settings thus far.

3.3 Actuation Using External Magnetic Fields

Systems for active magnetic actuation generally use either electromagnets or permanent magnets to generate and control magnetic fields external to the patient. Magnetically actuated CEs contain internal magnetic materials in the form of small magnets or ferromagnetic materials. When magnets are used, permanent magnets are preferred over electromagnets due to their high magnetic field strength to size ratio.

The forces and torques created by the interaction of the external magnetic field with the internal magnetic material provide a mechanism for wirelessly actuating CEs. This wireless actuation mechanism is especially suited for endoscopy as it does not require line of sight. Furthermore, the compliant nature of magnetic forces provides a safe means of actuation unlike conventional endoscopes where force is transmitted through rigid mechanical structures.

3.3.1 Sources of External Magnetic Fields

Electromagnets are currently the most flexible source of external magnetic field for magnetically actuated CEs. They are made from coils which become magnetized when electric current passes through them. In the majority of applications, the coils are arranged so as to generate uniform magnetic fields or field gradients at a target region. Since it is difficult to generate uniform magnetic fields or gradients with a single coil, Helmholtz and Maxwell coils are used frequently. Helmholtz coils are constructed by placing two coils of the same dimension and Ampere turns in parallel at a distance equal to their radius [140]. When current flows in the same direction inside the two coils, a nearly uniform magnetic field is generated in the region central to the two coils. Magnetic field gradients can be generated using Maxwell coils, which are constructed in a similar manner to Helmholtz coils, but the separation of the coils is increased to $\sqrt{3}$ times the coil's radius. Maxwell coils can also be used to generate a more uniform magnetic field, instead of a gradient, with the addition of a third coil. The region of uniform fields or gradients generated by these coil arrangements is limited to a relatively small volume of space at the center of the pairs. Thus, large dimensions are needed in order to create a workspace that encompasses the region of the GI tract in which a particular CE operates.

For any given electromagnet, the strength of the magnetic field generated by its coils varies linearly with the current being applied. This simplifies the design of

controllers as they can rapidly control the wrench (force and torque) induced on the CE in a relatively simple manner. This is in contrast to permanent magnet based controllers which require translating or rotating the actuating magnet in space to achieve the same task. Electromagnets also have an OFF state where no magnetic field is generated. This makes them much safer as they can remain in the OFF state until a specific procedure is about to be performed. As such, unintentional magnetic interaction with the environment can be safely avoided.

However, electromagnets have certain limitations that have yet to be overcome. These limitations mainly stem from the inherent nature of magnetic fields in that the strength of the generated magnetic field drops off at a rate of $1/r^3$ where r is the distance from the source. To make matters worse, the force induced on the CE, which is a function of the gradient of the magnetic field, drops off at a rate of $1/r^4$. This necessitates bulky coils and large currents. The bulky coils become unwieldy for clinical settings and the large currents generate heat due to resistive losses in the coils. Appropriate cooling systems become necessary to avoid overheating the coils. The combination of these factors increases the cost of manufacturing electromagnets suitable for magnetic actuation of CEs.

Consequently, permanent magnets are becoming the more common choice of actuation for these systems since they are able to maintain compact form factors while being able to induce relevant forces and torques on the capsule efficiently [17, 164, 90]. While it is possible to have an arrangement of permanent magnets that are fixed in space but are allowed to rotate for actuation, as demonstrated by Ryan and Diller [124], their workspace is severely limited without using extremely large magnets. A better trade-off between magnet size and workspace can be achieved by using a single permanent magnet mounted on a robot manipulator [164, 90, 151, 152, 138].

One downside with permanent magnets is that they do not have an OFF state. Unintentional interaction with other magnets or ferromagnetic materials can be hazardous in clinical settings. Although it is plausible that an OFF state could be achieved using field cancellation techniques, it has not been demonstrated for the types of magnets needed for magnetically actuated CEs. Thus, care must be taken even when the system is not in active use.

Another limitation is the difficulty in controlling the magnetic wrench induced on the capsule. As mentioned earlier, controlling the wrench is accomplished by changing the position and orientation of the actuating permanent magnet relative to the magnetic CE. There is a nonlinear relationship between the magnetic field strength and the relative pose of the external permanent magnet and the magnetic CE. Therefore, controllers for these systems generally have added complexity.

The use of electropermanent magnets for anchoring surgical devices across the abdominal wall has been reported by Tugwell et al. [159]. These types of magnets have the capability of being turned on and off by applying a short pulse of current. This makes them ideal for clinical use as they combine the efficiency of permanent magnets and the safety of electromagnets. It remains unknown whether these types of magnets can be strong enough to induce the necessary forces and torques making them suitable for magnetic capsule endoscopy.

3.3.2 Magnetic Control Strategies

Magnetic control strategies can be classified into open and closed-loop control. In general, open-loop control is defined as the control of a system without some type of feedback as to whether the system is performing as expected. In the case of magnetic actuation, we refine the definition to include systems where there is feedback, but the feedback is only available to the human operator. It is then the responsibility of the human to command the system in a way that responds to the feedback appropriately.

In the particular case of CEs, the feedback is in the form of video of the GI lumen captured by cameras on the CEs.

The advantage of the open-loop strategy is in the simplicity of the overall system as it relies on the brain power of the physician to close the loop. However, this advantage is countered by the steep learning curve required for efficient control of the CE as a result of the unintuitive nature of magnetic fields and the wrench they exert on the capsule. Open-loop systems are considered less safe because they do not have a means to ensure that the wrench exerted on the capsule is below a threshold where tissue damage can occur. While it is possible to provide visual indication of the wrench, it is difficult for the physician to constantly monitor the values while at the same time performing the unintuitive and difficult task of maneuvering the capsule. Even if human operators were able to detect wrenches that exceed a given threshold, they may not respond in a timely manner to avoid damage.

Closed-loop control is a strategy in which the controller incorporates measurements about the state of the system in determining the next control inputs. The controller uses measurements in a feedback loop to reduce the error between a reference state and the current state of the system. This allows the system to constantly monitor for unsafe levels of force and take appropriate and timely action to avoid tissue damage. Closed-loop strategies also provide the opportunity to create intuitive user interfaces for maneuvering the capsule. In essence, instead of manipulating the capsule indirectly through the magnetic actuation system, the physician can assume a more direct control of the capsule and the magnetic actuation system strives to make itself transparent. While video feedback is still available to the human operator, the feedback loop created by the physician constitutes a higher and more intelligent level of control than that which is available in open-loop systems. In this higher level of control, the physician is relieved of the burden of determining the control inputs to

the magnetic actuation system. Instead, the focus of the physician can be dedicated to guiding the capsule and inspecting the GI lumen.

A variety of sensory modalities can be used to generate feedback for the control system. In general, the closed-loop control system does not use sensor measurements directly. Instead, the measurements are first used to compute the position and rotation (pose) of the capsule or the magnetic wrench being applied on it. These quantities are then used to compute control inputs that reduce pose or wrench errors. Other modalities, such as pH and temperature can also be available on the capsule, but they are seldom used for feedback for the closed-loop system.

Open-loop and closed-loop control strategies for magnetic actuation have been utilized with both electromagnets and permanent magnets. Although not a strategy, another mode of control that is better suited for permanent magnet based systems involves the physician holding and manipulating the external magnet manually. The simplicity of the overall system is attractive, but it bears all the disadvantages of the open-loop system. Additionally, since external permanent magnets that generate wrenches strong enough for magnetic actuation are quite heavy, muscle fatigue is unavoidable without special mechanisms that support the weight while allowing full dexterity of manipulation.

3.3.3 Magnetic Propulsion

Notwithstanding how the external magnetic field is generated, existing magnetic actuation systems can also be classified into two categories based on the method of propulsion used. In the first category, which we call indirect propulsion, the applied magnetic wrench causes some type of motion on all or part of the capsule. The interaction of this motion with the surrounding environment, in turn, causes the capsule to propel. The second category is called direct propulsion. In this category,

magnetic force and torque are simultaneously used to directly pull or rotate the capsule to control its position and orientation.

3.3.3.1 Indirect Magnetic Propulsion Systems

Examples of indirect magnetic propulsion include spiral [131, 82, 76, 92, 91, 177, 115], helical [43], rolling [179, 94], and vibrational [77, 65, 98, 78] CEs. The earliest example of indirect propulsion CE was a spiral motion device developed by Sendoh et al. [131] in 2003. Three pairs of coils, each pair in Helmholtz arrangement, were used to generate a rotating magnetic field. The generated field induced a steady torque on the diametrically magnetized permanent magnet embedded inside the capsule (Figure 3.11a). The outer shell of the capsule had a thread-like spiral shape. Upon rotation of the capsule, the outer shell interacts with the lumen to generate propulsion in a corkscrew manner.

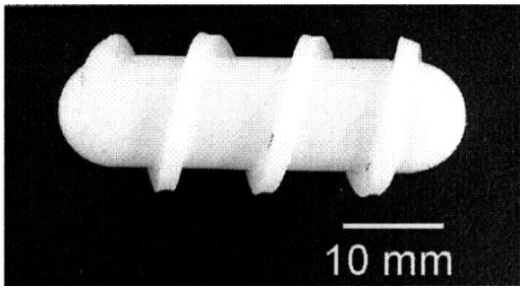

(a) Outer shell of a spiral motion capsule by Sendoh et al. [131]. Three pairs of Helmholtz coils induce steady torque on the diametrically magnetized permanent magnet embedded inside the capsule. *Reproduced with permission from [131] © 2003 IEEE.*

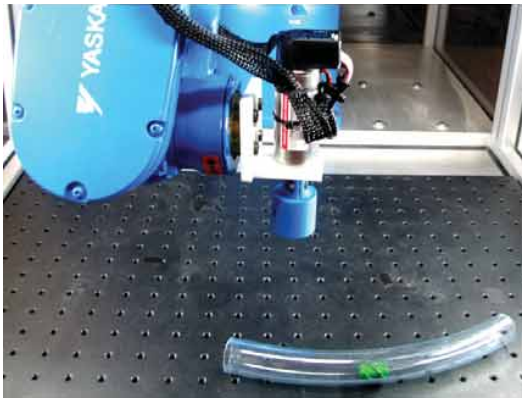

(b) Spiral CE system by Mahoney and Abbott [91]. A rotating permanent magnet is mounted on 6 degrees of freedom (DOF) robot manipulator to propel a spiral capsule. *Reproduced with permission from [139] © 2014 Taylor & Francis.*

Figure 3.11: Examples of CEs with indirect magnetic propulsion systems.

The work of Sendoh et al. [131] inspired other researchers to investigate the use of spiral motion for magnetic actuation of CEs [82, 76, 91, 177, 115]. Instead of the large

Helmholtz coils used by Sendoh et al. [131], Lee et al. [82] used rotating permanent magnets carried by a SCARA-type robot manipulator for their spiral-type capsule. They also used flexible threads affixed to the capsule shell to create the necessary spiral structure. The use of flexible threads mitigated issues related to slippage of previously developed spiral CEs when the lumen in which they operate had a diameter that was larger than the capsule (*e.g.* colon). The same group later developed another thread mechanism that can be disabled so as to allow direct propulsion for cases where the capsule is inside a much larger cavity like the stomach [76]. Although the system employed a robot manipulator, the overall system was controlled in open-loop per our earlier definition (see Section 3.3.2).

Mahoney and Abbott [91] provided a mathematical model for generating rotating magnetic fields for any desired rotation axis using a single rotating permanent magnet without constraining the magnet's position in space. This created a richer control space in which the actuating magnet can optimize a secondary task such as obstacle avoidance while propelling the capsule. The same research group later utilized these findings to actuate a spiral capsule. A motorized rotating permanent magnet was used in their system and the magnet was attached to a 6 DOF manipulator (Figure 3.11b). The group also integrated a magnetic field based localization system resulting in a fully closed-loop actuation system [115].

It is worth mentioning that none of the spiral-type CEs developed by these groups included a camera module. Thus, the operation of the spiral type propulsion in conjunction with a physician watching the video of the lumen has not been demonstrated. We hypothesize that image stabilization and derotation of the camera images will be necessary for clinical acceptance.

Rolling is another type of locomotion that has been pursued by some researchers. Notably, Yim and Sitti [179] developed a compliant and untethered magnetic CEs for use in a liquid filled stomach. The capsule had the ability to be axially contracted in

order to perform additional tasks such as drug delivery or biopsy. The contraction would also deform the capsule making it compliant, which was hypothesized to ease locomotion inside the stomach. The capsule consisted of two permanent magnets at its two ends, a drug chamber and an outer structure based on Sarrus linkages. The linkages fold when there is enough axial force from an external magnet thereby compressing the capsule and releasing the contents of the drug chamber. Should the force be removed, the elastic restoring force of the linkages would restore the capsule to its original shape. A large permanent magnet was used to apply torque and an attractive force on the capsule. The resulting static frictional torque at the contact area between the capsule and the stomach wall caused the capsule to roll. The overall system was controlled in an open-loop manner.

The previously described systems have mainly used rotational motion to indirectly propel the CEs. A different approach to indirect propulsion is the use of vibrations caused by alternating magnetic fields. A microactuator mechanism for self-propulsion of a swimming capsule was developed by Morita et al. [98] in 2010. The mechanism was designed to be used in conjunction with an existing CE. The microactuator consisted of a fin with a permanent magnet and a small spring connecting the fin with the main body of the capsule. An alternating current was passed through external electromagnets creating vibratory motion of the internal permanent magnet. This caused the fin to vibrate, which in turn propelled the capsule [98]. A similar idea was investigated by Kósa et al. [77], although their device could not be considered a CE because it was at an early stage of development. In their system, three tails, each with three adjacent coils were vibrated to create propulsion in a viscous medium. This is in contrast to most magnetically actuated CE where a permanent magnet is used on the capsule side of the system. The external magnetic field was supplied by a magnetic resonance imaging (MRI) machine. The amplitude and phase angles of

the sinusoidal magnetic field generate by the MRI were computed so as to create a sinusoidal travelling wave on the tails akin to flagellar movement of microorganisms.

Since the force and torque induced by the external magnetic field drop as $1/r^4$ and $1/r^3$ respectively, where r is the distance between the source and the capsule, using the torque for propulsion is preferable. However, current rotational propulsion systems designed for GI exploration rely on friction against lumens, and thus can only be propelled in collapsed lumens resulting in reduced polyp detection efficiency in parts of the GI tract such as the colon. Furthermore, this actuation strategy has only been demonstrated on untethered devices which are currently limited to diagnostic purposes and lack therapeutic capabilities such as polyp resection and biopsy sampling of suspect tissue.

3.3.3.2 Direct Magnetic Propulsion Systems

One of the earliest examples of direct magnetic propulsion CEs was developed by Carpi et al. [16] in 2006. Designed to work with existing passive CEs, their device consisted of a magnetic shell made from a mixture of silicone and Neodymium-Iron-Boron (NdFeB). The authors built a prototype using the commercially available CE M2A, a product of Given Imaging Ltd, Israel. The external source of magnetic field was a pair of permanent magnets and propulsion was achieved by manually (by hand) translating and rotating these magnets. Preliminary tests using the prototype on a porcine model showed that arbitrary translation and rotation of the capsule could be achieved. This promising result led to subsequent works by the same group where the hand held external magnets were replaced with the Niobe Stereotaxis system (Figure 3.12a), a commercial magnetic navigation system originally developed for steering magnetic catheters in the cardiovascular system [15, 17, 13]. In addition, real-time fluoroscopic imaging was used for localization. However, the purpose of the localization was to document and identify regions of interest indicated by the

physician. Since the main control capability of this system had to do with orientation, and the magnetic field created by the Stereotaxis system was sufficiently uniform, the controller only needed to set the magnetic field vector inside the workspace. Under simplified assumptions, due to the nature magnetic fields, the uniform field aligns the capsule to point in the direction of the field without requiring knowledge of its previous orientation. Thus, the overall system would be considered open-loop. Inspired by the Stereotaxis system, Mingyuan Gao et al. [97] developed a new magnetic propulsion system that was specifically designed for magnetic propulsion of CEs. The system had a platform that served as a bed for the patient, but could also translate in longitudinal and lateral directions. Two groups of permanent magnets straddled the platform and were nominally located above and below the patient. The magnets could rotate about a central longitudinal axis located at the base of the platform and move linearly relative to each other as well as relative to the platform. A similar concept was pursued by Sun et al. [147] who designed a novel magnetic actuation system that was comprised of two 4 DOF (3 DOF in position and 1 DOF in orientation) robot manipulators that were placed on the lateral sides of patient's bed. Each robot carried an external permanent magnet which was axially magnetized. The magnets were controlled in open-loop by looking at the captured GI images. The authors also demonstrated that the same magnetic actuation system could be used for indirect magnetic propulsion as well as the propulsion of hybrid capsules (capsules that use magnetic and electromechanical actuation).

An alternative approach that could reduce the size of the permanent magnets used in [13] and could achieve better control of the translation of the capsule was proposed by Ciuti et al. [25] in 2009. The reduction of the magnet size was achieved by mounting the permanent magnet at the end effector of a 6 DOF robot manipulator. Better translational control could also be achieved with the help of the robot manipulator as the external permanent magnet can now be positioned and oriented in space so

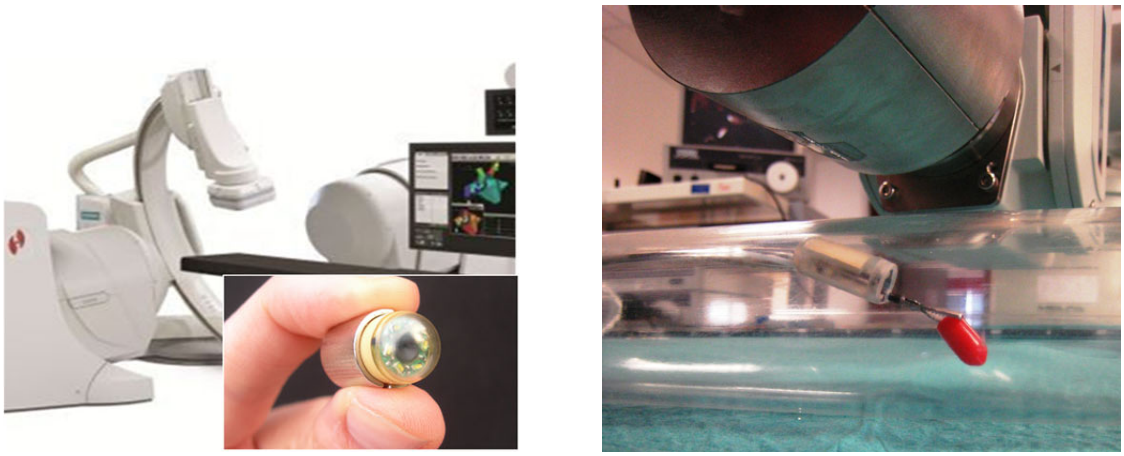

(a) The Niobe Stereotaxis system and a commercially available CE with a magnetic shell developed by Carpi et al. [13]. *Reproduced with permission from [24] © 2016 Springer-Verlag Berlin Heidelberg.*

(b) The Magnetic Air Capsule developed by Valdastri et al. [164]. The fully functional capsule was driven by an external permanent magnet that was mounted on a 6 DOF robot manipulator. *Reproduced with permission from [164] © 2012 Springer Nature.*

Figure 3.12: Examples of CEs with direct magnetic propulsion systems.

as to induce the desired force on the capsule. The authors conducted simulations to determine the optimal number and dimensions of permanent magnets to embed inside the capsule. The chosen configuration was four cylinders, each 140 mm^3 in volume arranged on the external surface of the capsule at 90° from each other [25]. In addition to the permanent magnets, the capsule also contained a CMOS camera, inertial sensors, and a wireless communication module. The inertial sensor was used to measure the acceleration of the capsule in order to determine when motion has occurred. Utilizing this sensor modality, the authors were able to close the loop, albeit in a simplistic manner.

A more advanced closed-loop control technique was introduced by Mahoney and Abbott [90] who used a 6 DOF industrial robot arm for manipulating an untethered magnetic device in a fluid filled cavity. The authors demonstrated for, the first time, 5 DOF control of a CE using a single external permanent magnet in a water tank emulating a fluid filled stomach. For localization, the authors used a vision based

algorithm which used a pair of cameras placed outside the water tank. While the localization method was not viable for realistic applications, their control method was instrumental for the work presented in this dissertation.

Further development of this approach was presented by Valdastri et al. [164] who developed a fully functional CE with a compliant multilumen tether (Figure 3.12b). Similar to Ciuti et al. [25], magnetic propulsion was accomplished by an industrial 6 DOF robotic manipulator; however, the addition of the multilumen tether provided insufflation, passing of an flexible instruments, lens cleaning, and power for the vision and sensor modules inside the capsule. The CE used in this dissertation is a progression of this work and will be discussed in detail in Chapter 2.

With few exceptions, the use of electromagnets for wireless manipulation of direct propulsion devices has been limited to objects in the micro scale [153, 80, 37, 107]. Keller et al. [71], in a joint effort by Olympus Medical Systems Corp. and Siemens Healthcare, developed an electromagnetic guidance system based on a modified MRI machine. The system was designed for controlling a capsule in $5 + 1$ DOF inside a liquid filled stomach, where one DOF is achieved by turning the patient. The computation of the currents for the various coils of the MRI machine require knowledge of the position of the capsule; however, the system described by Keller et al. [71] did not have this functionality. Instead, a static point in the center of the working volume was used for these calculations. This resulted in errors in the form of unwanted capsule drifts, which were mitigated by keeping the capsule in contact with the mucosa for stability [71]. Thus, the system operated in open-loop.

Another magnetically actuated CE that used electromagnets as the external source of magnetic field was introduced by Lee et al. [81]. The system consisted of 3 pairs of Helmholtz coils and a single axis Maxwell coil as well as a capsule prototype with a unique arrangement of three permanent magnets such that the resultant direction of magnetization was approximately 22° from the main axis of the capsule.

The Helmholtz coils, which by design generate uniform magnetic fields, were used to control the heading of the capsule while the Maxwell coils were constructed to generate uniform gradients and thereby control the force on the capsule. The authors demonstrated a novel helical motion by taking advantage of the angle between the main axis and the resultant direction of magnetization of the internal magnets. This was achieved by rotating the field direction generated by the Helmholtz coils and controlling the capsule's translation using the Maxwell coils.

While most systems that use electromagnets employ Helmholtz or Maxwell coil configurations, Lucarini et al. [89] proposed a single coil electromagnet that was to be carried by a robot manipulator. The magnet was designed to generate a magnetic gradient of 0.175 T/m (82.5 mN) for attraction and 0.105 T/m for dragging (49.5 mN), and a magnetic field of 50 mT at a distance of 70 mm. A toroidal shape magnet was chosen to dissipate heat faster and reduce the distance between poles for a more reliable control of the capsule. However, the authors reported that due to the high power consumption of the coil, cooling might be needed in order to use the system in real operating conditions.

With the aim of improving dexterity and continuity of locomotion, some researchers have proposed a hybrid approach where direct magnetic propulsion is combined with internal electromechanical actuation mechanisms [171, 135]. In this approach, the internal actuation mechanisms are either used as the primary sources of locomotive force or as means to dislodge the CE when it is stuck in collapsed areas of the GI and is unable to move forward with magnetic force alone. The CE developed by Wang et al. [171] is an example of the former and it used a spiral type internal propulsion mechanism and an external permanent magnet mounted on a 6 DOF robot manipulator. The function of the external magnet in their approach was to provide an attractive force for aiding the internal actuator. Simi et al. [135] introduced the

latter concept with their 3-legged CE that was actuated by a single brushless DC motor. In their approach, an external permanent magnet was used as the main dragging force to propel the capsule. In both examples, the control of both the internal and external actuation mechanisms was done in open-loop.

3.3.4 Magnetic Actuation Summary

The complexity of magnetically actuated CEs is much less than that of CEs with internal electromechanical actuation mechanisms. They can also be made more compact because they do not require large batteries in addition to the internal actuation mechanism. As a result, they are easier to construct, generally more reliable as they do not have many moving parts, and thus, safer to use. Therefore, they present a faster and easier path toward clinical realization of actively actuated CEs.

The limitations of the current state of the art in magnetically actuated CEs primarily stem from the way physicians interact with the system. Various levels of interaction are possible: (1) Hand held operation of the external magnet [85, 16, 149, 168] (2) Open-Loop robotic tele-operation (3) Closed-loop robotic tele-operation and (4) Closed-loop and fully autonomous navigation.

A comparison of hand-held operation against open-loop robotic tele-operation was conducted by Ciuti et al. [22] in 2009. A total of 10 trials were conducted *ex-vivo* on a segment of porcine colon, where 5 were hand-held and the other 5 were robotically tele-operated. Six to eight white spherical targets were placed inside the colon and participants were asked to navigate the entirety of the colon while identifying the targets. The results showed that open-loop robotic tele-operation was superior in precision and accuracy of steering and more targets were identified (87 ± 13 % vs 37 ± 14 %). However, the mean completion time for robotic tele-operation was significantly higher (201 ± 24 s vs 423 ± 48 s). The authors concluded that "fewer targets were reached with manual control because after obtaining view of a target,

the operator was unable to move toward it without the target going outside the visual field. On the other hand, the robotic arm enabled small, precise movements to approach the capsule steadily towards the target" [22]. In addition, the authors found that hand-held operation was more effective for large-scale movements and hypothesized that closed-loop control could improve the performance of robotic tele-operation.

Other studies have further demonstrated the limitation of open-loop control. In the study by Arezzo et al. [4], a robot manipulator with a permanent magnet was used to drive a tethered capsule in a phantom *ex-vivo* model of the colon and procedure times were three times longer when compared against standard endoscopy due to repeated loss of magnetic coupling. In the study reported by Denzer et al. [30], a magnetic resonance imaging (MRI) machine was modified by a joint team of researchers from Olympus and Siemens for magnetic actuation of an untethered device in the stomach. In their clinical trial, a low lesion detection sensitivity of 61.9 % was reported suggesting difficulty in maneuvering.

These results demonstrate the acute need for closed-loop systems that utilize pose estimation feedback. However, the majority of prior works in the literature assume that the capsule is free to move inside the patient once the lumen is distended with gas or liquid. Therefore, the externally generated magnetic field is controlled with the expectation that the capsule would align to it. While this assumption may hold true in most cases, there are often occasions when the capsule gets stuck into a tissue fold and the magnetic coupling is lost. In addition, faster capsule locomotion can be achieved with closed-loop systems without compromising safety.

Robotic closed-loop magnetic actuation systems can also enable fully autonomous navigation. Although not in the scope of this dissertation, this type of system is now in the realm of possibility as image processing techniques continue to advance. Recent advances in deep learning for vision based polyp detection, lumen detection

and environment mapping combined with closed-loop robotic control technologies can enable the next era of capsule endoscopy.

3.4 Pose Estimation for Capsule Endoscopy

Despite the differences in how the driving magnetic fields are generated and what method of propulsion is used, actively controlled magnetic actuation systems require pose estimation in order to successfully translate to clinical settings. We make a distinction here from current clinical methods that localize the capsule relative to anatomical landmarks for subsequent treatment [155, 137]. In this work, we focus on techniques that estimate the pose of the capsule with respect to a fixed global frame so as to enable closed-loop control. However, we will use the terms localization and pose estimation interchangeably as it is common in the literature for magnetically actuated CEs.

3.4.1 Metrics for Pose Estimation Techniques

As a precursor to our discussion, it is beneficial to define the metrics with which we analyze the pose estimation techniques. The criteria for success of a pose estimation algorithm for robotic capsule endoscopy is three fold. First, a level of accuracy suitable for closed-loop control is needed. However, there is no established benchmark in the literature for accuracy in magnetic capsule endoscopy applications. To ground our discussion, however, we will adopt the notion that the position error should be in the same order of magnitude as the dimensions of the capsule [34, 33]. Second, the system must have an update rate appropriate for real-time operation. Although difficult to define precisely, a rate of 100 Hz or faster is generally considered acceptable. This allows the robotic controller to compensate for any deviation of the capsule from the commanded pose or trajectory promptly so as to ensure the safety and clinical efficacy of the system. Finally, the workspace for the pose estimation system must be

compatible with endoscopic magnetic actuation, which has a typical working distance of 150 mm or larger [25].

3.4.2 Alternative Localization Techniques

Several localization techniques have been developed for CEs in the last two decades. A significant portion of these techniques were motivated by the need to localize the capsule near areas of observed ailments within the GI tract for subsequent targeted treatment. As such, some of these techniques did not have real-time operation compatible with magnetic actuation as their main objective.

Radio frequency (RF) based methods, which were some of the earliest localization techniques for CEs, fall in this category. These methods were attractive because most CEs, and particularly the commercially available ones, transmitted images from the GI tract at regular intervals to receivers outside the patient's body. By placing sensors in strategic locations, these transmissions could be used to estimate the location of the capsule at the time it made the transmission [41]. Consequently, RF based methods were inexpensive to implement as they did not require adding new sensors and other electronics to the capsule. The first RF based localization system operated in this manner and it was introduced by Fischer et al. [41] in 2001 for the Given Imaging M2A wireless CE.

Generally, RF based localization techniques can be categorized by the way they utilize the received RF signals to compute the position of the transmitter. The most widely used categories are: time of arrival (TOA), angle of arrival (AOA) and received signal strength indicator (RSSI). For CE applications, TOA based approaches have not been used in practice because RF signals travel at speeds close to the speed of light. Therefore, these approaches require highly accurate and synchronized sensors. For example, in order to achieve an accuracy better than 1 ft ($\approx$300 mm), these sensors must be able to resolve differences of less than 1 ns [155]. Similarly, AOA techniques

have not been pursued because of difficulties related to multipath [5]. However, several authors have published works utilizing these methods in simulation [70, 172, 101, 64, 49, 118, 51]. RSSI based methods have been used successfully [41, 5, 8], but they have slow update rates, mainly due to the interval of RF transmissions, and reduced accuracy owing to multipath and signal attenuation caused as the RF signal propagates through different tissues of the human body. Fischer et al. [41] computed 2-D position using RSSI and reported an accuracy of 3.77 cm. Arshak and Adepoju [5] used an empirical signal propagation model to account for path loss and a nonlinear iterative trilateration algorithm, but they did not report the absolute accuracy.

Other sensor modalities that are normally used for diagnostic purposes have been investigated for localization. These include MRI [39], X-ray (fluoroscopy) [13], positron emission tomography (PET) [154], and Ultrasound [42]. All of these approaches have drawbacks that make them less likely to be compatible for magnetically actuated CEs. MRI based methods generate large magnetic fields and gradients that could directly interfere with the magnetic actuation system. Although sub-millimeter accuracy can be achieved, constant exposure to potentially harmful radiation is a significant concern in X-ray (fluoroscopy) and PET based localization. Ultrasound based localization is safe, but could suffer from acoustic impedance mismatch due to the air-tissue interface [14].

Computer vision is another technique that has been pursued by researchers where images of the GI tract captured by the CE are processed to determine its position and orientation [60, 99, 1] as well as to classify the region of the GI tract from which the images were taken [38]. The performance of computer vision based methods is highly dependent on the quality and rate of the images being captured. Occlusion, blur, and bad lighting as well as sudden motions of the capsule can cause these techniques to fail. In light of this, some authors have proposed hybrid techniques that utilize vision and RF or magnetic field based localization [87, 86, 8, 46]. A common limitation

with computer vision based methods that compute the pose of the capsule is that the pose is expressed relative to an arbitrary starting frame or to a chosen frame in a map generated by the technique itself. The transformation between this frame and a global fixed frame is not determined. Therefore, using these techniques for robotic actuation is a challenge.

3.4.3 Magnetic Field Based Localization

Another approach for localization in capsule endoscopy that has been gaining popularity in the last decade is the use of magnetic fields. Unlike RF and ultrasound signals, the effect of the human body on quasi-static magnetic fields is negligible. As a result, much better accuracy and precision can be achieved without the need to model the propagation characteristics of the field through the patient. These fields are also generally considered safe unless they are very strong or the patient has magnetic implants. An additional advantage with the magnetic field based approach is that it affords the possibility to use the magnets that are already present in the system to perform localization. In this manner, the overall cost can remain low and compatibility with magnetic actuation becomes a possibility.

Several magnetic field based localization techniques can be found in the literature and their difference can be characterized in various ways including the sensors they use, the topology of the sensors, the type of magnetic field source they use, and the location of the sensors and the magnetic field sources. To facilitate our discussion, we will use the latter categorization.

Regardless of their categorization, all magnetic localization methods exploit the relationship between pose and magnetic field vectors, *i.e.*, given a known source of magnetic field, the magnetic field vector at a point is a function of the relative position

of the point from the source of magnetic field:

$$\mathbf{B} = \mathbf{B}(\mathbf{p}) \tag{3.1}$$

where $\mathbf{p}$ is a position vector from the magnet to the point of interest (see Appendix A for our nomenclature). The problem of magnetic localization can be summarized as the solution to the inverse of Equation (3.1). In addition, if we had a sensor that can measure the 3D magnetic field vector at that point, the measured vector will also be a function of the orientation, R (represented by a rotation matrix) of the sensor relative to the source of magnetic field.

$$\mathbf{B}_s = R\mathbf{B}(\mathbf{p}) \tag{3.2}$$

where $\mathbf{B}_s$ is the magnetic field in the sensor frame.

As we shall see, various techniques have been developed to solve the position, $\mathbf{p}$, and orientation R from these equations. These techniques directly or indirectly solve an optimization problem that can be formulated as follows:

$$\underset{\mathbf{p},R}{\text{minimize}} \quad \|\mathbf{B}_s - R\mathbf{B}(\mathbf{p})\| \tag{3.3}$$

3.4.3.1 Magnetic Field Models

Underlying all of these techniques is the vector valued function $\mathbf{B} : \mathbb{R}^3 \rightarrow \mathbb{R}^3$, which is a model of the magnetic field in space. The accuracy of this model determines the overall accuracy of the localization system. However, higher accuracy has higher computational cost.

For the quasi-static magnetic fields that are used in magnetic manipulation, the magnetic field is governed by Maxwell's equations [109]:

$$\nabla \cdot \mathbf{B} = 0 \tag{3.4}$$

$$\nabla \times \mathbf{B} = \mu_0 \mathbf{J} \tag{3.5}$$

where $\mathbf{J}$ is the current density, which is nonzero only inside a magnet, and $\mu_0 = 4\pi \times 10^{-7}$ is the magnetic permeability of free space. Consistent with these laws, the magnetic field generated by a magnet with current density, $\mathbf{J}$, is given by:

$$\mathbf{B}(\mathbf{p}) = \int_V \frac{\mathbf{J}(\mathbf{p}') \times (\mathbf{p} - \mathbf{p}')}{|\mathbf{p} - \mathbf{p}'|^3} dv' \tag{3.6}$$

where $\mathbf{p}'$ is a point on the magnet and $\mathbf{J}$ is the current density at $\mathbf{p}'$ [45].

For an electromagnet constructed using a coil with N loops carrying current I and has a height of h, the current density $\mathbf{J}$ is given by:

$$\mathbf{J} = \frac{NI}{h} \tag{3.7}$$

For permanent magnets, an equivalent current density can be calculated based on the magnetization, $\mathbf{M}$, of the magnet, which is a measure of the net magnetic dipole moment per unit volume [45].

Equation Equation (3.6) is known as the Biot–Savart law. From this law, we can derive exact analytical models for permanent and electromagnets. These models often involve complicated integrals calling for the use of elliptic integrals, Bessel functions, etc. [31]. Under certain assumptions, however, approximation can be made resulting in a simpler expression known as the point dipole model:

$$\mathbf{B}(\mathbf{p}) = \frac{\mu_0}{4\pi} \left(\frac{3\mathbf{p}(\mathbf{m} \cdot \mathbf{p})}{\|\mathbf{p}\|^5} - \frac{\mathbf{m}}{\|\mathbf{p}\|^3} \right) \tag{3.8}$$

where $\mathbf{m}$ is the dipole moment of the magnet. For permanent magnets, the dipole moment can be easily computed from the magnet's residual flux density, $\mathbf{B_r}$ (an intrinsic parameter of permanent magnets), given by $\mathbf{m} = \frac{\mathbf{B_r}V}{\mu_0}$, where V is the volume. For electromagnets made from coils, the dipole moment is a linear function of the current, $\mathbf{m} = NI(\pi r^2)$, where r is the radius of the coil.

The point dipole model assumes the source of magnetic field is concentrated at a single point and yet has a North and a South pole. The approximation is accurate for a uniformly magnetized sphere [108]. For other geometries, the model gets more accurate as the distance between the test point and the source gets larger. Because of its simplicity, the point dipole model has been used by numerous localization systems. However, the model introduces errors when the distance between the magnet and the sensor becomes small. Some researchers have studied whether these errors can be reduced by optimizing the dimensions of the magnet. They have found that the critical factor is the aspect ratio of the magnets dimensions [108].

3.4.3.2 Localization with External Sensors

This group of localization techniques is characterized by having an array of magnetic field sensors outside the patient. Typically, the sensors are either worn by the patient or placed around the patient in close proximity.

One of the earliest example of localizing magnets inside the human body was developed in 1997 by Weitschies et al. [173]. The localization system was developed to monitor the GI transit of orally administered drug dosage forms with the objective of understanding the transit times through the different parts of the GI as well as the location of their dissolution and drug release. They used a 37 channel superconducting quantum interference device (SQUID), a very expensive yet highly sensitive magnetometer, to measure the magnetic field generated by a sucrose pellet that was coated with magnetite and swallowed by a patient.

For applications in magnetic capsule endoscopy, researchers have instead used arrays of inexpensive magnetic field sensors such as Hall effect and Anisotropic Magnetoresistive (AMR) sensors. The main distinguishing factors among the various localization systems include number of sensors, topology of the sensors, and the algorithms for nonlinear optimization.

As an example, consider a capsule with a cylindrical permanent magnet with a dipole moment of $\mathbf{m}$ and an array of N magnetic field sensors arranged on a 2D plane. Since the magnet inside the capsule is small and the distance of the sensors from the capsule is much larger than the dimensions of the capsule, the point dipole model can be used. The magnetic field measured by each sensor is given by:

$$\mathbf{B}^i_{\text{calc}}(\mathbf{p},\mathbf{m}) = \frac{\mu_0 \left\|\mathbf{m}\right\|}{4\pi}\left(\frac{3\mathbf{p}(\hat{\mathbf{m}}\cdot\mathbf{p})}{\left\|\mathbf{p}\right\|^5} - \frac{\hat{\mathbf{m}}}{\left\|\mathbf{p}\right\|^3}\right), \quad i = (1,2,\ldots,N) \tag{3.9}$$

An optimization problem is now defined as:

$$\underset{\mathbf{p},\mathbf{m}}{\text{minimize}} \quad \sum_{i=1}^{N} \left\|\mathbf{B}^i_s - \mathbf{B}^i_{\text{calc}}\right\|^2 \tag{3.10}$$

where $\mathbf{B}_s$ is the measured magnetic field. This nonlinear optimization problem can be minimized using a variety of methods. After testing several nonlinear optimization algorithms that included Powell, Downhill Simplex, and Multilevel Coordinate Search, Hu et al. [56] concluded that Levenberg Marquardt (LM) was the best algorithm in terms of speed, accuracy and sensitivity to initial guesses. This is also ascertained by its prevalent use for such localization algorithms in the literature.

A number of publications have reported using the outlined optimization problem [129, 58, 59, 57, 175, 143, 83, 56, 74, 172, 111, 145, 53]. Notably, Schlageter et al. [129] were first to use silicon Hall effect sensors and demonstrate that localization is possible at distances up to 14 cm. In their system, a 4×4 array of single axis Hall effect sensors was used as shown in Figure 3.13 and 5 DOF localization was achieved

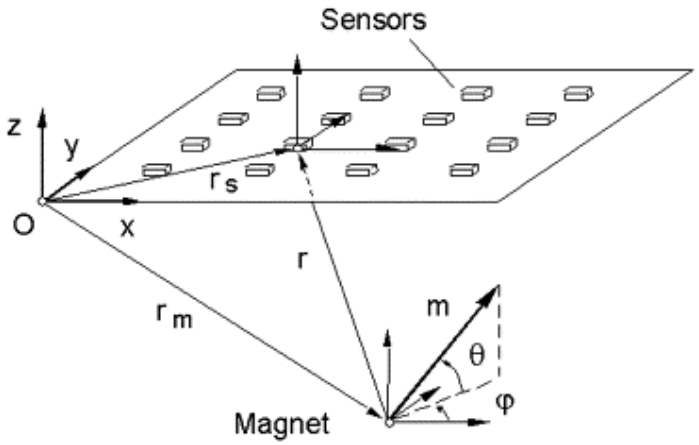

Figure 3.13: Sensor topology used in the localization system of Schlageter et al. [129]. *Reproduced with permission from [129] © 2001 Elsevier.*

using the LM algorithm. Since their sensors were single axis, their formulation was a variant of Equation (3.10) where the projection of the magnetic field vector onto the sensors sensing axis is used instead of the whole 3D vector. The accuracy of the system was analyzed in simulation by modeling noise and sensitivity variations of the Hall effect sensors. They showed that the position accuracy of the system depended on the orientation of the magnet and that the accuracy degraded as the magnet approached the edge of the sensor matrix.

Hu et al. [58] experimentally demonstrated a localization system with 16 3-axis Hall effect sensors uniformly arranged on a 200 mm × 200 mm plane. After experimentally testing 1, 2, and 3-axis Hall effect sensors, they observed that using 3-axis instead of single axis Hall effect sensors improved the accuracy of the system. The average localization errors were 7.8 mm (6.14°) in x, 7.3 mm (5.35°) in y, and 5.6 mm (4.26°) in z with average computation time of 0.137 s. Calibration of the system improved accuracy to an average error of 3.3 mm (3°) [57]; however, the authors observed that the accuracy degraded when the capsule moved outside the area of the sensor matrix. Further improvement in accuracy was made by the same research group by using an array of 64 3-axis AMR sensors on 4 planes forming the sides of

a cube as shown in Figure 3.14 [56]. After calibrating the field sensors' sensitivity

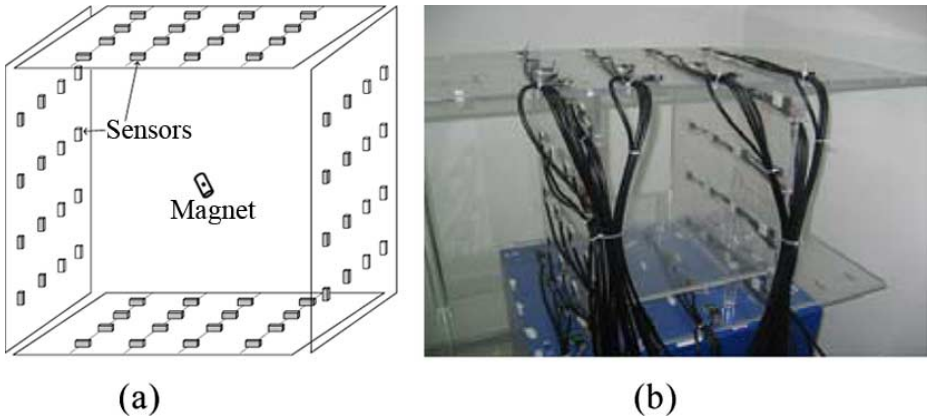

Figure 3.14: Cubic arrangement of magnetic field sensors in Hu et al. [56]. (a) Schematic of sensor topology, (b) Real implementation. *Reproduced with permission from [56] © 2010 IEEE.*

and positioning, the average error with the cubic sensor array system was reduced to 1.8 mm (1.54°). Additional testing conducted by these authors showed that the system was unaffected by the presence of copper and aluminum plates, but severe degradation occurred when ferromagnetic materials were introduced in the region of localization.

Wu et al. [175] developed a wearable system with an array of 60 single axis Hall effect sensors. Two sensors were placed back to back in order to provide opposite outputs for an instrumentation amplifier thereby improving the signal to noise ratio. Furthermore, 3 pairs of sensors were arranged so as to measure the full 3D magnetic field vector. The localization technique worked on the same basis as outlined above using the point dipole model and the LM optimization algorithm.

The use of a cylindrical magnet and the point dipole model in the localization systems described so far limits the localization of the capsule to 5 DOF owing to the symmetry of the magnetic field of a cylindrical magnet about its direction of magnetization. In order to achieve 6 DOF localization, other researchers have proposed

using rectangular [176] or annular [144] magnets with more accurate analytical models rather than the point dipole model. They have shown feasibility in simulation, but did not present experimental data.

Until recently, localization systems that use external sensors were not compatible with magnetic actuation because the external magnet used for actuating the capsule interfered with the sensors' ability to measure only the magnetic field from the capsule. In 2015, Son et al. [142] proposed a 5 DOF localization system compatible with magnetic actuation composed of an array of 8×8 single axis Hall effect sensors arranged on a $70\,\text{mm} \times 70\,\text{mm}$ plane. A stationary external electromagnet was used for actuating a magnetic CE. Owing to the principle of superposition of magnetic fields, the field sensors measured the sum of the magnetic fields from the internal permanent magnet as well as the external actuating electromagnet. Using the point dipole model, the magnetic field of the external magnet at each of the sensors was calculated and subtracted from the sensors' measurements. However, since it was difficult to measure the dipole moment of the electromagnet and the relative position of the external magnet from each of the sensors, the subtracted values were not accurate. To reduce these errors, they performed second order directional differentiation of the magnetic field at the sensors using the five point stencil finite difference method. Upon differentiation, the error terms, which were originally inversely proportional to the cube of the distance, become inversely proportional to the distance to the fifth power. To compute the 5 DOF position and orientation, a cost function composed of the sum of the second derivatives of the magnetic field measurements at each sensor is minimized using the LM algorithm. The average errors were $2.1 \pm 0.8\,\text{mm}$ (distance) and $6.7 \pm 4.3°$ and the update rate was $200\,\text{Hz}$. However, the workspace was limited to $70\,\text{mm} \times 70\,\text{mm} \times 50\,\text{mm}$ due to sensor noise. The authors proposed that using either a larger internal magnet or sensors with lower noise levels could expand the effective workspace.

Similarly, Song et al. [145] implemented a simultaneous tracking and navigation method towards achieving closed-loop control of untethered magnetic CE using an external permanent magnet for actuation. Unlike the stationary electromagnet in Son et al. [142], forces and torques were induced on the capsule by moving the external permanent magnet itself. The sensor array was composed of 8 AMR sensors on a $0.2\,\mathrm{m} \times 0.2\,\mathrm{m}$ plane. Since the actuating and capsule magnets were both permanent magnets only differentiated by their dipole moments, the system can be thought of performing multiple object tracking. Thus, the formulations in Equation (3.9) and Equation (3.10) are modified to include the second magnet.

$$\mathbf{B}^i_{\mathrm{calc}} = \mathbf{B}^i_{\mathrm{calc,ipm}}(\mathbf{p}_{\mathrm{ipm}}, \mathbf{m}_{\mathrm{ipm}}) + \mathbf{B}^i_{\mathrm{calc,epm}}(\mathbf{p}_{\mathrm{epm}}, \mathbf{m}_{\mathrm{epm}}), \quad i = (1, 2, \ldots, N) \tag{3.11}$$

where $\mathbf{p}_{\mathrm{ipm}}$ and $\mathbf{m}_{\mathrm{ipm}}$ are the position vector and the dipole moment of the internal permanent magnet (IPM) inside the capsule and $\mathbf{p}_{\mathrm{epm}}$ and $\mathbf{m}_{\mathrm{epm}}$ are the position vector and the dipole moment of the external permanent magnet (EPM). A cost function incorporating this equation is minimized to compute the 5 DOF pose of the two magnets. The authors demonstrated the feasibility of the system with an experimental setup where a human operator manually moved the actuating magnet to manipulate the capsule while using the localization system as feedback. The operator was tasked to guide the capsule to predetermined locations, after which, errors were computed. The average position error was 1.2 mm but the update rate of the system was 7 Hz. Furthermore, the feasibility of the system with larger actuating magnets, as would be used in realistic scenarios, was not assessed.

3.4.3.3 Localization with Internal Sensors

While adding internal sensors increases the complexity of a CE, it extends the capability of the overall system and offers significant benefits. Unlike most localization

systems with external sensors, which could only achieve 5 DOF localization, 6 DOF has been demonstrated by many researchers using CE with internal sensors. We note that closed-loop control can be achieved with only 5 DOF; however, in most CE applications, it is expected that the operator commands the motion of the CE based on camera feedback. Consequently, we can think of the camera view as the frame of reference for the operators' command. Hence, in order to create an intuitive user interface that maps the operator's input to the correct capsule motion, the full 6 DOF pose needs to be known. In addition, the use of internal sensors allows for creating localization systems more amenable to magnetic actuation. The fact that closed-loop control using permanent magnets has only been demonstrated using this scheme affirms this point.

Furthermore, internal sensor based localization systems typically require much fewer sensors, which can simplify the construction and calibration processes. With fewer constraints on the size and power of the external sources of magnetic fields, these sensors can achieve higher signal to noise ratios than the sensors in localization systems with external sensors.

Researchers have explored different ways of generating magnetic fields externally as well as sensing them inside the capsule. The sensors can be miniature induction coils, which measure AC magnetic fields, or DC sensors such as Hall effect or AMR sensors. Additional sensors such as accelerometers and gyroscopes have also been used by some researchers [127, 34, 33]. In systems where the capsule contains an internal permanent magnet, DC sensors must be placed strategically so as to not be saturated. The placement of the sensors for cylindrical internal permanent magnets (IPMs) was suggested by Miller et al. [96], who showed that there are a number of points in the vicinity of the magnet where the sensing axis of their Hall effect sensors can be placed orthogonal to magnetic field vector at the point. This assured that the Hall effect sensor was primarily sensitive to external magnetic fields and that

the small fields from the internal magnet, unavoidable due to alignment errors, can be subtracted off as biases. It is worth mentioning, however, that AMR sensors are incompatible with such capsules due to their low saturation point.

External magnetic fields can be generated with permanent magnets or electromagnets. Though their rotation can generate AC magnetic fields, permanent magnets are typically used in conjunction with DC sensors, which are usually capable of sensing low frequency fields. Electromagnets can be used to generate higher frequency magnetic fields that do not interfere with low frequency magnetic fields that are used for actuation. In such cases, miniature induction coils are used for sensing. An example of this was introduced in 2003 by Plotkin and Paperno [113], who developed a localization system with an 8×8 array of transmitter coils with a miniature coil (0.9 mm diameter, 3 mm length) inside the capsule as a magnetic field sensor (Figure 3.15). The transmitters were sequentially activated by an AC current at an excitation fre-

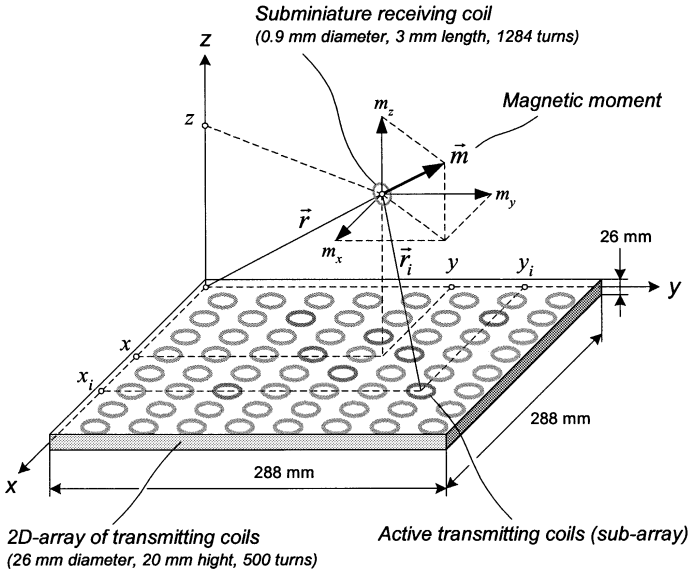

Figure 3.15: A miniature induction coil is used as a sensor by Plotkin and Paperno [113] to receive the magnetic field generated by an 8×8 array of transmitters at an excitation frequency of 50 kHz. *Reproduced with permission from [113] © 2003 IEEE.*

quency of 50 kHz. The magnetic field generated by the transmitters induced voltages on the receiving coil, which were measured by a precise electronic circuit inside the

capsule. The algorithm to determine the pose of the capsule followed the nonlinear minimization method outlined earlier. The cost function was defined as the sum of the errors between the measured and calculated magnetic fields at the capsule. The point dipole model was used to calculate the magnetic fields and the LM algorithm was used for minimization. Since the coil can only measure the magnetic field at a single direction, the projection of the magnetic field onto the dipole moment of the coil was used. This also implied that the system could only achieve 5 DOF localization. Nevertheless, the system achieved remarkable accuracy with maximum error of 1.1 mm in position and 0.8° in orientation at an update rate of 50 Hz. However, compatibility with magnetic actuation was not addressed.

Islam and Fleming [63] improved on the idea of using coils as sensors to create a 6 DOF localization system. Since this could not be accomplished using a single axis coil, as used by Plotkin and Paperno [113], they designed a novel rectangular shaped 3 axis sensing coil. And, instead of an array of transmitter coils, they used a single assembly of 3 orthogonal coils. The authors omitted which algorithm they used or the update rate achieved, but their experiments showed average errors of 6 mm in position and 1.11° in orientation with a sensing range higher than 250 mm. Though they hypothesized that the system was compatible with magnetic actuation, it was not experimentally validated in conjunction with localization.

Commercially available magnetic trackers such as NDI's Aurora tracker operate in a similar manner [102]. Their highly calibrated products can achieve sub-millimeter and sub-degree accuracies with update rates exceeding 40 Hz, but they do not work well when there are other ferromagnetic objects in the environment. Even worse accuracies are expected if the sensor is brought near a permanent magnet, as would be the case for magnetically actuated CE. Thus, they are not compatible with magnetic actuation.

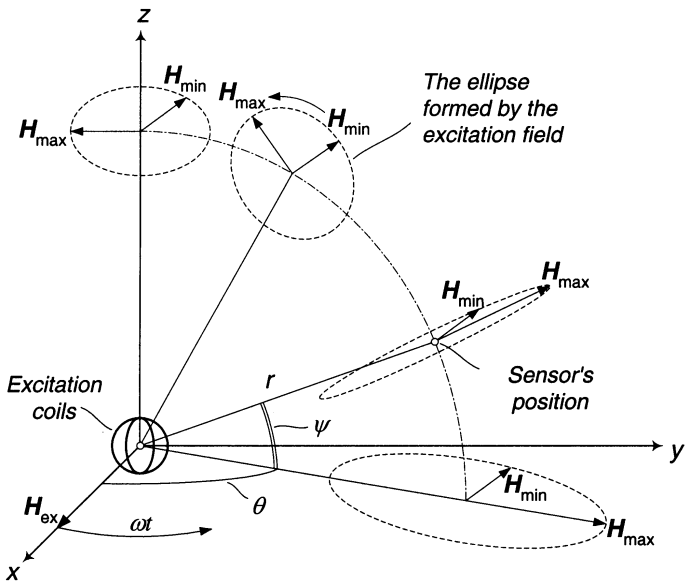

Figure 3.16: Elliptical rotation of magnetic fields generated by orthogonal coils excited with phase quadrature currents. *Reproduced with permission from [105] © 2001 IEEE.*

The use of rotational magnetic fields as an alternative technique was proposed by several researchers [105, 75, 116, 117]. In particular, Paperno et al. [105], showed that if two mutually orthogonal coils were excited with phase quadrature currents, the resulting magnetic field at any point in the localization region rotates elliptically as shown in Figure 3.16. This ellipse was uniquely parameterized by its aspect ratio, size, phase, and orientation. From these parameters, the 6 DOF pose of a 3D magnetic field sensor can be recovered. Inspired by these findings, Popek et al. [116] developed a localization system using a single external rotating permanent magnet and a capsule with an IPM and 6 Hall effect sensors placed strategically so as to not be saturated by the magnetic field of the IPM. As noted by Paperno et al. [105], the rotation of the external permanent magnet was equivalent to the two mutually orthogonal coils being excited with phase quadrature currents; thus, the same elliptical rotation of the magnetic field was induced. With the use of analytical expressions relating the minimum and maximum field magnitudes of a point dipole magnetic field with the induced ellipse, the authors were able to calculate the 6 DOF pose of the capsule.

Experimental results showed that the system had a total error of 11 mm in position and 11° in orientation with an update rate of 20 Hz when the capsule was allowed to rotate freely with the rotating external magnet. The same authors improved the accuracy of the system to 4.9 ± 2.7 mm and $3.3 \pm 1.7°$ by using magnetic field measurements of the entire ellipse instead of the minimum and maximum magnitudes in a nonlinear cost function minimized using the LM algorithm [117]. To demonstrate that the accuracy was sufficient for magnetic propulsion, the authors designed a proof-of-concept spiral propulsion system. A robot manipulator carrying a spherical permanent magnet that could rotate in all 3 directions propelled the capsule through straight and curved lumens. However, propulsion had to be paused in order to perform localization as the localization algorithm assumed no net motion of the capsule during a sampling period.

Relevant to direct propulsion, and this dissertation, Salerno et al. [127] demonstrated that an EPM mounted on a robotic manipulator, together with magnetic field and inertial sensors inside the capsule, can be used for estimating the position of the capsule. Their approach however was not real-time and required the separation of actuation and pose estimation steps. Di Natali et al. [34] improved upon this system by creating an efficient algorithm that exploited the axial symmetry of cylindrical magnets to create a real-time 6 DOF pose estimation system. In their approach, the capsule had 6 Hall effect sensors in an arrangement that approximated a pair of 3-axis Hall Effect sensors separated by a known distance (Figure 3.17). Inertial sensors were also available and were used to rotate sensor readings into the reference frame of the EPM. A look-up table mapping a uniform grid of positions in cylindrical coordinates to magnetic field vectors was generated offline using a finite element method (FEM) software according to the magnetic current model shown in Equation (3.6). The authors took advantage of the azimuthal symmetry of the EPM to reduce the dimension of the look-up table to a plane (Figure 3.18). During operation, the yaw angle of the

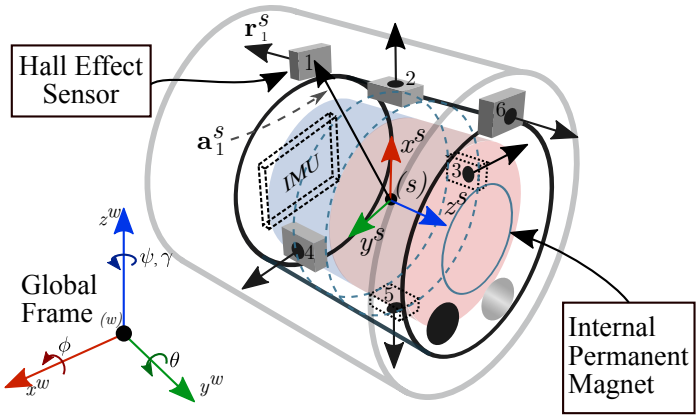

Figure 3.17: Placement of Hall effect sensors on the capsule to approximate pairs of 3-axis sensors.

capsule is first initialized to a known value. For each magnetic field measurement, a sequential search of the look-up table is performed to find the two points that closely matched the measured magnetic fields from each pair of Hall effect sensors. The average of these two points is taken as the center of the capsule. A new yaw angle is then calculated based on the line segment between the two points. Experimental results showed that the system had an update rate of 71 Hz and within a spherical workspace of 150 mm in radius, average errors were below 5 mm and 19° for position and orientation respectively.

With the aim of improving the update rate, the same authors [33] proposed an iterative method where small changes in magnetic field were linearly mapped to small changes in position by the Jacobian of Equation (3.6):

$$\frac{\partial \mathbf{B}(\mathbf{p})}{\partial \mathbf{p}} = J = \begin{bmatrix} \frac{\partial B_x}{\partial p_x} & \frac{\partial B_x}{\partial p_y} & \frac{\partial B_x}{\partial p_z} \\ \frac{\partial B_y}{\partial p_x} & \frac{\partial B_y}{\partial p_y} & \frac{\partial B_y}{\partial p_z} \\ \frac{\partial B_z}{\partial p_x} & \frac{\partial B_z}{\partial p_y} & \frac{\partial B_z}{\partial p_z} \end{bmatrix} \tag{3.12}$$

In order to efficiently compute this Jacobian, a map that relates positions in cylindrical coordinates to Jacobians was generated by taking the gradients of an interpolated

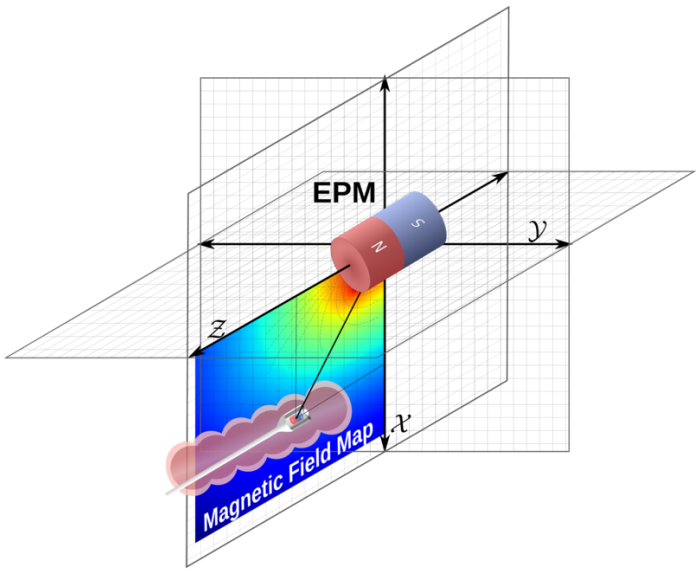

Figure 3.18: Localization based on a 2D look-up table of magnetic field vectors.

magnetic field model. Modal representation was used to express the parameters of the interpolation and a matrix of coefficients was computed offline using least-squares fitting. During operation, the position and yaw angle were first initialized to known values. Designating a measured magnetic field vector as $\mathbf{B}_s$, for each iteration, changes in magnetic field were computed as $\mathbf{\Delta B}_s = \mathbf{B}_{s,\text{new}} - \mathbf{B}_{s,\text{old}}$. The new position was then determined as:

$$\mathbf{p}_{\text{new}} = \mathbf{p}_{\text{old}} + J^{-1}\mathbf{\Delta B}_s \tag{3.13}$$

The orientation was determined by applying inertial navigation algorithms on accelerometer and gyroscope measurements. The iterative approach rendered an update rate faster than 100 Hz. The average localization errors, expressed in cylindrical coordinates, were below 7 mm in both the radial and axial components, and 5° in the azimuthal component.

3.4.4 Magnetic Field Based Localization Summary

Despite the abundance of localization techniques, only few have been implemented and demonstrated on real magnetically actuated CE [145, 33, 115]. In particular, the methods presented by Di Natali et al. [34, 33] are compatible with direct propulsion, which is the type of propulsion used in the Magnetically Actuated Capsule (MAC) system described in Chapter 2. In contrast to Popek et al. [117], where propulsion and localization had to be decoupled, these methods provide continuous localization while maintaining compatibility with magnetic actuation. Since the same magnet used for actuation is also used for localization, the complexity of the overall system is limited to the construction of the capsule.

It is important to note that the workspace volumes specified in these systems have a different interpretation than the localization systems based on a stationary arrangement of magnetic field sources or sensors. In these systems, the workspace is defined as a static region in which localization of the capsule can be achieved. In contrast, in the localization systems proposed by Di Natali et al. [34, 33] and Popek et al. [117, 115], a robot manipulator is employed to carry the external permanent magnet used for actuation and localization. This implies that, even though the workspace is defined as a static region centered on the magnet, since the pose of the magnet is known from the forward kinematics of the robot, the overall system has a mobile workspace. This can be used to create an adaptive localization system that avoids the performance degradation observed in some localization systems when the capsule reached the boundary of the localization region.

However, after repeated use of the techniques described by Di Natali et al. [34, 33] in practical settings, we have discovered two drawbacks that limit their viability for future clinical use: (1) singularities in certain regions of the workspace leading to the loss of estimation capability and (2) the dependence on accurate yaw angle initialization and sensitivity to yaw drift leading to reduced accuracy in the estimated

pose when yaw angle errors are present. These issues will be discussed in detail in Chapter 4.

CHAPTER 4

Enhanced Real-Time Pose Estimation for Magnetically Actuated Capsule Endoscopes

4.1 Introduction

In order to apply the necessary forces and torques, magnetic actuation systems need accurate estimates of the capsule's pose. Despite their high levels of accuracy, commercially available electromagnetic tracking systems such as the NDI Aurora (Northern Digital Inc., Waterloo, ON, Canada) and the Ascension trakSTAR (Ascension Technology, Burlington, VT, USA) are incompatible with magnetic actuation due to magnetic distortions caused by the magnets found in the capsule and the actuator [44].

As such, several groups have proposed pose estimation methods with varying degrees of accuracy, workspace size, estimation time, and achievable degrees of freedom as discussed in Section 3.4. A subset [127, 34, 33, 114, 3] of these methods have contributed to the recent advances in robotically guided magnetic capsule endoscopy where trajectory following [152, 117] and automation of repetitive endoscopic maneuvers [138] were demonstrated.

In particular, Salerno et al. [127] demonstrated that an external permanent magnet (EPM) mounted on a robot manipulator, together with magnetic field and inertial sensors inside the capsule, can be used for estimating the position of the capsule. Their approach however was not real-time and required the separation of actuation and pose estimation steps. Di Natali et al. [34] improved upon this system by creating an efficient algorithm that exploited the axial symmetry of cylindrical magnets to create a real-time 6 degrees of freedom (DOF) pose estimation system. They also

provided a more computationally efficient iterative algorithm with an update rate faster than 100 Hz [33].

A thorough analysis of the workspace of the aforementioned real-time pose estimation methods [34, 33] identifies singularities in certain regions of the workspace leading to the loss of estimation capability. The assumption made in these algorithms is that for a given pose of the EPM, there is a bijective mapping from all positions in the workspace to magnetic field vectors and that changes in magnetic field always occur for changes in position. We show in the next section that this assumption fails to hold on the singularity plane of the EPM defined as the plane normal to the dipole moment that passes through the center of the magnet (see Figure 4.2). Certain applications of robotically guided magnetic capsule endoscopy require the capsule to be naturally located in this region during clinical procedures, thus, this limitation hinders future clinical use of these devices [151, 152, 138, 90]. This problem requires additional sources of information to constrain the number of solutions found by the algorithms. Further drawbacks of these pose estimation methods come from the need

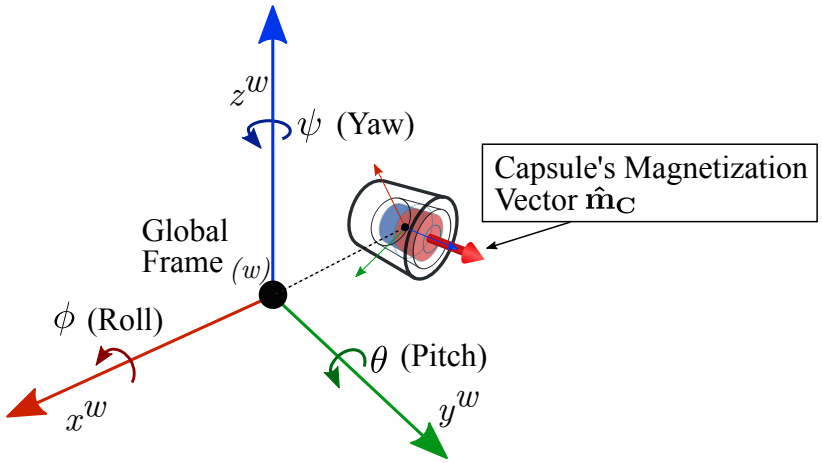

Figure 4.1: Definition of roll (ϕ), pitch (θ), and yaw (ψ) angles.

for accurate initialization of the capsule's yaw angle (see Figure 4.1) with respect to a global frame and the susceptibility of the estimated yaw angle to drift. Yaw angle errors arising from these issues lead to reduced accuracy in the overall estimated pose.

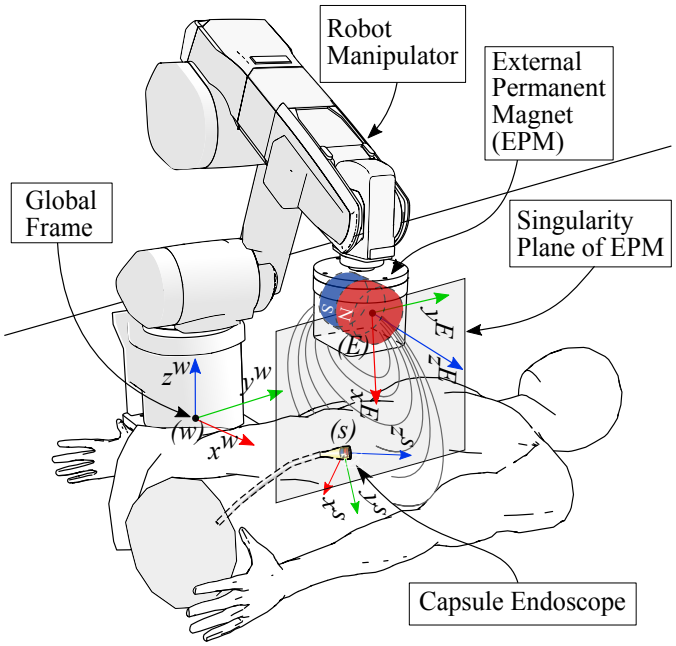

Figure 4.2: Application scenario of active magnetic manipulation of a capsule endoscope using a permanent magnet mounted at the end effector of a robot manipulator.

Unlike pitch and roll angles, which are determined from the acceleration due to gravity, this issue exists for the yaw angle owing to the strong magnetic field from the EPM rendering the earth's magnetic field unusable as an absolute reference. Aside from the inconvenience of performing accurate initializations every time the software is started, it is important to consider the implications in clinical settings. That is, if the algorithm is restarted for any reason during a procedure, it will be extremely difficult to reinitialize the yaw angle while the capsule is inside a patient.

Our solution employs a hybrid system that combines static and time-varying magnetic field sources to create a robust and clinically viable magnetic pose estimation method for robotically guided magnetic capsule endoscopy. While our method is described in the context of solving the singularity and yaw initialization problems in the specific magnetically actuated soft-tethered capsule endoscopy system shown in Figure 4.2, the approach presented here can be applied to other tethered and untethered devices. Furthermore, we note that any source of magnetic field that, for the

purpose of actuation, can be sufficiently approximated by the point-dipole magnetic field model exhibits the singularity described in the next section. This affects any pose estimation method that uses a single source of magnetic field with the exception of methods that make multiple measurements while rotating or translating the magnet, such as the one used by [117]. Therefore, the methods described herein can be adopted in other systems with different schemes of magnetic actuation. The assumption we make is that, similar to the capsules in [127, 34, 33], our capsule contains one inertial measurement unit (IMU) and at least three single axis magnetic field (Hall effect) sensors arranged orthogonally so as to measure the magnetic field in all three axes. While it is further assumed that the capsule contains a permanent magnet in order to enable magnetic actuation, our method can be used in applications where this internal magnet is not necessary [9]. An additional contribution of our work stems from our use of a state estimation technique based on a parallel implementation of a particle filter to combine all available sensor information in a stochastic framework.

4.2 Background

A summary of the pose estimation methods described in [34] and [33] was given in Section 3.4.4. Here, the problems of singularity regions and yaw initialization are explained in further detail. Hereafter, bold letters indicate vectors ($\mathbf{v}$) or vector valued functions ($\mathbf{B}$), a hat over a bold letter indicates a unit vector ($\hat{\mathbf{v}}$), and except otherwise stated, an uppercase italicized letter indicates a matrix (M). I denotes the identity matrix.

In both methods of pose estimation, the capsule has six Hall Effect sensors in an arrangement that approximates a pair of 3-axis Hall Effect sensors separated by a known distance. Inertial sensors are also available and are used to rotate sensor readings into the frame of the EPM.

4.2.1 Limitations of Existing Pose Estimation Methods

For theoretical analysis, without any loss of generality, we will assume the EPM is an axially magnetized cylindrical magnet, but the principles of singularity described herein apply to all magnets that can sufficiently be approximated by a dipole model. The magnetic field of the EPM, $\mathbf{B_E} : \mathbb{R}^3 \to \mathbb{R}^3$, is then given by:

$$\mathbf{B_E}(\mathbf{p}) = \frac{\mu_\mathbf{0} \left\|\mathbf{m_E}\right\|}{\mathbf{4}\pi \left\|\mathbf{p}\right\|^\mathbf{3}} (\mathbf{3}\hat{\mathbf{p}}\hat{\mathbf{p}}^\top \hat{\mathbf{m}}_\mathbf{E} - \hat{\mathbf{m}}_\mathbf{E}) \tag{4.1}$$

where $\mathbf{p}$ is the vector from the EPM to the capsule, $\hat{\mathbf{p}} = [\hat{p}_x \quad \hat{p}_y \quad \hat{p}_z]^\top$ is the unit vector along $\mathbf{p}$, and $\mathbf{m}_E$ is the dipole moment of the EPM. Since the accuracy of this model increases as $||\mathbf{p}||$ gets larger [108], it is adequate for characterizing singularity regions.

4.2.1.1 Regions of Magnetic Field Singularity:

Assuming the orientation of the capsule is accurately determined, position estimation can be expressed by the nonlinear inverse problem $\mathbf{B_E^{-1}}(\mathbf{p})$. A region of singularity is where infinite solutions exist to this problem. Let $\mathcal{P}_s$ designate the plane that is normal to the dipole moment and passes through the center of the EPM, *i.e.*, $\mathcal{P}_s = \{\mathbf{p}_s \in \mathbb{R}^3 \mid \mathbf{p}_s^\top \hat{\mathbf{m}}_\mathbf{E} = 0\}$. On this plane, we have:

$$\mathbf{B_E}(\mathbf{p}) = -\frac{\mu_0 \left\|\mathbf{m_E}\right\|}{4\pi \left\|\mathbf{p}\right\|^3} \hat{\mathbf{m}}_\mathbf{E} \tag{4.2}$$

$$\widehat{\mathbf{B_E}(\mathbf{p})} = -\hat{\mathbf{m}}_\mathbf{E} \tag{4.3}$$

$$||\mathbf{B_E}(\mathbf{p})|| = \frac{\mu_0 \left\|\mathbf{m_E}\right\|}{4\pi \left\|\mathbf{p}\right\|^3} \tag{4.4}$$

Since $\widehat{\mathbf{B_E}(\mathbf{p})}$ is constant in the EPM frame and $||\mathbf{B_E}(\mathbf{p})||$ changes only when $\|\mathbf{p}\|^3$ changes, the set of solutions to $\mathbf{B_E^{-1}}(\mathbf{p})$ is a circle of radius r on $\mathcal{P}_s$ defined as

$$\mathbf{C}_s = \{\mathbf{c}_s \in \mathcal{P}_s \mid ||\mathbf{c}_s|| = r\}.$$

That is, when the capsule is located on $\mathcal{P}_s$, there exist an infinite number of vectors of equal magnitude and direction forming a circle $\mathbf{C}_s$ on $\mathcal{P}_s$ and centered on the EPM, as shown in Figure 4.3, rendering infinite solutions to $\mathbf{B_E^{-1}}(\mathbf{p})$. Therefore, additional information is required to constrain the solution to a single pose.

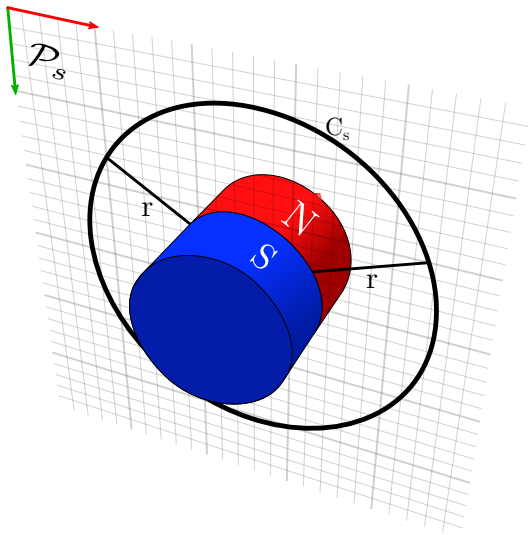

Figure 4.3: Circle formed by magnetic field vectors of equal magnitude and direction on the singularity plane $\mathcal{P}_s$.

Additional insight as to where the regions of singularity occur can be gained by analyzing the Jacobian, J, of Equation (4.1) with respect to $\mathbf{p}$. Figure 4.4 shows the condition number of J, defined as the ratio of the maximum and minimum singular values of J, *i.e.*, $\kappa(J) = \frac{\sigma_{max}(J)}{\sigma_{min}(J)}$ on three different planes including $\mathcal{P}_s$. As indicated by the colors in the figure, J becomes ill-conditioned near $\mathcal{P}_s$ and becomes singular on $\mathcal{P}_s$ while the planes parallel to $\mathcal{P}_s$ but farther from the center of the magnet are non-singular.

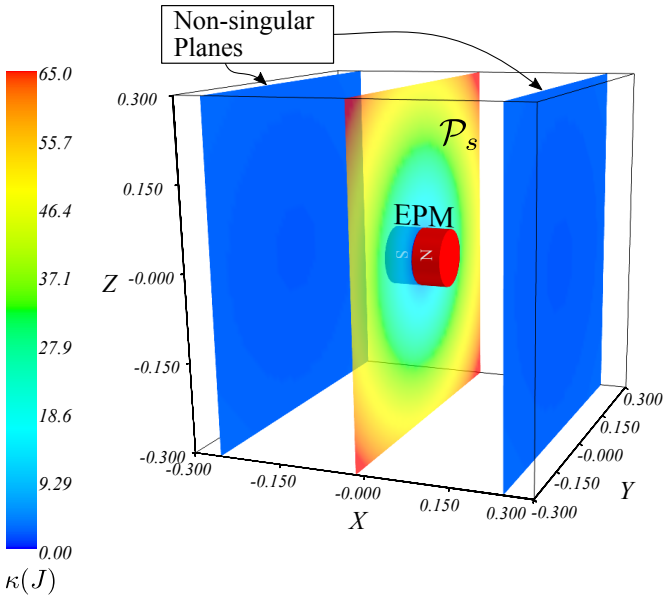

Figure 4.4: Regions of magnetic field singularity as indicated by high condition numbers of the Jacobian matrix. Note that the plot shows a plane near the singularity plane $\mathcal{P}_s$ because the condition number on $\mathcal{P}_s$ is infinite. Two other planes parallel to $\mathcal{P}_s$ are displayed to show that the singularity region only exists near the center of the magnet.

4.2.1.2 Yaw Angle Initialization:

Both algorithms in [34] and [33] require the accurate initialization of the yaw angle. Since both algorithms depend on converting the measured magnetic fields from the capsule's reference frame to the EPM's reference frame, the solutions found by the algorithms are sensitive to yaw angle errors. As discussed earlier, both algorithms use an incremental approach to estimate the yaw angle and are prone to sensor noise with errors increasing with longer periods of use.

To determine the sensitivity of these algorithms to yaw angle error, Monte Carlo simulations were performed at random positions in a 300 mm × 300 mm × 150 mm workspace centered on the EPM. Position errors were obtained by computing the distance between the true position of the test point from the simulated point. At each point, the yaw angle error ranged from 0° to 5°. As shown in Figure 4.5, distance errors can be as high as 15 mm in some regions of the workspace for a yaw angle error

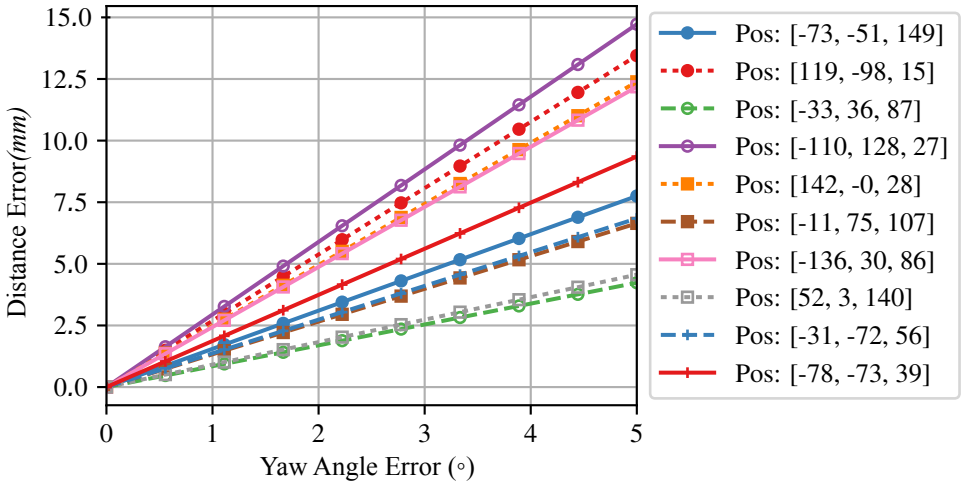

Figure 4.5: Position error as a function of yaw error. The errors can be as high as 15 mm in some regions of the workspace for a yaw angle error of 5°.

of 5°. While an error of 15 mm might be acceptable for closed-loop control, with the addition of errors from sensor bias and noise, the total error might be much higher. Furthermore, although it can be argued that one can initialize the yaw angle to within 5° of the true yaw, accurate initialization of the yaw angle can be very difficult in clinical settings after a procedure has been started. The pose estimation methods in [34] and [33] would require the capsule be removed from the patient, reinitialized, and reinserted leading to prolonged procedure times.

4.3 Our Approach

4.3.1 Hybrid Magnetic Field

As shown in Figure 4.6, if we augment the system with an electromagnetic coil that generates a weak time-varying magnetic field and attach it to the EPM such that their dipole moments are orthogonal, the static field of the EPM and the time-varying field of the coil can be used simultaneously to obtain an additional set of equations that allow for solving for the position and yaw angle of the capsule.

Orthogonal collocation of the EPM and the electromagnetic coil ensures that in the singularity region of the EPM, the magnetic field of the coil is always orthogonal to the magnetic field of the EPM. If instead the coil was placed at a fixed location, *e.g.* embedded in the surgical table, it would be possible for the dipole moments of the EPM and the coil to become aligned during magnetic manipulation. If this alignment were to happen in the singularity region of the EPM, the number of available equations for solving the inverse problem would be reduced. As a result, the singularity problem remains unmitigated. Another benefit of collocation is that it allows for a dynamic workspace that moves with the actuating magnet. This ensures that an adequate signal to noise ratio is maintained at the location of the capsule without requiring a large coil.

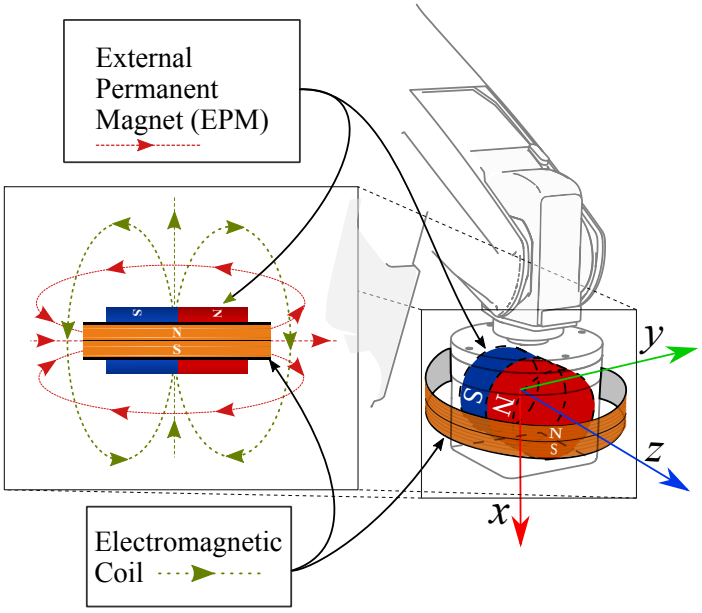

Figure 4.6: EPM augmented with an electromagnetic coil.

For a given workspace, the time-varying field is made strong enough to be detected by the magnetic field sensors in the capsule without inducing enough force and torque to physically affect the capsule's pose. A time-varying signal is used in order to measure the magnetic fields of the EPM and the coil separately. In contrast, if two static magnetic fields were used, it would not be possible to make separate measurements

owing to the principle of superposition where the vector sum of the magnetic fields is measured. This is not desirable as it reduces the number of available equations. Goertzel's tone-detection algorithm [48, 163] is used to extract the magnitude and phase of the time-varying signal for each sensor. The measured values are assembled to create a vector that allows us to treat the coil as if it were another permanent magnet with the same origin as the EPM.

For the following analysis, measured magnetic fields from the EPM ($\mathbf{b}^s_{\mathbf{E}}$) and electromagnetic coil ($\mathbf{b}^s_{\mathbf{C}}$) are rotated to the EPM frame by the following expression:

$$\mathbf{b}_{\mathbf{E}} = R^E_w R^w_s \mathbf{b}^s_{\mathbf{E}} \tag{4.5}$$

$$\mathbf{b}_{\mathbf{C}} = R^E_w R^w_s \mathbf{b}^s_{\mathbf{C}} \tag{4.6}$$

For notational convenience, we omit the frame designator, $(\cdot)^E$, for vectors expressed in the EPM frame (see Figure 4.7). The rotation matrix R^E_w represents the rotation of

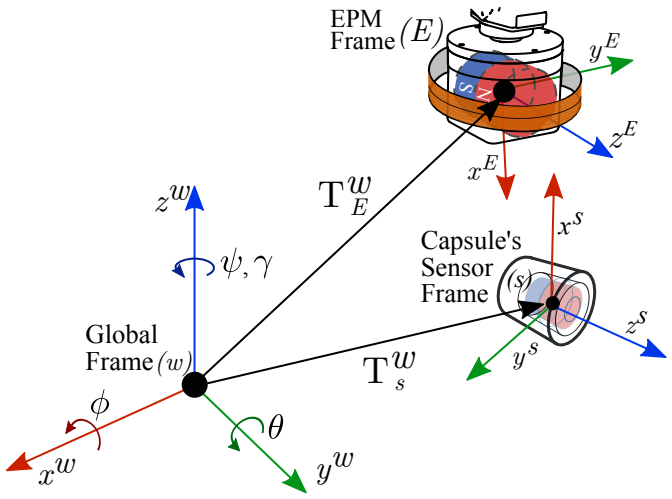

Figure 4.7: Coordinate frames of the magnetic pose estimation system showing the global frame (w), the capsule's sensor frame (s) and the EPM frame (E).

the world frame (w) with respect to the EPM frame (E) and is assumed to be known from the robot manipulator. R^w_s is the rotation of the capsule's sensor (s) frame with respect to the world frame. Due to yaw angle initialization errors, R^w_s is unknown

and has to be solved for in our algorithm. It is useful to view this matrix as:

$$R_s^w = R_z(\gamma)\tilde{R}_s^w \tag{4.7}$$

where

$$R_z(\gamma) = \begin{bmatrix} \cos(\gamma) & -\sin(\gamma) & 0 \\ \sin(\gamma) & \cos(\gamma) & 0 \\ 0 & 0 & 1 \end{bmatrix}, \tag{4.8}$$

$\tilde{R}_s^w$ is the rotation of the capsule's sensor frame (s) with respect to the world frame (w) computed using inertial measurements, and γ is the yaw angle error. The tilde symbol ($\tilde{\cdot}$) is used to indicate that there is yaw angle error in the rotation matrix.

Incorporating the capsule orientation and the new additional magnetic field, the new system of equations is given by:

$$R_w^E R_z(\gamma)\tilde{R}_s^w \mathbf{b}_{\mathbf{E}}^s = \mathbf{B}_{\mathbf{E}}(\mathbf{p}) \tag{4.9}$$

$$R_w^E R_z(\gamma)\tilde{R}_s^w \mathbf{b}_{\mathbf{C}}^s = \mathbf{B}_{\mathbf{C}}(\mathbf{p}) \tag{4.10}$$

where

$$\mathbf{B}_{\mathbf{E}}(\mathbf{p}) = \frac{\mu_0 \left\|\mathbf{m}_{\mathbf{E}}\right\|}{4\pi \left\|\mathbf{p}\right\|^3}(3\hat{\mathbf{p}}\hat{\mathbf{p}}^\top \hat{\mathbf{m}}_{\mathbf{E}} - \hat{\mathbf{m}}_{\mathbf{E}}) \tag{4.11}$$

$$\mathbf{B}_{\mathbf{C}}(\mathbf{p}) = \frac{\mu_0 \left\|\mathbf{m}_{\mathbf{C}}\right\|}{4\pi \left\|\mathbf{p}\right\|^3}(3\hat{\mathbf{p}}\hat{\mathbf{p}}^\top \hat{\mathbf{m}}_{\mathbf{C}} - \hat{\mathbf{m}}_{\mathbf{C}}) \tag{4.12}$$

and $\mathbf{m}_{\mathbf{E}}$ and $\mathbf{m}_{\mathbf{C}}$ are the dipole moments of the EPM and coil respectively. Without any loss of generality, we will assign the dipole moment direction vectors to $\hat{\mathbf{m}}_{\mathbf{E}} = \hat{\mathbf{z}} = [0 \quad 0 \quad 1]^\top$ and $\hat{\mathbf{m}}_{\mathbf{C}} = \hat{\mathbf{x}} = [1 \quad 0 \quad 0]^\top$. Substituting into Equation (4.9) and Equation (4.10) and simplifying, we have:

$$R_w^E R_z(\gamma)\tilde{R}_s^w \mathbf{b}_{\mathbf{E}}^s = \frac{\mu_0 \left\|\mathbf{m}_{\mathbf{E}}\right\|}{4\pi \left\|\mathbf{p}\right\|^3}(3\hat{p}_z\hat{\mathbf{p}} - \hat{\mathbf{z}}) \tag{4.13}$$

$$R_w^E R_z(\gamma)\tilde{R}_s^w \mathbf{b}_{\mathbf{C}}^s = \frac{\mu_0 \left\|\mathbf{m_C}\right\|}{4\pi \left\|\mathbf{p}\right\|^3}(3\hat{p}_x\hat{\mathbf{p}} - \hat{\mathbf{x}}) \tag{4.14}$$

which expands to

$$R_w^E R_z(\gamma)\tilde{R}_s^w \mathbf{b}_{\mathbf{E}}^s = \frac{\mu_0 \left\|\mathbf{m_E}\right\|}{4\pi \left\|\mathbf{p}\right\|^3} \left(\begin{bmatrix} 3\hat{p}_z\hat{p}_x \\ 3\hat{p}_z\hat{p}_y \\ 3\hat{p}_z^2 - 1 \end{bmatrix} \right) \tag{4.15}$$

$$R_w^E R_z(\gamma)\tilde{R}_s^w \mathbf{b}_{\mathbf{C}}^s = \frac{\mu_0 \left\|\mathbf{m_C}\right\|}{4\pi \left\|\mathbf{p}\right\|^3} \left(\begin{bmatrix} 3\hat{p}_x^2 - 1 \\ 3\hat{p}_x\hat{p}_y \\ 3\hat{p}_x\hat{p}_z \end{bmatrix} \right) \tag{4.16}$$

We analyze these algebraic equations to determine if there are singularities in the hybrid system that would result in infinite solutions to the inverse problem of finding the pose given magnetic field measurements. We do not imply that the equations can be used directly to solve for the unknowns. Nevertheless, the analysis, without the need for extensive simulations, shows that an additional magnet placed orthogonally gives enough information so that a nonlinear solver can find a unique solution. However, the analysis does not take into account the stochastic nature of the signals; therefore, for practical implementation, we use the particle filter based state estimator described later in Section 4.3.2.

In most cases, the system is over-determined and the unknown values can be solved. However, due to the symmetry of magnetic fields, it is possible to find more than one solution to the system of equations, yet the number of solutions is always finite. Further, multiple solutions due to symmetry exist in disjoint regions of the workspace making it possible to choose proper solution based on previous poses of the capsule.

From Equation (4.13) and Equation (4.14), we note that if γ is known as a result of accurate initialization as assumed in [34, 33], the singularity problem is eliminated.

That is, if either $\hat{p}_x = 0$ or $\hat{p}_z = 0$, Equation (4.13) or Equation (4.14) can be used to estimate the capsule's position respectively. If both $\hat{p}_x$ and $\hat{p}_z$ are zero, we immediately know $\hat{p}_y = \pm 1$ and $\|\mathbf{p}\|$ can be determined from either Equation (4.13) or Equation (4.14).

If γ is not known, we have three conditions, namely, no singularity, singular region of one magnet (EPM or coil), and singular region of both magnets (EPM and coil):

1. $\hat{p}_x \neq 0$ and $\hat{p}_z \neq 0$: Not in singularity. The system is overdetermined and all unknowns, $\hat{p}_x, \hat{p}_y, \hat{p}_z, \|\mathbf{p}\|$ and γ, can be solved.

2. Either $\hat{p}_x = 0$ or $\hat{p}_z = 0$: The two cases represent singular regions for each magnet. However, $\mathbf{p}$ is only in the singularity region of one of the magnets. We show in either case that all unknowns can be solved.

   (a) $\hat{p}_x = 0$: Applying this constraint, we have:

$$R_w^E R_z(\gamma) \tilde{R}_s^w \mathbf{b}_{\mathbf{E}}^s = \frac{\mu_0 \|\mathbf{m_E}\|}{4\pi \|\mathbf{p}\|^3} \begin{bmatrix} 0 \\ 3\hat{p}_z \hat{p}_y \\ 3\hat{p}_z^2 - 1 \end{bmatrix} \tag{4.17}$$

$$R_w^E R_z(\gamma) \tilde{R}_s^w \mathbf{b}_{\mathbf{C}}^s = \frac{\mu_0 \|\mathbf{m_C}\|}{4\pi \|\mathbf{p}\|^3} \begin{bmatrix} -1 \\ 0 \\ 0 \end{bmatrix} \tag{4.18}$$

$$\left\| R_w^E R_z(\gamma) \tilde{R}_s^w \mathbf{b}_{\mathbf{E}}^s \right\| = \frac{\mu_0 \|\mathbf{m_E}\|}{4\pi \|\mathbf{p}\|^3} \sqrt{3\hat{p}_z^2 + 1} \tag{4.19}$$

$$\left\| R_w^E R_z(\gamma) \tilde{R}_s^w \mathbf{b}_{\mathbf{C}}^s \right\| = \frac{\mu_0 \|\mathbf{m_C}\|}{4\pi \|\mathbf{p}\|^3} \tag{4.20}$$

We note that $\|\mathbf{p}\|$ can be solved from Equation (4.20) since

$$\left\| R_w^E R_z(\gamma) \tilde{R}_s^w \mathbf{b}_{\mathbf{C}}^s \right\| = \|\mathbf{b}_{\mathbf{C}}^s\| .$$

$\hat{p}_z$ can then be solved from Equation (4.19), and $\hat{p}_y$ can be solved from the unity constraint $\|\hat{\mathbf{p}}\| = 1$. Although multiple solutions are possible for $\hat{p}_y$ and $\hat{p}_z$ due to the square root terms, as mentioned earlier, workspace and continuity constraints can be used to eliminate wrong solutions. Since only γ is left unknown, it can be solved as the angle between the measured and calculated magnetic field vectors projected on the xy-plane. A more robust solution can be found by casting it as a least squares optimization problem,

$$\gamma = \underset{R_z(\gamma)\in\mathbb{SO}(3)}{\arg\min} \left\| R_z(\gamma) P \tilde{R}_s^w \mathbf{b}_{\mathbf{E}}^s - P {R_w^E}^\top \mathbf{B}_{\mathbf{E}}(\mathbf{p}) \right\|^2 + \left\| R_z(\gamma) P \tilde{R}_s^w \mathbf{b}_{\mathbf{C}}^s - P {R_w^E}^\top \mathbf{B}_{\mathbf{C}}(\mathbf{p}) \right\|^2 \tag{4.21}$$

where P is a projection matrix onto the xy-plane and $\mathbf{B}_{\mathbf{E}}(\mathbf{p})$ and $\mathbf{B}_{\mathbf{C}}(\mathbf{p})$ are the calculated magnetic field vectors at $\mathbf{p}$, which has already been determined. A well known closed form solution for Equation (4.21) can be found in the literature [7].

(b) $\hat{p}_z = 0$: Similarly, we have:

$$R_w^E R_z(\gamma) \tilde{R}_s^w \mathbf{b}_{\mathbf{E}}^s = \frac{\mu_0 \|\mathbf{m}_{\mathbf{E}}\|}{4\pi \|\mathbf{p}\|^3} \begin{bmatrix} 0 \\ 0 \\ -1 \end{bmatrix} \tag{4.22}$$

$$R_w^E R_z(\gamma) \tilde{R}_s^w \mathbf{b}_{\mathbf{C}}^s = \frac{\mu_0 \|\mathbf{m}_{\mathbf{C}}\|}{4\pi \|\mathbf{p}\|^3} \begin{bmatrix} 3\hat{p}_x^2 - 1 \\ 3\hat{p}_x \hat{p}_y \\ 0 \end{bmatrix} \tag{4.23}$$

$$\left\| R_w^E R_z(\gamma) \tilde{R}_s^w \mathbf{b}_{\mathbf{E}}^s \right\| = \frac{\mu_0 \|\mathbf{m}_{\mathbf{E}}\|}{4\pi \|\mathbf{p}\|^3} \tag{4.24}$$

$$\left\| R_w^E R_z(\gamma) \tilde{R}_s^w \mathbf{b}_{\mathbf{C}}^s \right\| = \frac{\mu_0 \|\mathbf{m}_{\mathbf{C}}\|}{4\pi \|\mathbf{p}\|^3} \sqrt{3\hat{p}_x^2 + 1} \tag{4.25}$$

Here, $\|\mathbf{p}\|$ can be solved from Equation (4.24). $\hat{p}_x$ can then be solved from Equation (4.25) and $\hat{p}_y$ from the unity constraint $\|\hat{\mathbf{p}}\| = 1$. Finally γ can be found using Equation (4.21).

3. $\hat{p}_x = 0$ and $\hat{p}_z = 0$: This condition occurs when $\mathbf{p}$ is in the singularity region of both magnets. From the unity constraint, $\hat{p}_y = \pm 1$. After substitution, we have:

$$R_w^E R_z(\gamma) \tilde{R}_s^w \mathbf{b}_{\mathbf{E}}^s = \frac{\mu_0 \|\mathbf{m}_{\mathbf{E}}\|}{4\pi \|\mathbf{p}\|^3} \begin{bmatrix} 0 \\ 0 \\ -1 \end{bmatrix} \tag{4.26}$$

$$R_w^E R_z(\gamma) \tilde{R}_s^w \mathbf{b}_{\mathbf{C}}^s = \frac{\mu_0 \|\mathbf{m}_{\mathbf{C}}\|}{4\pi \|\mathbf{p}\|^3} \begin{bmatrix} -1 \\ 0 \\ 0 \end{bmatrix} \tag{4.27}$$

$$\left\| R_w^E R_z(\gamma) \tilde{R}_s^w \mathbf{b}_{\mathbf{E}}^s \right\| = \frac{\mu_0 \|\mathbf{m}_{\mathbf{E}}\|}{4\pi \|\mathbf{p}\|^3} \tag{4.28}$$

$$\left\| R_w^E R_z(\gamma) \tilde{R}_s^w \mathbf{b}_{\mathbf{C}}^s \right\| = \frac{\mu_0 \|\mathbf{m}_{\mathbf{C}}\|}{4\pi \|\mathbf{p}\|^3} \tag{4.29}$$

$\|\mathbf{p}\|$ can readily be solved from Equation (4.28) or Equation (4.29) and γ can be found using Equation (4.21).

4.3.2 Magnetic Pose Estimation with Particle Filters

Particle filters or Sequential Monte Carlo (SMC) methods are a class of recursive Bayesian state estimation techniques often used for object tracking and localization [21]. In these methods, the posterior distribution, $p(\mathbf{x}_k|\mathbf{z}_{1:k})$, of the state $\mathbf{x}_k$ at time k conditioned on a time series of measurements $\mathbf{z}_{1:k} = \{\mathbf{z}_i, i = 1, 2, \ldots, k\}$ is represented by a set of point masses or particles with corresponding importance weights, w_k^i. The nonparametric representation of the probability density function (pdf) and the use of Monte Carlo techniques allow particle filters to overcome limiting

assumptions made in other state estimation techniques such as Kalman filters [21], where process and measurement models are linear and noise distributions are Gaussian. Constraints on the state of the system, such as workspace bounds, can also be applied in a more straight forward manner using particle filters.

In this work, we use the sampling importance resampling (SIR) variant of the particle filter [50]. At each time step, the SIR algorithm performs a prediction, which consists of drawing samples from the prior density, $p(\mathbf{x}_k|\mathbf{x}^i_{k-1})$, creating a new set of particles. The process model of the system $\mathbf{x}_k = \mathbf{f}_k(\mathbf{x}^i_{k-1}, \mathbf{v}^i_{k-1})$, where $\mathbf{v}^i_{k-1}$ is the process noise, can be used to generate a sample where the pdf $p(\mathbf{v}^i_{k-1})$ is assumed to be known. The importance weights of the newly sampled particles are then updated based on the likelihood function $p(\mathbf{z}_k|\mathbf{x}^i_k)$, which makes use of the measurement model $\mathbf{z}_k = \mathbf{h}(\mathbf{x}_k, \mathbf{n}_k)$ where $\mathbf{n}_k$ is the measurement noise. After normalization of the importance weights, a resampling step is performed. This step samples from the set of particles with replacement so as to eliminate particles with small weights and reinforce particles with large weights. Resampling is necessary in order to avoid a condition known as "weight degeneracy" or "sample impoverishment" where only a few particles are left with nonzero weights after a few iterations of the algorithm. The resampled set of particles is the discrete approximation of the posterior $p(\mathbf{x}_k|\mathbf{z}_{1:k})$. A more detailed account of particle filters and the SIR algorithm can be found in [6] or [21].

For the present problem of magnetic pose estimation and tracking, we first make use of the complementary filter of Mahony et al. [93] for fusing accelerometer and gyroscope measurements. The output of the filter is an estimate of the capsule's rotation with an unknown yaw offset, γ. The position of the capsule and the yaw angle offset comprise the state, $\mathbf{x}_k = [x \quad y \quad z \quad \gamma]^\top$, to be estimated with respect to a world frame.

4.3.2.1 Process Model:

It is known that using a process model that incorporates actuation control inputs would lead to better state estimation. However, in applications such as magnetically actuated capsule endoscopy, the motion of the object being tracked can be, at times, significantly different from commanded motion due to environmental factors (*e.g.*, capsule trapped in a tissue fold, peristalsis), making it difficult to construct an accurate motion model. In this work, we demonstrate that it is sufficient to use the random walk process model given by:

$$\mathbf{f}_k(\mathbf{x}^i_{k-1}, \mathbf{v}^i_{k-1}) = \mathbf{x}^i_{k-1} + \mathbf{v}^i_{k-1} \tag{4.30}$$

where

$$\mathbf{v}^i_{k-1} \sim \mathcal{N}(0, Q) \tag{4.31}$$

is a sample from a normal distribution and Q is a covariance matrix empirically chosen as a trade-off between convergence speed and jitter of the pose estimate. For our experiments, $Q = \text{diag}(0.0015, 0.0015, 0.0015, 0.01)$

4.3.2.2 Measurement Model:

As shown in Figure 4.9, our system uses six single axis Hall effect sensors positioned in the capsule so as to approximate two triaxial sensors. We use a signal processing technique to separately measure the magnetic fields from the EPM and the electromagnetic coil (see Section 4.4). Given the relative position vector, $\mathbf{a}^s_i$, of each Hall effect sensor from the center of the capsule, the sensor output is computed as the projection of the magnetic field at the sensor in the direction of the sensor's

normal vector, $\mathbf{r}_i^s$.

$$b_{\mathbf{E}_i}^s = \mathbf{r}_i^{s\top} R_E^s \mathbf{B}_\mathbf{E} \left(T_s^E(\mathbf{x}_k^w) \mathbf{a}_i^s \right) \tag{4.32}$$

$$b_{\mathbf{C}_i}^s = \mathbf{r}_i^{s\top} R_E^s \mathbf{B}_\mathbf{C} \left(T_s^E(\mathbf{x}_k^w) \mathbf{a}_i^s \right) \tag{4.33}$$

where $i = 1, 2, \ldots, 6$ and $T_s^E : \mathbb{R}^3 \times \mathbb{S}^1 \to \mathbb{SE}(3)$ is the homogeneous transformation of the capsule's frame with respect to the EPM frame given by:

$$T_s^E(\mathbf{x}^w) = T_w^E T_s^w(\mathbf{x}^w) \tag{4.34}$$

$$= T_w^E \begin{bmatrix} & & x_x \\ & R_z(\gamma)\tilde{R}_s^w & x_y \\ & & x_z \\ \mathbf{0} & & 1 \end{bmatrix} \tag{4.35}$$

and T_w^E is the transformation of the world frame with respect to the EPM frame (see Figure 4.7), which is assumed to be known from the forward kinematics of the robot manipulator. We will denote magnetic field values calculated using Equation (4.32) and Equation (4.33) as $\mathbf{z}_k^* \in \mathbb{R}^{12}$. We assume that our the sensors' noise is normally distributed. Thus, given a set of sensor measurements, $\mathbf{z}_k \in \mathbb{R}^{12}$, our likelihood function is:

$$p(\mathbf{z}_k | \mathbf{x}_k^i) = \frac{1}{(2\pi)^6 |R|^{1/2}} \exp\left(-\frac{1}{2} (\mathbf{z}_k - \mathbf{z}_k^*)^\top W_z R^{-1} W_z (\mathbf{z}_k - \mathbf{z}_k^*) \right) \tag{4.36}$$

where $R \in \mathbb{R}^{12\times12}$ is a covariance matrix that characterizes the noise in the magnetic field sensors and $|\cdot|$ is the determinant operator. $W_z \in \mathbb{R}^{12\times12}$ is a diagonal weight matrix used to normalize the three orders of magnitude difference in the sensor outputs for the EPM and the coil. We found that the presence of W_z in the likelihood function to be of extreme importance. If left out, the likelihood function would be

dominated by the error residuals from the EPM readings because the magnetic fields from the coil are very weak. This amounts to the algorithm completely ignoring the readings from the coil thereby facing the same challenges of singularity of a single EPM described in Section 4.2.1.1.

The choice of a magnetic field model for $\mathbf{B_E}$ and $\mathbf{B_C}$ directly impacts the accuracy of the pose estimate. Choosing the point-dipole model shown in Equation (4.1) would result in reduced accuracy when the capsule is in close proximity to the source of external magnetic field. This is at odds with magnetic actuation because close proximity is necessary to induce enough force and torque; therefore, a better model is needed. Only spherical magnets would not exhibit this problem as Equation (4.1) is known to perfectly model their magnetic fields [108]. For cylindrical magnets, while it is possible to employ finite element methods as used in [126, 34, 33], a more efficient closed form solution is available from Derby and Olbert [31] using the generalized complete elliptic integral:

$$C(k_c, p, c, s) = \int_0^{\pi/2} \frac{c\cos^2\varphi + s\sin^2\varphi}{(\cos^2\varphi + p\sin^2\varphi)\sqrt{\cos^2\varphi + k_c^2\sin^2\varphi}} d\varphi \tag{4.37}$$

which can be numerically solved in an efficient manner by using Bulirsch's algorithm [31]. For an electromagnetic coil with length $2b$, radius a, turns per unit length n and current I, the magnetic field components in cylindrical coordinates (ρ, φ, z) are:

$$b_\rho = B_o\left[\alpha_+ C(k_+, 1, 1, -1) - \alpha_- C(k_-, 1, 1, -1)\right] \tag{4.38}$$

$$b_\varphi = 0 \tag{4.39}$$

$$b_z = \frac{B_o a}{a+\rho}\left[\beta_+ C(k_+, \eta^2, 1, \eta) - \beta_- C(k_-, \eta^2, 1, \eta)\right] \tag{4.40}$$

where

$$B_o = \frac{\mu_0}{\pi} nI, \tag{4.41}$$

$$z_\pm = z \pm b, \tag{4.42}$$

$$\alpha_\pm = \frac{a}{\sqrt{z_\pm^2 + (\rho + a)^2}}, \tag{4.43}$$

$$\beta_\pm = \frac{z_\pm}{\sqrt{z_\pm^2 + (\rho + a)^2}}, \tag{4.44}$$

$$\eta = \frac{a - \rho}{a + \rho}, \tag{4.45}$$

$$k_\pm = \sqrt{\frac{z_\pm^2 + (a - \rho)^2}{z_\pm^2 + (a + \rho)^2}} \tag{4.46}$$

For a permanent magnet with the same dimensions, the magnetic remanence B_r is equivalent to $\mu_0 nI$, thus Equation (4.41) becomes

$$B_o = \frac{B_r}{\pi} \tag{4.47}$$

It is worth mentioning that in order to use this model at our desired update rate of 100 Hz, it was necessary to generate a look-up table that maps positions to magnetic field vectors. Without a look-up table, the update rate was reduced to 65 Hz using an Intel i7@3.60 GHz CPU.

4.3.2.3 Final Pose Estimate:

The final pose estimate can be inferred from the posterior distribution, $p(\mathbf{x}_k|\mathbf{z}_{1:k})$, represented by the particles. The maximum *a posteriori* (MAP) estimate, defined as:

$$\mathbf{x}_k^{\text{MAP}} = \arg\max_{\mathbf{x}_k} p(\mathbf{x}_k|\mathbf{z}_{1:k}) \tag{4.48}$$

is known to be a good estimate of the true state, especially in pose estimation applications where the posterior can be multimodal [125]. One way to obtain the MAP estimate is to take the particle with the largest weight. The resultant estimate using this approach, however, can be very jittery. Therefore, we use the robust mean, $\bar{\mathbf{x}}_k^{\text{MAP}}$, which is the weighted sum of particles inside a ball centered on the particle with the largest weight, $\mathbf{x}_{k,\text{max\_weight}}$:

$$\bar{\mathbf{x}}_k^{\text{MAP}} \approx \frac{\sum_i^N d(\mathbf{x}_k^i) w_k^i \mathbf{x}_k^i}{\sum_i^N d(\mathbf{x}_k^i) w_k^i} \tag{4.49}$$

where N is the number of particles. The function $d : \mathbb{R}^3 \times \mathbb{S}^1 \to \mathbb{R}$ is given by

$$d(\mathbf{x}_k^i) = \begin{cases} 1 & \text{if } \|W_x(\mathbf{x}_{k,\text{max\_weight}} - \mathbf{x}_k^i)\| < \eta \\ 0 & \text{otherwise} \end{cases} \tag{4.50}$$

where W_x is a diagonal weight matrix and η is the desired radius of the ball. In our experiments, we set $W_x = \text{diag}(1, 1, 1, 0)$ and $\eta = 0.1$.

When computing summations on $\gamma \in \mathbb{S}^1$, we use the mean of circular quantities as the simple arithmetic mean is not suitable. This operation is given by:

$$\bar{\gamma} = \text{atan2}\left(\frac{\sum_i^N d(\mathbf{x}_k^i) w_k^i \sin(\gamma^i)}{\sum_i^N d(\mathbf{x}_k^i) w_k^i}, \frac{\sum_i^N d(\mathbf{x}_k^i) w_k^i \cos(\gamma^i)}{\sum_i^N d(\mathbf{x}_k^i) w_k^i} \right) \tag{4.51}$$

The reconstructed pose estimate is finally given by:

$$T_s^w(\bar{\mathbf{x}}_k^{MAP}) = \begin{bmatrix} & & x_x \\ & R_z(\gamma)\tilde{R}_s^w & x_y \\ & & x_z \\ \mathbf{0} & & 1 \end{bmatrix} \tag{4.52}$$

4.3.2.4 Initialization:

Since our objective is to avoid accurate initialization, the particles are initialized by drawing from a uniform distribution within the bounds of a predefined workspace. Correspondingly, no initialization of the pose is required. The particle filter quickly converges solving for the position and the yaw offset. However, at least for initialization, the workspace should be set such that only one solution is available. This is accomplished by constraining the workspace to be contained in a single hemisphere of either the EPM or the electromagnetic coil. This constraint is necessary for all pose estimation techniques that use magnets with symmetrical magnetic fields.

4.4 System and Software Environment

4.4.1 Overview of the System

A general overview of the experimental setup is shown in Figure 4.8. At the end-effector of the 6 DOF robot manipulator, a Neodymium-Iron-Boron (NdFeB) cylindrical permanent magnet (N52 grade, 101.6 mm diameter and length, ND_N-10195, Magnetworld AG, Germany) with axial magnetization and 1.48 T remanence is held by means of a 3D printed box. An additional 3D printed structure holds the electromagnetic coil, which is built using 24 AWG wire with 160 turns arranged in two overlapping layers. Its diameter and height are, respectively, 180 mm and 40 mm. A second robot manipulator (RV6SDL, Mitsubishi, Inc., Japan) holds the capsule for precise ground truth measurements. The two robots are registered by least squares fitting a set of jointly measured 3D points [7].

The capsule remains as described in Chapter 2 and contains two sets of three Hall effect magnetic field sensors and a single IMU. Once assembled, a bias measurement of the magnetic fields is performed away from an external source of magnetic field. The biases are saved and are removed from sensor measurements during the operation of

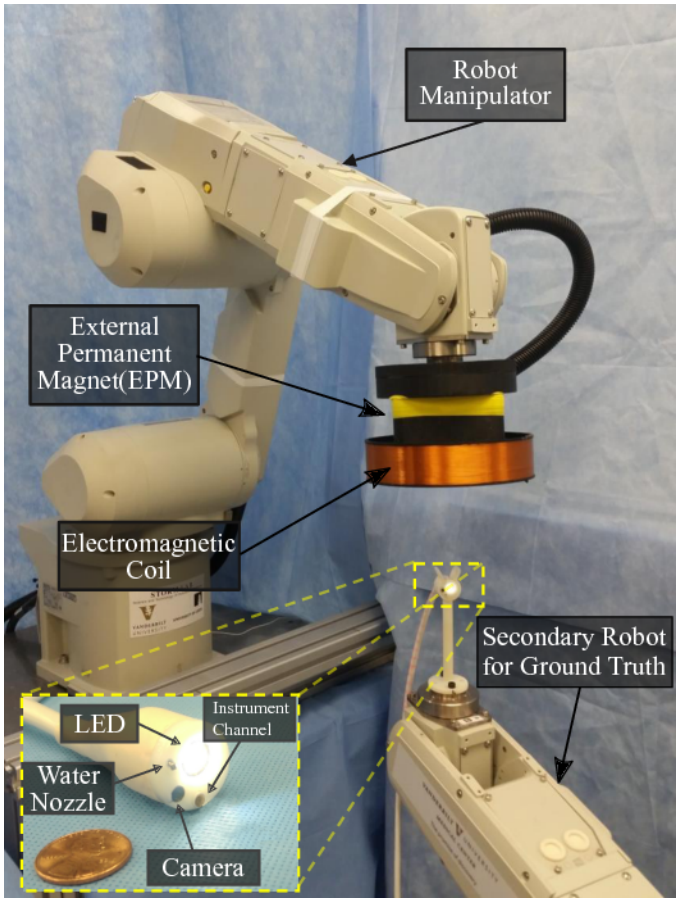

Figure 4.8: Experimental setup of the Magnetically Actuated Capsule (MAC).

the pose estimation algorithm. The generation of the input signal for the coil and the processing of data are achieved through a custom built circuit system that consists of the STM Nucleo development board (STM32F411RET, ARM Cortex M4) and a driver circuit, which are described more in detail in the following section.

4.4.2 Time-varying Magnetic Field

The electromagnetic coil, used to generate a time-varying magnetic field, is designed to satisfy two main constraints. First, it has to be small enough so as to not collide with the environment or the patient during a clinical procedure. Second, it needs to be able to generate a magnetic field strong enough to be detected by our

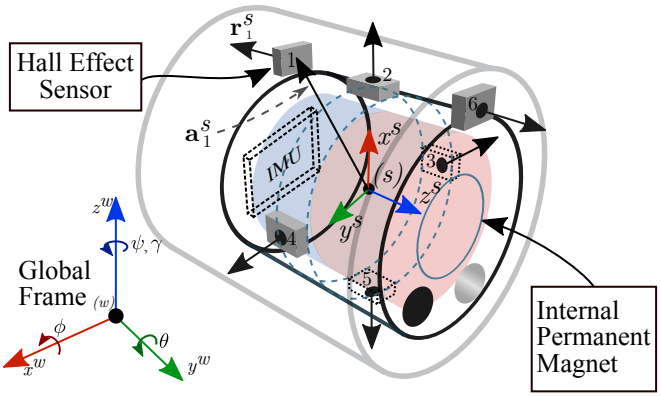

Figure 4.9: The six Hall effect magnetic field sensors and the IMU found inside the capsule. $\mathbf{m}_i^s$ is relative position vector of each Hall effect sensor from the center of the capsule and $\mathbf{r}_i^s$ is each Hall effect sensor's normal vector, which corresponds its the sensing direction.

sensors within the desired workspace. The design parameters were current, coil radius, number of wire turns, and number of wire layers. In order to determine the optimal values for the parameters, nonlinear optimization was performed using MATLAB (Mathworks, USA) where the volume of the coil was the minimization objective. In order to ensure adequate signal-to-noise ratio in the desired workspace, a larger workspace of 300 mm was used in the optimization. The minimum magnetic field strength that can be measured by the Hall effect sensors at the boundary of this workspace was constrained to be above the noise floor of the sensors (10 µT).

The mechanical enclosure for the coil was designed to slide along the outer edges of the EPM in order to achieve the smallest volume for the whole assembly while minimizing the risk for collision with the other links of the robot. This implies that the coil and the EPM may not be centered at the same location; thus, the position of the coil with respect to the EPM was a parameter in our algorithm. For our experiments, the center of the coil was 45 mm away from the center of the EPM along the x-axis of the EPM. It is worth mentioning, however, that varying this distance did not have a noticeable impact on the performance of the pose estimation system.

The time-varying signal was generated by the electromagnetic coil using an off-the-shelf H-bridge in combination with pulse width modulation (PWM) signals from the Nucleo development board. The resistance of the coil was measured to be 7 Ω and its theoretical inductance was calculated to be 6.2 mH. A bench-top power supply was connected to the H-bridge with a set voltage of 17.3 V resulting in an average current of 0.71 A for a total power of 12.3 W. The particular time-varying signal used was a square wave at a frequency of 300 Hz. This frequency was chosen because it allows for a sufficient number of wavelengths to be sampled within the sampling window of 10 ms. It is also low enough that no absorption of the magnetic field occurs as it passes through the human body [132]. Furthermore, due to the high coercivity of NdFeB, from which the EPM is made, the effect of the relatively weak magnetic field generated by the coil on the EPM is negligible. Conversely, since the permeability of the EPM is very close to that of vacuum, the EPM does not act as a flux concentration device, such as soft iron. Thus, the magnetic field generated by the coil is not significantly affected by the presence of the EPM.

4.4.3 Signal Processing

The Nucleo development board was used to acquire data from the capsule's internal sensors. The IMU was sampled at a rate of 100 Hz, while the Hall effect sensors were sampled at a rate of 18 kHz via a 16-bit analog-to-digital converter (AD7689, Analog Devices, USA) inside the capsule. By default, a Hall effect sensor measures the superposition of all static and time-varying signals at a point in space. In order to separately measure the strengths of the magnetic fields generated by the EPM and the coil, signal processing techniques were used. First, by using a sampling time window that was an integer multiple of the period of the time-varying signal, we ensured that the signal's mean was zero. The EPM measurement was then obtained by simply averaging the raw sensor readings. To recover the amplitude of the time-varying

signal, we used Goertzel's algorithm [48, 163], an efficient filter commonly used for tone detection. Two instances of the algorithm were run with 10 ms and 30 ms time windows respectively. The output from 10 ms instance was less reliable due to its relatively large bandwidth, but it provided the desired update rate for real-time pose estimation. The 30 ms instance contained enough samples to apply data windowing functions (*e.g.* Blackman) making its bandwidth much narrower [52]. The particle filter described in Section 4.3 used the outputs of both instances, but assigned a lower weight to the 10 ms instance and only used it while the output from the 30 ms instance was pending.

It is worth mentioning that our scheme of sampling the sensors inside the capsule utilizes the serial peripheral interface (SPI) between the sensors and the microcontroller on the Nucleo board. To adapt our signal acquisition to wireless devices, it would be necessary to embed the microcontroller inside the capsule and only send the processed data wirelessly. This is because a wireless transceiver would be the most power intensive component in a wireless device that contains the same set of magnetic and inertial sensors as our capsule. Reducing the sampling rate of the magnetic field sensors would further conserve energy, however, doing so would negatively affect the tone detection algorithm by increasing its bandwidth. As a result, the overall system would be more susceptible to noise.

Examples of wireless devices that use a similar set of sensors can be found in the literature. The capsule in [32] contained the Allegro A1391 Hall effect sensors as well as the STMicroelectronics LIS331DLH accelerometer and used the Texas Instrument C2530 System-On-Chip microcontroller for data processing and wireless communication. The resulting capsule had a length of 60 mm and diameter of 18 mm which is approximately 2.3 times times the size of commercially available capsule endoscopes. Similarly, [117] used the Allegro A1392 Hall effect sensors and the CC2530 in their

capsule. The resulting capsule had a length of 42 mm and diameter of 13.5 mm which is approximately 1.4 times the size of commercially available capsule endoscopes [117].

4.4.4 Parallel Particle Filter Implementation

Our implementation of the particle filter makes use of the SMCTC C++ library [67]. Modifications to the library were made to enable parallel computation where possible using the OpenMP API [104]. In particular, the update phase of the algorithm, where the likelihoods $p(\mathbf{z}_k|\mathbf{x}_k^i)$ are computed, benefited from parallelization as the calculations for each particle are independent and computationally intensive. With these modifications, we were able to use 10000 particles on 4 cores of an Intel i7@3.60 GHz CPU with an average update rate of 100 Hz.

4.4.5 Calibration

Several parameters of the system need to be calibrated to get good accuracy. We start by calibrating the IMU where the capsule is inserted in a 3D printed fixture so that accelerometer data can be collected in all principal directions. The primary purpose of this calibration is to account for the misalignment between the capsule frame and the IMU frame caused during assembly. We followed the formulations described in [146]:

$$\tilde{\mathbf{a}}_i = A_m \begin{bmatrix} \frac{1}{s_x} & 0 & 0 \\ 0 & \frac{1}{s_y} & 0 \\ 0 & 0 & \frac{1}{s_z} \end{bmatrix} (\mathbf{a} - \mathbf{a}_{\text{off}}) \tag{4.53}$$

where $\tilde{\mathbf{a}}_i$ are normalized accelerometer outputs for known orientations i; $\mathbf{a}$ are raw measurements; A_m is the misalignment rotation matrix between the capsule and the IMU; s_x, s_y, and s_z are scaling factors; and $\mathbf{a}_{\text{off}}$ is the zero-g offset. Equation (4.53)

can be rewritten in a manner suitable for least-squares computation:

$$\begin{aligned}\tilde{\mathbf{a}}_i^\top &= \bar{\mathbf{a}}_i A_c \\ &= \begin{bmatrix} a_{x_i} & a_{y_i} & a_{z_i} & 1 \end{bmatrix} A_c\end{aligned} \tag{4.54}$$

where $A_c \in \mathbb{R}^{4\times 3}$ forms the parameters to be calibrated and $\bar{\mathbf{a}}_i = [\mathbf{a}_i^\top \quad 1]$ is the augmented row vector formed from $\mathbf{a}_i$, the ith raw measurements.

Six known orientations corresponding to the faces of the calibration fixture are used to collect samples $\tilde{\mathbf{a}}_i, i = 1, 2, ..., 6$. Let $Y = [\tilde{\mathbf{a}}_1 \quad \tilde{\mathbf{a}}_2 \quad \tilde{\mathbf{a}}_3 \quad \tilde{\mathbf{a}}_4 \quad \tilde{\mathbf{a}}_5 \quad \tilde{\mathbf{a}}_6]^\top$ be the matrix of these known outputs, and similarly define $W = [\bar{\mathbf{a}}_1^\top \quad \bar{\mathbf{a}}_2^\top \quad \bar{\mathbf{a}}_3^\top \quad \bar{\mathbf{a}}_4^\top \quad \bar{\mathbf{a}}_5^\top \quad \bar{\mathbf{a}}_6^\top]^\top$ be to the matrix of augmented raw measurements $\bar{\mathbf{a}}_i$, then we can write:

$$Y = WA_c \tag{4.55}$$

the solution of which is given by

$$A_c = \left(W^\top W\right)^{-1} W^\top Y \tag{4.56}$$

During the operation of the pose estimation algorithm, raw accelerometer measurements are multiplied by A_c before they are used in the complementary filter [93] to estimate the capsule's orientation with an unknown yaw offset.

Calibration of the magnetic field sensors is accomplished in two steps. In the initial step, the zero-offset magnetic field readings are obtained. These measurements are done with the capsule located far away from any external magnetic field sources so that only the magnetic field of the internal permanent magnet (IPM) are recorded. The second step is a comprehensive procedure that is used to calibrate for the scaling of magnetic field sensors, misalignment of the magnetic field sensors, the dimensions of the coil, the strength of the coil, and the position of the coil relative to the EPM.

To collect the necessary data for this step, the robot is used to move the EPM and coil in a grid pattern (*e.g.* $3 \times 3 \times 3$ grid spanning $0.15\,\mathrm{m} \times 0.15\,\mathrm{m} \times 0.15\,\mathrm{m}$) near the capsule while the capsule is held stationary. The pose of the EPM and readings from the magnetic field sensors are collected for a period of time at each grid point resulting in N samples.

To solve for the unknown parameters, we solve a nonlinear minimization problem. Our optimization variable $\mathbf{x}$ is given by

$$\mathbf{x} = \begin{bmatrix} \boldsymbol{\theta} \\ \boldsymbol{\phi} \\ \boldsymbol{\xi} \\ \boldsymbol{\Gamma} \\ \mathbf{p}_{\boldsymbol{\varsigma}} \\ \mathbf{o}_{\boldsymbol{\varsigma}} \end{bmatrix} \tag{4.57}$$

where $\boldsymbol{\theta} \in \mathbb{S}^6$ and $\boldsymbol{\phi} \in \mathbb{S}^6$ are alignment rotations in the x and y axis respectively;[1] $\xi \in \mathbb{R}^6$ is the scaling factor for the magnetic field sensors; $\Gamma \in \mathbb{R}^3$ is comprised of the height and radius of the coil and its translation with respect to the EPM; and $\mathbf{p}_{\boldsymbol{\varsigma}}$ and $\mathbf{o}_{\boldsymbol{\varsigma}}$ are the position and orientation (in Euler angles) of the capsule respectively. Reusing some of our earlier notation, we denote $\mathbf{z}_i \in \mathbb{R}^{12}$ as the ith measured sample comprised of magnetic field readings from the EPM and the coil, and $\mathbf{z}_i^*(\mathbf{x})$ as the calculated magnetic field. $\mathbf{z}_i^*(\mathbf{x})$ is based on Equations (4.32) and (4.33) and is a function of our optimization variable. The minimization problem can then be written as

$$\begin{aligned} \underset{\mathbf{x}}{\text{minimize}} \quad & \sum_{i=1}^{N} (\mathbf{z}_i - \mathbf{z}_i^*(\mathbf{x}))^\top W_z (\mathbf{z}_i - \mathbf{z}_i^*(\mathbf{x})) \\ \text{subject to} \quad & \mathbf{g}(x) \leq 0 \end{aligned} \tag{4.58}$$

[1] We assume the normal of the magnetic field sensor is along z axis, and thus, rotations about this axis do not affect the sensor's readings.

Once again, $W_z \in \mathbb{R}^{12\times12}$ is a diagonal weight matrix used to normalize the three orders of magnitude difference in the sensor outputs for the EPM and the coil. The constraint function $\mathbf{g(x)}$ is used to enforce bounds on $\mathbf{x}$. As the optimization problem can have many local minima, having bounds that limit x to reasonable values is advisable. For example, by starting the motion of the robot such that the EPM and coil assembly is directly above the capsule, we can set narrow bounds for $\mathbf{p_\varsigma}$.

We have used Scipy's *minimize* function with the SLSQP option to solve the optimization problem. A plot from the resulting calibration is shown in Figure 4.10. In this plot, the nominal selection of values for x is compared with the results from our calibration. Significant improvements are observed in matching the measured data with calibrated parameters.

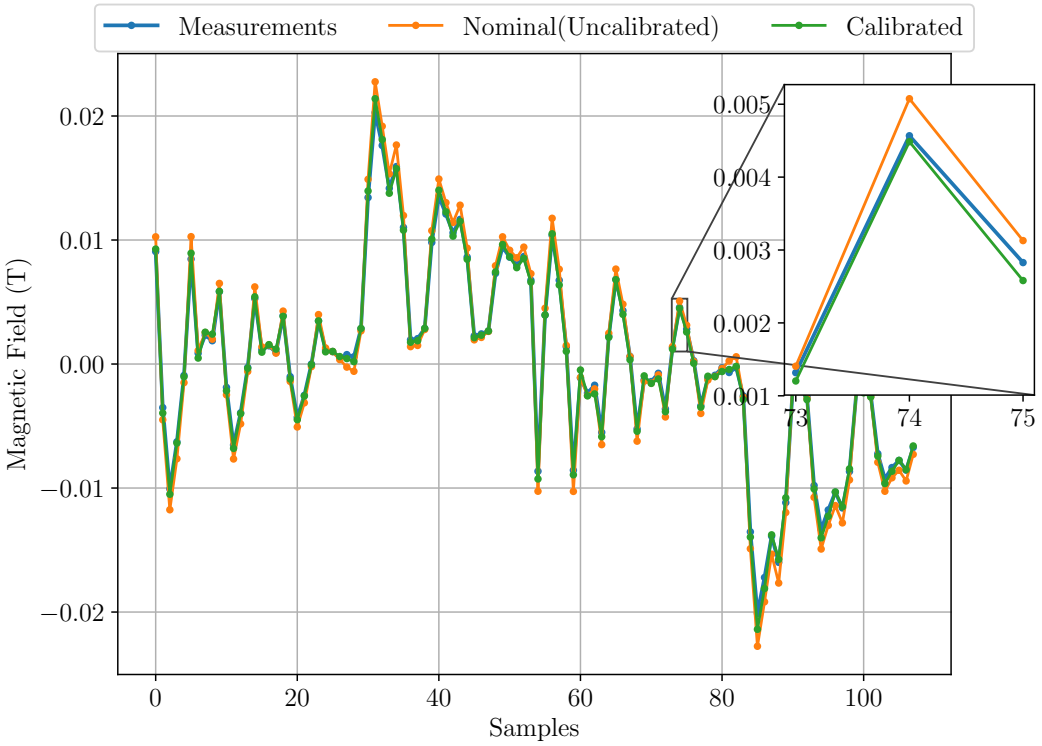

Figure 4.10: Comparison between nominal and calibrated parameters. Significant improvements are observed in matching the measured data with calibrated parameters.

4.5 Experimental Validation and Results

In light of the criteria of success mentioned in Section 3.4.1, the pose estimation algorithm was experimentally validated in static and dynamic conditions. In the static condition tests, both the capsule and the EPM were fixed in known poses making it possible to compute average errors at each position including positions in the singular regions of the EPM and the coil. The dynamic test involved moving the capsule and/or the EPM at fixed speeds to characterize trajectory errors.

4.5.1 Validation in Static Conditions

As shown in Figure 4.8, the capsule was inserted into a 3D printed enclosure and secured to the secondary robot manipulator that was positioned in a known pose relative to the first robot. In the first set of static tests, the EPM was moved in a spiral trajectory along the surface of a hemisphere maintaining a constant distance from the capsule (see Figure 4.11). Six tests were performed with varying radii of the hemisphere ranging from 150 mm to 200 mm. The maximum radius was limited to 200 mm in order to constrain the test to regions of clinically relevant forces and torques induced on the capsule.

4.5.1.1 Spiral Trajectory

A spiral trajectory was chosen to assess whether the accuracy of the system degraded with increasing distance. For each test, the EPM was stopped at 25 points along the trajectory and pose estimates were recorded for 30 seconds each. The pose estimation algorithm was restarted at each point to assess its ability to determine the yaw offset error. Pose errors were computed by taking the mean of the collected pose estimates and comparing them against the ground truth. Orientation errors are given

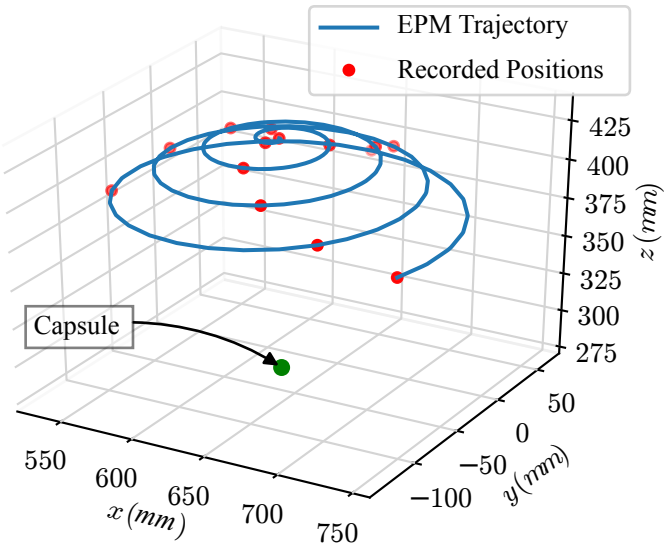

Figure 4.11: Spiral trajectory used in static validation experiments. The red dots indicate the positions where the EPM was stopped and 25 points were collected.

Table 4.1: Average accuracy (mean ± std) of position estimates for static tests along a spiral trajectory

Radius of hemisphere (mm)	Δx (mm)	Δy (mm)	Δz (mm)	$\Delta\phi$ (°)	$\Delta\theta$ (°)	$\Delta\psi$ (°)
150	1.04 ± 1.42	3.67 ± 1.63	2.87 ± 1.05	0.93 ± 0.67	-0.95 ± 1.03	-4.73 ± 0.31
160	1.39 ± 1.42	3.81 ± 1.62	2.65 ± 1.00	1.00 ± 0.62	-1.05 ± 0.88	-5.06 ± 0.25
170	1.42 ± 1.39	3.97 ± 1.66	2.41 ± 0.92	1.00 ± 0.61	-1.09 ± 0.67	-5.62 ± 0.16
180	1.71 ± 1.42	4.19 ± 1.69	2.15 ± 0.94	1.02 ± 0.59	-0.86 ± 0.57	-5.62 ± 0.14
190	1.87 ± 1.40	4.32 ± 1.72	1.80 ± 0.91	1.05 ± 0.54	-0.84 ± 0.43	-5.65 ± 0.11
200	1.97 ± 1.38	4.35 ± 1.71	1.55 ± 0.88	1.11 ± 0.50	-0.84 ± 0.33	-5.66 ± 0.09

in ZYX Euler angles, roll(ϕ), pitch(θ), and yaw(ψ), where the resultant rotation is:

$$R_s^w = R_{\mathbf{z}}(\psi)R_{\mathbf{y}}(\theta)R_{\mathbf{x}}(\phi) \tag{4.59}$$

and the yaw(ψ) angle corresponds to the unknown yaw angle error γ, from Section 4.3.

Table 4.1 shows the overall accuracy of the system using the mean and standard deviations of the errors. In general, accuracy is expected to degrade with increasing distance as the magnetic field strengths weaken and become more susceptible to noise. The negligible differences in the standard deviations of the errors in Table 4.1,

however, show that due to our high sampling rate, signal processing of the magnetic field measurements, and fusing of multiple sources of magnetic fields, this degradation was not observed. Yet, a larger position error was incurred in the y axis, which may be due to the fact that the capsule was in the singularity region of the EPM for a subset of the 25 points on the hemisphere reducing the number of constraining equations mapping poses to magnetic field vectors. Since the singularity plane of the EPM for these set of trials was the yz-plane, larger errors on the y axis can be expected. Additionally, the orientation error in ψ was larger than the other orientation angles since it was the only angle affected by the bias and noise characteristics of the magnetic field sources, while the other two angles were obtained from accelerometer measurements.

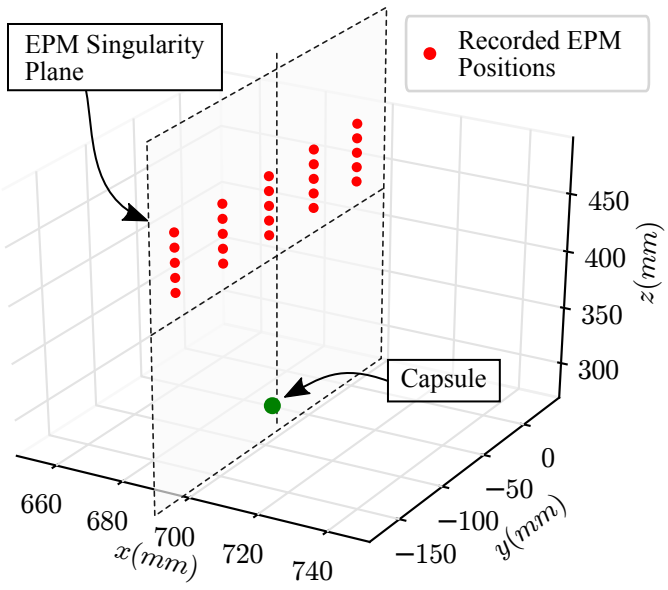

Figure 4.12: Configuration for testing the singular regions of the EPM. With the capsule fixed in space, the EPM was placed on a grid of coplanar points. The EPM was oriented such that the capsule was always in its singularity plane.

4.5.1.2 Evaluation in the Region of Singularity

The second set of static tests evaluated the performance of the system in the singularity region of the EPM. As shown in Figure 4.12, the capsule was fixed in

a single pose inside the EPM's singularity region. The EPM was then placed on a grid of points defined by the plane of singularity. A total of 25 grid points spanning 200 mm × 50 mm were used where pose estimates were recorded for 30 seconds each. The average position and orientation errors were:

$$\begin{aligned} \Delta x &= \ 2.85 \pm 0.80\,\text{mm} & \Delta\phi &= \ 0.73 \pm 0.60^\circ \\ \Delta y &= \ 3.74 \pm 1.53\,\text{mm} & \Delta\theta &= -1.69 \pm 0.15^\circ \\ \Delta z &= \ 1.67 \pm 0.88\,\text{mm} & \Delta\psi &= \ 3.76 \pm 0.12^\circ \end{aligned}$$

To ensure the absence of singularity regions, the capsule was also placed on the line defined by the intersection of the singularity planes of the EPM and the coil. A total of 10 equally spaced points were used to record pose estimates for 30 seconds each. The average position and orientation errors were:

$$\begin{aligned} \Delta x &= \ 1.21 \pm 0.18\,\text{mm} & \Delta\phi &= \ 0.75 \pm 0.10^\circ \\ \Delta y &= \ 4.85 \pm 1.34\,\text{mm} & \Delta\theta &= -2.05 \pm 0.13^\circ \\ \Delta z &= \ 5.10 \pm 0.68\,\text{mm} & \Delta\psi &= \ 1.08 \pm 0.06^\circ \end{aligned}$$

The results show that the system performs well even in the singular regions of either magnet.

The overall accuracy of the system for these set of tests was equivalent or better than the systems described in [34] and [33] without requiring an initialization step. For comparison, the errors reported by the authors are given in Table 4.2. Given the results, we can conclude that our pose estimation algorithm readily satisfies the accuracy criteria.

4.5.1.3 Comparison with Prior Pose Estimation Methods

To provide a concrete example of the effect of magnetic singularity regions and demonstrate the scale of the singularity problem on previous 6 DOF pose estimation methods, we applied the algorithm described in [34] to the data collected in the

Table 4.2: Average accuracy (mean ± std) of previous methods

Method	Δx(mm)	Δy(mm)	Δz(mm)	$\Delta\phi$(°)	$\Delta\theta$(°)	$\Delta\psi$(°)
[127]	-3.2 ± 18.0	5.4 ± 15.0	-13 ± 19			
[34]	-3.40 ± 3.20	-3.80 ± 6.20	3.40 ± 7.30	-6 ± 18	3 ± 20	-19 ± 50
	Δr(mm)	$\Delta\theta'$(°)	Δz(mm)	$\Delta\phi$(°)	$\Delta\theta$(°)	$\Delta\psi$(°)
[33]	6.2 ± 4.4	5.4 ± 7.9	6.9 ± 3.9	3.4 ± 3.2	3.7 ± 3.5	3.6 ± 2.6

150 mm static spiral trajectory experiment. As the authors conclude in [33], the long term performance of their iterative algorithm is susceptible to drift without periodic updates from their absolute pose estimation algorithm [34]. The ill-conditioning of

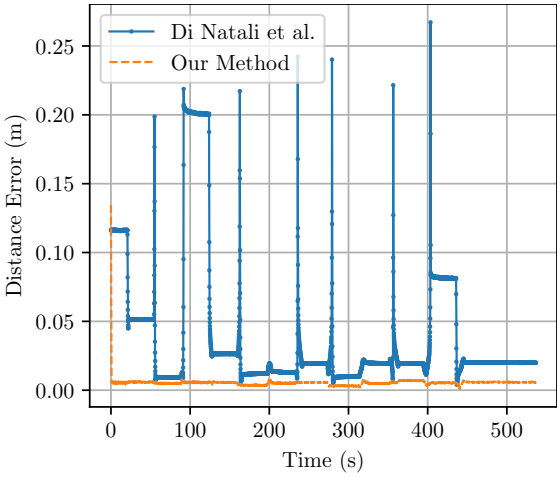

(a) Comparison between the pose estimation algorithms in [34] and our algorithm. Severe performance degradation occurs in [34] when the capsule is in the singularity region of the EPM.

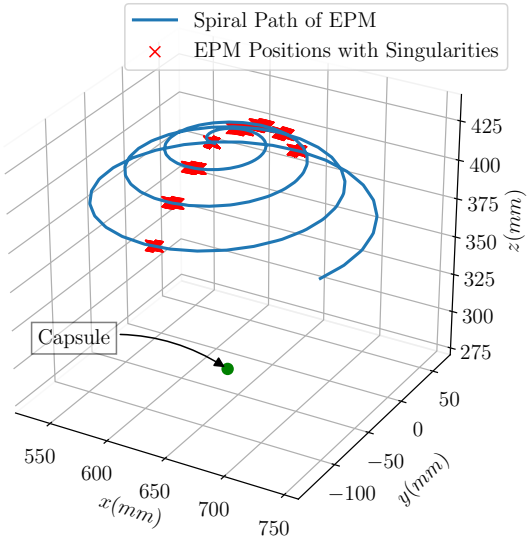

(b) Positions of the EPM where severe performance degradation occurs in [34] when the capsule is in the singularity region of the EPM.

the Jacobian in regions of singularity (Section 4.2.1) combined with the drift problem leads us to expect the performance of the iterative algorithm to be worse than their noniterative algorithm in [34]. Consequently, only a comparison between [34] and our novel approach is given here. Figure 4.13a shows the distance error of the two methods during the spiral trajectory experiment. Severe performance degradation occurs in [34] when the capsule is in or near the singularity region of the EPM. Large

spikes can also be observed as the EPM moves along the spiral to one of the 25 test points (see Figure 4.13b) and, in so doing, its singularity region crosses the position of the capsule. In contrast, our approach is robust to the presence of singularity regions.

4.5.1.4 Effect of EPM Orientation

In order to explore the effect of the EPM's orientation on the pose estimation algorithm, an additional static experiment was conducted. The EPM was moved to 10 points on a planar grid of 100 mm × 100 mm and at each point 10 different orientations were tested (see Figure 4.14). The grid was chosen to be in the xy plane so as to include singular and non-singular regions. The average position and orientation errors were:

$$\Delta x = -2.55 \pm 2.89\,\text{mm} \qquad \Delta\phi = \ \ 1.17 \pm 0.30^\circ$$

$$\Delta y = \ \ 2.60 \pm 4.91\,\text{mm} \qquad \Delta\theta = -1.03 \pm 4.18^\circ$$

$$\Delta z = -7.21 \pm 1.84\,\text{mm} \qquad \Delta\psi = \ \ 3.06 \pm 0.65^\circ$$

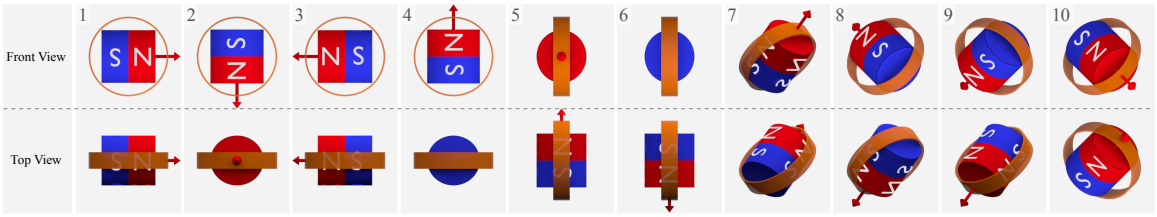

Figure 4.14: The ten orientations of the EPM and coil assembly that were tested in our experiment.

As can be seen from these values, the orientation of the EPM does not have a marked effect on the accuracy of the pose estimation algorithm.

4.5.2 Validation in dynamic conditions

Two types of experiments were conducted for validation under dynamic conditions. The *static-dynamic* experiment consisted of moving only the capsule along a trajectory while the EPM was static. In the *dynamic-dynamic* experiment, both the

capsule and the EPM moved along a trajectory keeping a constant relative speed. In both cases, the trajectory was designed to mimic the general shape of a human colon [2]. Moreover, in order to have ground truth measurements, a secondary robot manipulator was used to hold and move the capsule along the given trajectory. Errors were obtained by taking the average of the errors computed at each instance of time between the pose estimate and the ground truth.

4.5.2.1 Static-dynamic Case

The motivation for the first case was to assess whether the particle filter, without an accurate motion model, could track the movement of the capsule. Table 4.3 shows the performance of the system at speeds of 10 mm/s, 25 mm/s and 50 mm/s. The increase in the standard deviation of the position errors is correlated with increase in capsule speed indicating that the system is sensitive to the relative motion of the capsule. However, in most robotic capsule endoscopy applications, the relative motion of the capsule with respect to the EPM is expected to be minimal.

Table 4.3: Average accuracy (mean ± std) of pose estimates for static-dynamic tests

Speed (mm/s)	Δx (mm)	Δy (mm)	Δz (mm)	$\Delta\phi$ (°)	$\Delta\theta$ (°)	$\Delta\psi$ (°)
10	-3.39 ± 6.76	-4.84 ± 5.23	4.06 ± 1.91	-0.96 ± 2.30	0.29 ± 1.73	-0.37 ± 2.84
25	-1.98 ± 7.70	-5.07 ± 5.67	4.49 ± 1.92	-1.75 ± 1.88	0.08 ± 1.55	-0.20 ± 2.79
50	0.70 ± 12.05	-3.33 ± 10.01	4.79 ± 2.74	-3.10 ± 2.14	-1.65 ± 3.44	-0.13 ± 2.69

4.5.2.2 Dynamic-dynamic Case

The latter dynamic condition reflects how the capsule would be used in a real scenario where the capsule is driven by a moving EPM. As such, the trajectory of the EPM was created by offsetting the capsule's trajectory by a distance of 200 mm. Again, speeds of 10 mm/s, 25 mm/s and 50 mm/s were tested, the results of which, are shown in Table 4.4. Unlike the static-dynamic case, the standard deviations in

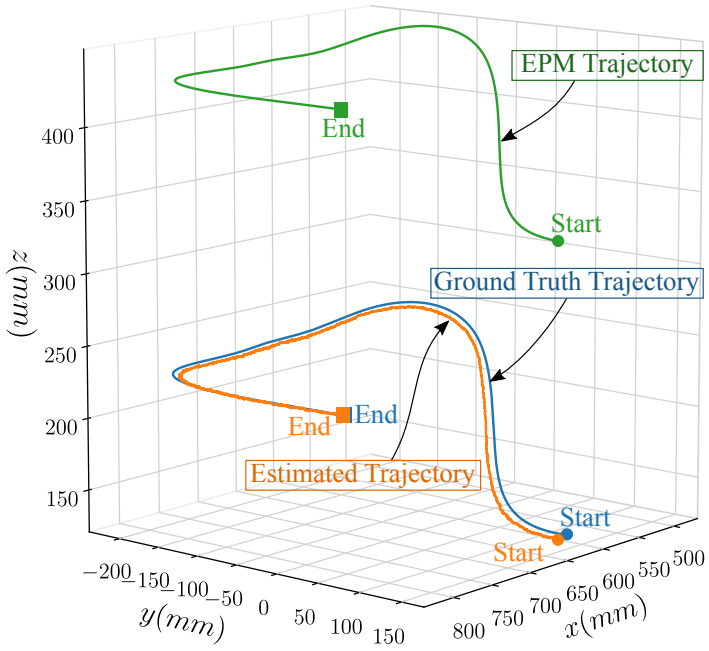

Figure 4.15: Plot of the trajectories of the EPM and the capsule for the 10 m/s dynamic-dynamic test. In order to establish ground truth, a secondary robot manipulator was used to hold and move the capsule at a constant speed along the trajectory. The trajectory was designed to mimic the shape of a human colon.

the position errors are not affected by the speed of the capsule because there was very little relative motion between the EPM and the capsule. Yet, a larger standard deviation is observed than the static test (Table 4.1), which can be attributed to the use of the random walk motion model in the particle filter algorithm. As mentioned in Section 4.3, better performance can be expected in applications with accurate motion models.

Table 4.4: Average accuracy (mean ± std) of pose estimates for dynamic-dynamic tests

Speed (mm/s)	Δx (mm)	Δy (mm)	Δz (mm)	$\Delta\phi$ (°)	$\Delta\theta$ (°)	$\Delta\psi$ (°)
10	-2.05 ± 5.00	-1.60 ± 3.76	1.60 ± 0.57	-1.76 ± 1.15	0.07 ± 1.80	-0.27 ± 2.65
25	-1.39 ± 5.56	-1.50 ± 3.95	1.35 ± 0.65	-2.14 ± 1.45	-0.09 ± 1.96	-0.17 ± 2.60
50	-2.59 ± 5.44	-1.77 ± 5.63	1.16 ± 0.75	-3.01 ± 2.00	-1.44 ± 3.76	-0.08 ± 2.68

It is also evident from a qualitative assessment of Figure 4.15 that the system tracks the capsule's trajectory with a steady bias. Further work is needed to determine

whether this bias exists due to errors in the magnetic field model used or faulty sensor calibrations. Despite this, the errors reported in Table 4.4 are equivalent or better than the errors reported in [127, 34, 33] (see Table 4.2).

4.6 Conclusion

A fundamental problem in magnetic pose estimation is that any source of magnetic field that can be sufficiently modeled by the point-dipole model is susceptible to ambiguities arising from regions of singularity when used as a source of information for pose estimation. This problem is mitigated by using a secondary source of magnetic field with an orthogonal dipole moment as shown in this chapter. The extra information gained from the secondary source of magnetic field has the added benefit of enabling the computation of the initial yaw angle.

In order to use the two sources of information effectively, a particle filtering approach was used. By randomly initializing particles in the workspace, the filter was able to converge to the pose of the capsule, thereby eliminating the need for accurate initialization. Our experimental results show that the random walk motion model is sufficient to accurately track the capsule as long as the relative motion of the capsule with respect to the EPM remains low, as would be the prevalent case for robotic capsule endoscopy applications. However, in clinical application scenarios certain conditions, such as the sudden movement of the patient, could violate the assumption of low relative motion. This necessitates a higher-level system that monitors the sensor readings and the internal state of the pose estimation system and warns the user if the pose estimates cannot be relied upon. We hypothesize that the value of the likelihood function during the measurement update step of our particle filter algorithm can help to make this determination as we have observed the value to be extremely small when the capsule is out of range or it is intentionally moved to a new position rapidly.

In virtually all of our static tests, the average errors were below 5 mm in any single position axis and 6° in any orientation angle. How pose estimation errors affect the forces and torques induced on the capsule and closed-loop control in general needs further study, the result of which would be to establish a more meaningful benchmark. With our parallel implementation of the particle filter, our system was able to achieve an average update rate of 100 Hz. In comparison, the update rates reported in [34] and [33] were 71 Hz and 143 Hz respectively. In terms of workspace, our system exceeded the required radius of 150 mm owing to size of our EPM, the use of multiple sources of magnetic fields, and the higher sampling rate used in our signal acquisition.

CHAPTER 5

Closed-Loop Control for Direct Propulsion Capsules

5.1 Introduction

In the context of magnetically actuated capsule endoscopy, we define closed-loop control as a control strategy in which the magnetic actuator incorporates measurements about the pose of the capsule endoscope (CE) and the wrenches currently applied to it in order to determine the magnetic fields and gradients that move the capsule toward a desired pose. This implies that there is a controller that can alter the magnetic fields and gradients felt by the capsule at any given instance of time. For electromagnet based actuation systems, this is accomplished by varying the currents on multiple coils. Whereas for permanent magnet based systems, this involves changing the pose of the external permanent magnet with the help of an automated mechanism, usually in the form of a robotic manipulator.

The function of closed-loop control is to ensure that the capsule moves according to a given command. In a clinical scenario, this commanded motion is provided by a gastroenterologist who, using some form of user interface, directs the capsule to areas of interest based on a video stream coming from the capsule. This type of control is known as tele-operation as the physician does not directly impart forces or torques on the capsule. The semantics of the term is different from its use in the study by Ciuti et al. [23] where a user interface is used to control an external permanent magnet (EPM) mounted on a robot's end effector. The motion of the EPM in turn was used to manipulate a capsule. In contrast, we define tele-operation as a means of control where the operator does not have to think about how to control the EPM. Instead, the operator's commanded motions are directly applied on the capsule and the motion of the robotic manipulator remains transparent to the operator.

The goal of our contribution is to bring the Magnetically Actuated Capsule (MAC) system closer to clinical realization where the closed-loop algorithms developed will be used to create an effective tele-operation system. Various actuation techniques and control strategies have been explored for CE applications in different parts of the gastrointestinal (GI) tract. The MAC system described in Chapter 2 has been designed specifically for the colon as a direct propulsion system. A survey of the literature has shown that the most relevant related system was presented by Mahoney and Abbott [90]. Their system, however, had a few limitations that prevent it from being used directly in the MAC system. First, their capsule was designed to operate in a liquid filled stomach where no disturbance impeded the capsule's motion and the capsule's magnetic moment (heading) was assumed to always align itself to the direction of the EPM's magnetic field. Such assumptions do not hold in the MAC system because (1) its intended use is in the colon where it is subjected to constant contact with the colon wall, and (2) the soft-tether introduces additional disturbances in the form of friction and stored bending energy. In order to implement closed-loop control for the MAC without these assumptions, their formulations have to be extended to include feedback of the orientation of the capsule.

Another limitation in Mahoney and Abbott's study was the lack of a clinically relevant real-time pose estimation system. In their experiments, a mockup capsule was submerged in a water tank in view of two external cameras pointing in orthogonal directions. Image processing techniques were used to determine the position of the capsule, but its orientation was not computed.

In this chapter, we build on the work of Mahoney and Abbott [90] and demonstrate closed-loop control for the MAC integrated with a clinically viable magnetic pose estimation system.

5.2 Theoretical Approach

Since it is not feasible to levitate the capsule using a single permanent magnet in a cavity that is not filled with liquid, the capsule's position is controlled in 2 degrees of freedom (DOF). This implies that the capsule will always be in contact with a barrier such as the colon wall. Nevertheless, the force applied by the capsule against the barrier can be regulated and this capability can be used to keep this force below a safety threshold. In our formulations and experiments, this barrier is assumed to constrain motion in the vertical direction. In addition, due to the nature of magnetically induced torque, it is not possible to control the rotation of the capsule along its axis of magnetization. Thus, our closed-loop control scheme admits 2 DOF control in position and 2 DOF control in orientation.

As is done in most magnetically actuated closed-loop control systems, we assume that the magnetic field of both the actuator and the magnet inside the capsule can be modelled by the point dipole model. Although this model can be inaccurate for small distances from the actuating magnet, we rely on our pose estimation system, which uses a more accurate magnetic field model, for pose feedback to close the loop on any error introduced by the point dipole model. This assumption allows us to efficiently compute the needed motion of the EPM to control the capsule, which would otherwise be computationally burdensome if we had employed more complicated models. Although the capsule is tethered, our formulations do not explicitly model the effect of tether and its interactions with the environment as our device is not equipped with the necessary shape and force sensors. Instead, we treat it as a disturbance and rely on the closed-loop system to compensate for it.

The dipole moments of the actuating permanent magnet and the capsule's magnet are denoted by $\mathbf{m_E} \in \mathbb{R}^3$ and $\mathbf{m_\varsigma} \in \mathbb{R}^3$ respectively. The actuating magnet is attached to the end effector of a robotic manipulator that can position it in at least 5 DOF. Due to the axial symmetry of a dipole field, rotation of the actuating magnet about

its dipole moment does not change the magnetic field at the capsule. Thus, only 5 DOF is needed, although more DOF could enable the robot to accomplish other tasks while performing the primary task of magnetic manipulation. The position of the actuating magnet and the capsule's magnet are denoted by $\mathbf{p}_{\mathbf{E}} \in \mathbb{R}^3$ and $\mathbf{p}_{\boldsymbol{\varsigma}} \in \mathbb{R}^3$ respectively.

With the dipole assumption, given a magnetic field $\mathbf{B}_{\mathbf{E}}$ generated by the EPM, the force $\mathbf{f}$ and torque $\boldsymbol{\tau}$ on the magnet inside the capsule is given by:

$$\mathbf{f} = (\mathbf{m}_{\boldsymbol{\varsigma}} \cdot \nabla)\mathbf{B}_{\mathbf{E}} \tag{5.1}$$

$$\boldsymbol{\tau} = \mathbf{m}_{\boldsymbol{\varsigma}} \times \mathbf{B}_{\mathbf{E}} \tag{5.2}$$

As such, the magnetic force $\mathbf{f}_{\mathbf{m}}$ and torque $\boldsymbol{\tau}_{\mathbf{m}}$ on the capsule are:

$$\mathbf{f}_{\mathbf{m}}(\mathbf{p}, \hat{\mathbf{m}}_{\mathbf{E}}, \hat{\mathbf{m}}_{\boldsymbol{\varsigma}}) = \frac{3\mu_0 \left\|\mathbf{m}_{\mathbf{E}}\right\| \left\|\mathbf{m}_{\boldsymbol{\varsigma}}\right\|}{4\pi \left\|\mathbf{p}\right\|^4}(\hat{\mathbf{m}}_{\mathbf{E}}\hat{\mathbf{m}}_{\boldsymbol{\varsigma}}{}^{\top} + \hat{\mathbf{m}}_{\boldsymbol{\varsigma}}\hat{\mathbf{m}}_{\mathbf{E}}{}^{\top} + (\hat{\mathbf{m}}_{\boldsymbol{\varsigma}}{}^{\top} Z \hat{\mathbf{m}}_{\mathbf{E}})I)\hat{\mathbf{p}} \tag{5.3}$$

$$\boldsymbol{\tau}_{\mathbf{m}}(\mathbf{p}, \hat{\mathbf{m}}_{\mathbf{E}}, \hat{\mathbf{m}}_{\boldsymbol{\varsigma}}) = \frac{\mu_0 \left\|\mathbf{m}_{\mathbf{E}}\right\| \left\|\mathbf{m}_{\boldsymbol{\varsigma}}\right\|}{4\pi \left\|\mathbf{p}\right\|^3}\hat{\mathbf{m}}_{\boldsymbol{\varsigma}} \times D(\hat{\mathbf{p}})\hat{\mathbf{m}}_{\mathbf{E}} \tag{5.4}$$

where $\mathbf{p} = \mathbf{p}_{\boldsymbol{\varsigma}} - \mathbf{p}_{\mathbf{E}}$, $I \in \mathbb{R}^{3\times3}$ is the identity matrix, $D = 3\hat{\mathbf{p}}\hat{\mathbf{p}}^{\top} - I$, and $Z = I - 5\hat{\mathbf{p}}\hat{\mathbf{p}}^{\top}$.

The robot manipulator is controlled in joint position mode and its generalized coordinates are given by $\mathbf{q} \in \mathbb{R}^n$, where n is the number of joints. The robot's geometric Jacobian $J_{\mathcal{R}}(\mathbf{q}) \in \mathbb{R}^{6\times n}$ is used to linearize the relationship between generalized joint velocities and the end effector twist as follows:

$$\begin{bmatrix} \dot{\mathbf{p}}_{\mathbf{E}} \\ \boldsymbol{\omega}_{\mathbf{E}} \end{bmatrix} = J_{\mathcal{R}}(\mathbf{q})\dot{\mathbf{q}} \tag{5.5}$$

We note that any component of $\boldsymbol{\omega}_{\mathbf{E}}$ that rotates the actuating magnet along the axis of the dipole moment $\hat{\mathbf{m}}_{\mathbf{E}}$ does not change $\hat{\mathbf{m}}_{\mathbf{E}}$. That is, $\dot{\hat{\mathbf{m}}}_{\mathbf{E}} = \boldsymbol{\omega}_{\mathbf{E}} \times \hat{\mathbf{m}}_{\mathbf{E}}$. To incorporate

this into the mathematical formulation we define the EPM's Jacobian $J_{\mathbf{E}}(q)$ as

$$\begin{bmatrix} \dot{\mathbf{p}}_{\mathbf{E}} \\ \dot{\hat{\mathbf{m}}}_{\mathbf{E}} \end{bmatrix} = \begin{bmatrix} I & 0 \\ 0 & S(\hat{\mathbf{m}}_{\mathbf{E}})^{\top} \end{bmatrix} J_R \dot{\mathbf{q}} = J_{\mathbf{E}} \dot{\mathbf{q}} \tag{5.6}$$

where $S(\mathbf{a}) \in \mathfrak{so}(3)$ denotes the skew-symmetric form of the cross product operation.

Furthermore, we assume that the system is in a quasi-static equilibrium meaning that at a given instance of time, the magnetic forces on the capsule are counter balanced by gravity and other forces from the environment (*e.g.* tether resistance, reaction force from colon wall). With this assumption, we can solve for the necessary pose of the EPM that imparts a desired force and torque on the capsule using the nonlinear equations Equation (5.3) and Equation (5.4) by linearizing them with respect to their parameters as follows

$$\begin{aligned} \begin{bmatrix} \dot{\mathbf{f}} \\ \dot{\boldsymbol{\tau}} \end{bmatrix} &= \begin{bmatrix} \frac{\partial \mathbf{f_m}}{\partial \mathbf{p}} & \frac{\partial \mathbf{f_m}}{\partial \hat{\mathbf{m}}_{\mathbf{E}}} & \frac{\partial \mathbf{f_m}}{\partial \hat{\mathbf{m}}_{\boldsymbol{\varsigma}}} \\ \frac{\partial \boldsymbol{\tau}_{\mathbf{m}}}{\partial \mathbf{p}} & \frac{\partial \boldsymbol{\tau}_{\mathbf{m}}}{\partial \hat{\mathbf{m}}_{\mathbf{E}}} & \frac{\partial \boldsymbol{\tau}_{\mathbf{m}}}{\partial \hat{\mathbf{m}}_{\boldsymbol{\varsigma}}} \end{bmatrix} \begin{bmatrix} \dot{\mathbf{p}} \\ \dot{\hat{\mathbf{m}}}_{\mathbf{E}} \\ \dot{\hat{\mathbf{m}}}_{\boldsymbol{\varsigma}} \end{bmatrix} \\ &= J_{\mathcal{F}}(\mathbf{p}, \hat{\mathbf{m}}_{\mathbf{E}}, \hat{\mathbf{m}}_{\boldsymbol{\varsigma}}) \begin{bmatrix} \dot{\mathbf{p}} \\ \dot{\hat{\mathbf{m}}}_{\mathbf{E}} \\ \dot{\hat{\mathbf{m}}}_{\boldsymbol{\varsigma}} \end{bmatrix} \end{aligned} \tag{5.7}$$

The components of the matrix $J_{\mathcal{F}}(\mathbf{p}, \hat{\mathbf{m}}_{\mathbf{E}}, \hat{\mathbf{m}}_{\boldsymbol{\varsigma}})$ are given in Appendix B. Since $\mathbf{p} = \mathbf{p}_{\boldsymbol{\varsigma}} - \mathbf{p}_{\mathbf{E}}$, we separate the contribution of the capsule's velocity on the change in wrench from that of the EPM's velocity. Using $J_{\mathcal{F}}$ to designate $J_{\mathcal{F}}(\mathbf{p}, \hat{\mathbf{m}}_{\mathbf{E}}, \hat{\mathbf{m}}_{\boldsymbol{\varsigma}})$:

$$\begin{bmatrix} \dot{\mathbf{f}} \\ \dot{\boldsymbol{\tau}} \end{bmatrix} = J_{\mathcal{F}} \left(\begin{bmatrix} \dot{\mathbf{p}}_{\varsigma} \\ 0 \\ \dot{\hat{\mathbf{m}}}_{\boldsymbol{\varsigma}} \end{bmatrix} + \begin{bmatrix} -\dot{\mathbf{p}}_{\mathbf{E}} \\ \dot{\hat{\mathbf{m}}}_{\mathbf{E}} \\ 0 \end{bmatrix} \right) \tag{5.8}$$

$$\begin{bmatrix} \dot{\mathbf{f}} \\ \dot{\boldsymbol{\tau}} \end{bmatrix} = J_{\mathcal{F}} \left(\begin{bmatrix} \dot{\mathbf{p}}_{\varsigma} \\ 0 \\ \dot{\hat{\mathbf{m}}}_{\boldsymbol{\varsigma}} \end{bmatrix} + \begin{bmatrix} -I & 0 & 0 \\ 0 & I & 0 \\ 0 & 0 & 0 \end{bmatrix} \begin{bmatrix} J_{\mathbf{E}} \\ 0 \end{bmatrix} \dot{\mathbf{q}} \right) \tag{5.9}$$

Due to the fast dynamics of the system compared to our robot manipulator and the friction in our environment, the motion of the capsule is characterized by stick-slip motion. Thus, for practical purposes, we can neglect the contributions of $\dot{\mathbf{p}}_{\varsigma}$ and $\dot{\hat{\mathbf{m}}}_{\boldsymbol{\varsigma}}$ to the changes in force and torque. Therefore Equation (5.9) becomes:

$$\begin{bmatrix} \dot{\mathbf{f}} \\ \dot{\boldsymbol{\tau}} \end{bmatrix} = J_{\mathcal{F}} \begin{bmatrix} -I & 0 & 0 \\ 0 & I & 0 \\ 0 & 0 & 0 \end{bmatrix} \begin{bmatrix} J_{\mathbf{E}} \\ 0 \end{bmatrix} \dot{\mathbf{q}} \tag{5.10}$$

Defining $J_{\mathcal{F}_{\mathbf{E}}}$ as

$$J_{\mathcal{F}_{\mathbf{E}}} = J_{\mathcal{F}} \begin{bmatrix} -I & 0 & 0 \\ 0 & I & 0 \\ 0 & 0 & 0 \end{bmatrix} \begin{bmatrix} J_{\mathbf{E}} \\ 0 \end{bmatrix} \tag{5.11}$$

and noting that, when discretized, Equation (5.10) relates small changes in joint angles $\boldsymbol{\delta}\mathbf{q}$ to changes in force $\boldsymbol{\delta}\mathbf{f}$ and torque $\boldsymbol{\delta}\boldsymbol{\tau}$ on the capsule, Equation (5.9) can then be rearranged and succinctly written as

$$\begin{bmatrix} \boldsymbol{\delta}\mathbf{f} \\ \boldsymbol{\delta}\boldsymbol{\tau} \end{bmatrix} = J_{\mathcal{F}_{\mathbf{E}}} \boldsymbol{\delta}\mathbf{q} \tag{5.12}$$

The solution to $\boldsymbol{\delta}\mathbf{q}$ are determined by inverting the Jacobian matrix $J_{\mathcal{F}_{\mathbf{E}}}$, which will have a null space since we assume the robot has at least 5 DOF and the magnetic task space is 4 DOF as described earlier. This redundancy in the Jacobian matrix can be utilized to choose solutions that perform the given tasks while avoiding joint

limits or preferring certain robot configurations. This technique will be described in Section 5.2.3

Once $\boldsymbol{\delta}\mathbf{q}$ is determined, it can be sent directly to the robot, if the robot has a joint velocity interface. However, if the robot has a joint position interface, as in the case of our platform, $\boldsymbol{\delta}\mathbf{q}$ is integrated in time to calculate the next joint position vector $\mathbf{q}$, which is then sent to the robot.

The values of $\boldsymbol{\delta}\mathbf{f}$ and $\boldsymbol{\delta}\boldsymbol{\tau}$ can be chosen according to the desired task. Two possible schemes are described in Sections 5.2.1 and 5.2.2. These schemes were developed during the course of the dissertation with the overarching goal of achieving tele-operation for the MAC platform. Thus additional improvements were made in the latter scheme besides the choice of position vs. velocity as the source of error.

5.2.1 Closed-Loop Position Control

In position control, $\boldsymbol{\delta}\mathbf{f}$ and $\boldsymbol{\delta}\boldsymbol{\tau}$ are chosen to minimize the position and orientation errors between the current pose of the capsule and a desired pose:

$$\begin{bmatrix} \boldsymbol{\delta}\mathbf{f} \\ \boldsymbol{\delta}\boldsymbol{\tau} \end{bmatrix} = \begin{bmatrix} K_{p_e}\mathbf{e}_p + \mathbf{f}_{grav} \\ K_{p_o}\mathbf{e}_o \end{bmatrix} \tag{5.13}$$

The position error is given by $\mathbf{e}_p = \mathbf{p}_{\varsigma_d} - \mathbf{p}_{\varsigma}$ with z-component set to zero and where $\mathbf{p}_{\varsigma_d}$ is the desired position of the capsule. The z-component of $\boldsymbol{\delta}\mathbf{f}$ is set to a value so as to keep the capsule from falling. As such, $\mathbf{f}_{grav} = [0 \quad 0 \quad K_{p_g}(f_{z_d} - f_{z_c})]^T$ where f_{z_d} is the desired vertical magnetic force (determined empirically based on the weight of the capsule), and f_{z_c} is the current vertical force. The orientation error is obtained by computing the angle between the heading axis of the capsule and the desired heading: $\mathbf{e}_o = \hat{\mathbf{h}}_{\boldsymbol{\varsigma}} \times \hat{\mathbf{h}}_{\boldsymbol{\varsigma_d}}$ where $\hat{\mathbf{h}}_{\boldsymbol{\varsigma}}$ and $\hat{\mathbf{h}}_{\boldsymbol{\varsigma_d}}$ are the capsule's current and desired headings, respectively. Note that any component of $\hat{\mathbf{h}}_{\boldsymbol{\varsigma_d}}$ in the direction of $\hat{\mathbf{h}}_{\boldsymbol{\varsigma}}$ will be nulled by the cross product making it explicit that this DOF cannot

be controlled. The proportional gains K_{p_e}, K_{p_o} and K_{p_g} are tuned experimentally balancing the trade-offs between manipulation speed and linearization accuracy. That is, the linear relationship formed by the Jacobian $J_{\mathcal{F}_\mathbf{E}}$ in Equation (5.12) is only valid if the commanded $\boldsymbol{\delta}\mathbf{f}$ and $\boldsymbol{\delta}\boldsymbol{\tau}$ remain small.

The limitation of this scheme is that the position error $\mathbf{e}_p$ decreases exponentially as $\mathbf{p}_\varsigma$ approaches $\mathbf{p}_{\varsigma_d}$. As a result, given a path of way points, the capsule unnecessarily slows down to a stop at each way point. As this is not conducive for tele-operation, an alternative scheme for choosing $\boldsymbol{\delta}\mathbf{f}$ and $\boldsymbol{\delta}\boldsymbol{\tau}$ was pursued.

5.2.2 Closed-Loop Hybrid Position and Velocity Control

Despite the unavoidable stick–slip characteristics of magnetic manipulation in air, smoother motion can be achieved by decoupling forward velocity error from lateral position errors and providing two separate proportional-integral (PI) controllers that close the loop on the corresponding errors. Given a desired path, the forward velocity controller attempts to propel the capsule forward (tangent to the path) at a constant velocity while the position controller ensures that the lateral (normal to the path) position error of the capsule from the desired path remains small.

In the following expressions, we denote the directions of the tangent and normal vectors at the point on the path that is closest to the center of the capsule by $\hat{\mathbf{t}}$ and $\hat{\mathbf{n}}$ respectively. These vectors are shown in Figure 5.1.

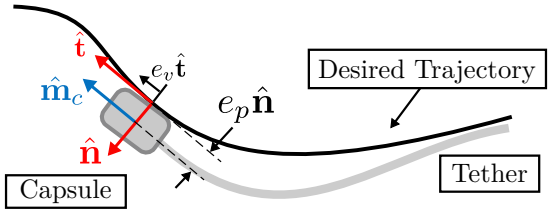

Figure 5.1: Illustration of the tangent ($\hat{\mathbf{t}}$) and normal ($\hat{\mathbf{n}}$) vectors.

The velocity error, $\mathbf{e}_v$, is defined as the error between the current average velocity, $\dot{\mathbf{p}}_\boldsymbol{\varsigma}$, and the desired velocity, $\dot{\mathbf{p}}_{\boldsymbol{\varsigma_d}}$. Using the position estimates output by our pose

estimation algorithm, the average velocity of the capsule is computed by applying a low pass filter to differences in position in consecutive time steps. Thus, $\mathbf{e}_v = \dot{\mathbf{p}}_{\boldsymbol{\varsigma_d}} - \dot{\mathbf{p}}_{\boldsymbol{\varsigma}}$. We remove any component of the velocity error in the lateral direction by projecting it onto the tangent direction, $\hat{\mathbf{t}}$, of the path. The tangent velocity error, $(\mathbf{e}_v \cdot \hat{\mathbf{t}})\hat{\mathbf{t}}$, is used as the error term in a proportional controller. The tangent projection of the velocity error, $\mathbf{e}_v \cdot \hat{\mathbf{t}}$, is also used to form a feed forward term f_r, that estimates and compensates for the resistance force applied by the tether.

$$f_r = -K_{i_{vel}} \int \mathbf{e}_v \cdot \hat{\mathbf{t}} \tag{5.14}$$

f_r is assumed to always be in the negative direction of the path as it represents the resistance forces from the tether behind the capsule.

The position error is given by $\mathbf{e}_p = \mathbf{p}_{\boldsymbol{\varsigma_d}} - \mathbf{p}_{\boldsymbol{\varsigma}}$. The projection of this error into the normal direction, $(\mathbf{e}_p \cdot \hat{\mathbf{n}})\hat{\mathbf{n}}$, is used as the error term in a PI controller. Finally, the orientation error is computed as $\mathbf{e}_o = \hat{\mathbf{h}}_{\boldsymbol{\varsigma}} \times \hat{\mathbf{h}}_{\boldsymbol{\varsigma_d}}$ as is done for the closed-loop position control scheme.

Using the matrices $P_{\hat{\mathbf{t}}} = \hat{\mathbf{t}}\hat{\mathbf{t}}^\top$ and $P_{\hat{\mathbf{n}}} = I - \hat{\mathbf{t}}\hat{\mathbf{t}}^\top$ to project error vectors onto $\hat{\mathbf{t}}$ and $\hat{\mathbf{n}}$ respectively, the overall expression for our control input, which is the vector of desired wrench on the capsule, is given by:

$$\begin{bmatrix} \mathbf{u}_f \\ \mathbf{u}_\tau \end{bmatrix} = \begin{bmatrix} K_{p_{vel}} P_{\hat{\mathbf{t}}} \mathbf{e}_v + K_{p_{pos}} P_{\hat{\mathbf{n}}} \mathbf{e}_p + K_{i_{pos}} \int P_{\hat{\mathbf{n}}} \mathbf{e}_p \\ K_{p_o} \mathbf{e}_o + K_{i_o} \int \mathbf{e}_o \end{bmatrix} \tag{5.15}$$

The final changes in wrench on the capsule are computed by subtracting estimates of the wrench currently applied on the capsule:

$$\begin{bmatrix} \delta\mathbf{f} \\ \delta\boldsymbol{\tau} \end{bmatrix} = \begin{bmatrix} \mathbf{u}_f - (\mathbf{f}_\mathbf{m} + \mathbf{f}_r) \\ \mathbf{u}_\tau - \boldsymbol{\tau}_\mathbf{m} \end{bmatrix} \tag{5.16}$$

Subtracting the estimated current wrenches allows us to control the gain of the integral terms explicitly whereas in the position control scheme in Section 5.2.1 the integration occured implicitly as the controller integrated the resulting $\boldsymbol{\delta}\mathbf{q}$s.

5.2.3 Redundancy Resolution

We use two types of redundancy resolution techniques to choose a single $\boldsymbol{\delta}\mathbf{q}$ from an infinity of possible solutions to Equation (5.12). Infinite solutions exist because (1) there are more DOF in the robot manipulator than needed by the task of manipulating the EPM, and (2) certain motions of the EPM, such as rotation about its dipole moment, do not change the wrench induced on the capsule.

5.2.3.1 Weighted Damped Least-Squares Optimization

Equation (5.12) can be cast as a weighted damped least-squares (WDLS) optimization problem [128, 19]:

$$\min_{\boldsymbol{\delta}\mathbf{q}} \left(\left\| W_x \left(\boldsymbol{\delta}\mathbf{x} - J_{\mathcal{F}_\mathbf{E}} \boldsymbol{\delta}\mathbf{q} \right) \right\|^2 + \alpha^2 \left\| W_q^{-1} \boldsymbol{\delta}\mathbf{q} \right\|^2 \right) \tag{5.17}$$

where

$$\boldsymbol{\delta}\mathbf{x} = \begin{bmatrix} \boldsymbol{\delta}\mathbf{f} \\ \boldsymbol{\delta}\boldsymbol{\tau} \end{bmatrix}, \tag{5.18}$$

$W_x \in \mathbb{R}^{6\times 6}$ and $W_q \in \mathbb{R}^{n\times n}$ are symmetric and positive definite weighting matrices and α is a user-defined damping parameter. W_x can be used to set the weight of the errors between the commanded and resulting $\boldsymbol{\delta}\mathbf{x}$ [128]. This is useful, for example, for permitting more error in the vertical direction as it is not critical for horizontal motion as long as it is within safety limits. Furthermore, owing to the capsule being tangentially aligned with its tether at the point of where the capsule is attached to the tether, motion along this direction results in the least interference from the tether.

If the capsule were to travel in a direction that is not aligned with its heading, the tether would induce a higher disturbance as a result of the additional bending torque. To avoid this, we wish to prioritize capsule heading over position/velocity control resulting in heading being generally aligned with the capsule's direction of motion. This prioritization is implemented by increasing weights (favoring motion) in W_x that correspond to the torque components of the $\boldsymbol{\delta}\mathbf{x}$.

The WDLS approach can also be used to avoid joint limits by setting W_q to inhibit the motion of joints near their limits. To accomplish this, we first define a function $h(\mathbf{q}) : \mathbb{R}^n \rightarrow \mathbb{R}$ that maps joint values to a value that approaches infinity as the joints approach their limits [19].

$$h\left(\mathbf{q}\right) = \sum_{i=1}^{n} \frac{1}{4} \frac{\left(q_{i,max} - q_{i,min}\right)^2}{\left(q_{i,max} - q_i\right)\left(q_i - q_{i,min}\right)} \tag{5.19}$$

we then define the diagonal elements w_i of $W_{\mathbf{q}}$ as

$$w_i = 1 + \left| \frac{\partial h(\mathbf{q})}{\partial q_i} \right| \tag{5.20}$$

where the gradient is defined as

$$\frac{\partial h(\mathbf{q})}{\partial q_i} = \frac{1}{4} \frac{\left(q_{i,max} - q_{i,min}\right)^2 \left(2q_i - q_{i,max} - q_{i,min}\right)}{\left(q_{i,max} - q_i\right)^2 \left(q_i - q_{i,min}\right)^2} \tag{5.21}$$

The gradient $\frac{\partial h(\mathbf{q})}{\partial q_i}$ is equal to zero when the ith joint is at the midpoint of its range and infinity when the joint approaches either of its bounds. Correspondingly, w_i is equal to 1 when the ith joint is at the midpoint and infinity when the joint approaches its bounds. When this weighting matrix is used in Equation (5.17) and a joint is near its limit, the objective function approaches infinity preventing any more motion of the joint thus ensuring that joint limits are never violated. However, since this formulation in its current form only stops motion of the joint without favoring joint

motions that move away from the joint limit, a better formulation is given by [19]

$$w_i = \left\{ \begin{array}{ll} 1 + \left| \frac{\partial h(\mathbf{q})}{\partial q_i} \right| & \text{if } \Delta \left| \frac{\partial h(\mathbf{q})}{\partial q_i} \right| \geq 0 \\ 1 & \text{if } \Delta \left| \frac{\partial h(\mathbf{q})}{\partial q_i} \right| < 0 \end{array} \right\} \tag{5.22}$$

This formulation allows motion in a joint if the direction of motion takes the joint away from its joint limit.

The last component of the WDLS optimization problem given in Equation (5.17) is the damping term controlled by α, a small positive number. This damping is used to avoid kinematic singularities of the robot which occur when the manipulator Jacobian $J_{\mathcal{R}}$ loses rank. Without a scheme to avoid kinematic singularities, such as the damping used in our formulation, the robot's joint velocities can approach infinity when the robot is in certain configurations—an undesirable and dangerous phenomenon. Since manipulator singularities can indeed occur during magnetic guidance, this component is essential for successful practical use.

A closed form solution to Equation (5.17) is given by $\boldsymbol{\delta}\mathbf{q} = J^{+}\boldsymbol{\delta}\mathbf{x}$ where J^{+} is the WDLS inverse of the Jacobian defined as

$$\begin{aligned} J^{+} &= J_W^{\top}(J_W J_W^{\top} + \alpha I)^{-1} \\ J_W &= W_x J_{\mathcal{F}_{\mathbf{E}}} W_q \end{aligned} \tag{5.23}$$

As can be seen from Equation (5.23), the parameter α adds a small perturbation to the matrix $J_W J_W^{\top}$ so that its inverse can be computed even when it is singular. The downside of this approach is that this perturbation is always present introducing errors in the system even in non-singular robot configuration. While it is possible to set α to zero when the robot in these situations, practical use has shown that the small errors introduced do not affect the magnetic guidance system significantly.

5.2.3.2 Gradient Projection

Gradient projection is a redundancy resolution technique that exploits the homogeneous solutions of a system of equations to accomplish a secondary task [84]. In our case, the homogeneous solutions of Equation (5.17) are those solutions that move the joints of the robot while making no impact on the resulting $\boldsymbol{\delta}\mathbf{x}$. Such solutions can be found by utilizing the null space projection matrix of the Jacobian in Equation (5.23) defined as $(I - J^{+}J)$. The overall solution can be written as

$$\boldsymbol{\delta}\mathbf{q} = J^{+}\boldsymbol{\delta}\mathbf{x} + (I - J^{+}J)\beta\boldsymbol{\eta} \tag{5.24}$$

where $\boldsymbol{\eta}$ is an arbitrary vector and β is a user-defined scaling parameter [19].

Liegeois [84] showed that an objective function $g(\mathbf{q})$ can be locally minimized using the following solution:

$$\boldsymbol{\delta}\mathbf{q} = J^{+}\boldsymbol{\delta}\mathbf{x} + (I - J^{+}J)\beta\,\nabla g(\mathbf{q}) \tag{5.25}$$

where $\beta < 0$. Note that, unlike WDLS, gradient projection can cause the robot to move even when no motion is commanded in task space.

The choice of the vector $g(\mathbf{q})$ depends on the desired secondary task. In our application, the secondary tasks can be used to add certain heuristics into the closed-loop controller. These heuristics help move the robot toward configurations more suitable for magnetic manipulation. Here we give two such heuristic functions.

The first heuristic expresses a preference for an elbow-up configuration of the 5th and 6th links of the robot, which is a desirable configuration during colonoscopy, as shown in Figure 5.2. The objective function $g(\mathbf{q})$ is chosen to be the joint norm squared function of the error between a desired nominal joint configuration, $\mathbf{q}_{des}$ and

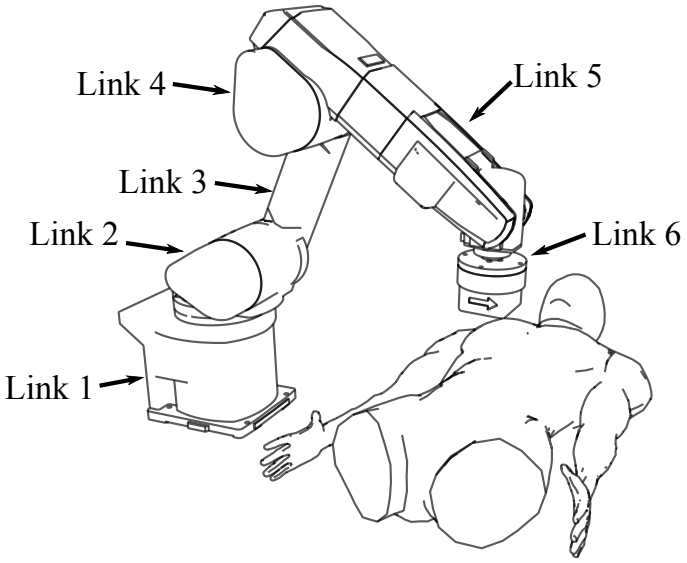

Figure 5.2: Intended robot-patient positioning for tethered capsule colonoscopy. Links 5 and 6 are desired to maintain elbow-up configuration.

the current joint values $\mathbf{q}$:

$$g(\mathbf{q}) = \frac{1}{2}(\mathbf{q}_{des} - \mathbf{q})^{\top} W_g (\mathbf{q}_{des} - \mathbf{q}) \tag{5.26}$$

whose gradient, $\nabla g \in \mathbb{R}^{n \times 1}$, is defined as

$$\nabla g = -W_g (\mathbf{q}_{des} - \mathbf{q}) \tag{5.27}$$

where $W_g \in \mathbb{R}^{n \times n}$ is a weight matrix used to prioritize which joints must satisfy the objective function (*e.g.* the weight associated with joint 0 should be zero as it has no bearing on the robot having a elbow-up configuration). The limitation of this approach is that the $\mathbf{q}_{des}$ and W_g have to be determined experimentally and may change depending on the orientation of the patient.

The second heuristic expresses a preference for having the bottom surface of the magnet holder be parallel to the patient. We call this the flatness heuristic. As this heuristic involves the motion of the EPM as opposed to the joints of the robot, there

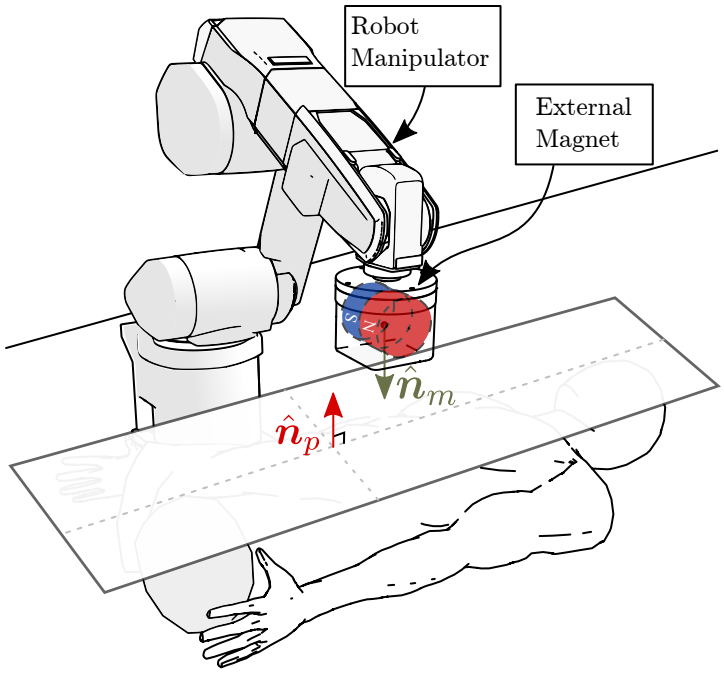

Figure 5.3: Illustration of the normal vector $\hat{\mathbf{n}}_p$ of the patient surface and the normal vector $\hat{\mathbf{n}}_m(\mathbf{q})$ of the magnet holder.

is only 1 DOF redundancy—rotation about the EPM's axis of magnetization. The objective function $g(\mathbf{q})$ is determined by the cosine of the angle between the normal vector $\hat{\mathbf{n}}_p$ of the patient surface and the normal vector $\hat{\mathbf{n}}_m(\mathbf{q})$ of the magnet holder (see Figure 5.3):

$$g(\mathbf{q}) = \hat{\mathbf{n}}_p^\top \hat{\mathbf{n}}_m(\mathbf{q}) \tag{5.28}$$

but the normal vector $\hat{\mathbf{n}}_m(\mathbf{q})$ can be written in terms of the forward kinematics of the robot

$$\hat{\mathbf{n}}_m(\mathbf{q}) = R^0_{\mathbf{E}}(\mathbf{q})\hat{\mathbf{n}}^{\mathbf{E}}_m \tag{5.29}$$

$$g(\mathbf{q}) = \hat{\mathbf{n}}_p^\top R^0_{\mathbf{E}}(\mathbf{q})\hat{\mathbf{n}}^{\mathbf{E}}_m \tag{5.30}$$

where $R^0_{\mathbf{E}}(\mathbf{q}) \in \mathbb{SO}(3)$ is the rotation of the EPM frame with respect to the base frame, (0), of the robot and $\hat{\mathbf{n}}^{\mathbf{E}}_m$ is normal vector expressed in the EPM frame. Note that $\hat{\mathbf{n}}^{\mathbf{E}}_m$ is constant vector set by the user in a similar manner as $\hat{\mathbf{n}}_p$. Taking the

gradient of $g(\mathbf{q})$ involves taking the partial derivative $\frac{\partial R^0_{\mathbf{E}}}{\partial \mathbf{q}}(\mathbf{q})$, which is problematic since $R^0_{\mathbf{E}}$ is a matrix. To resolve this, we take an approach similar to the one used by Murray et al. [100] in writing the Jacobian in terms of twists.

We start by noting that the time derivative of our objective can be written as

$$\begin{aligned}
\dot{g} = \frac{\partial g}{\partial \mathbf{q}}\dot{\mathbf{q}} &= \hat{\mathbf{n}}_p^\top \dot{R}^0_{\mathbf{E}} \hat{\mathbf{n}}^{\mathbf{E}}_m \\
&= \hat{\mathbf{n}}_p^\top \left(\sum_{i=1}^{n} \frac{\partial R^0_{\mathbf{E}}}{\partial q_i} \dot{q}_i \right) \hat{\mathbf{n}}^{\mathbf{E}}_m \\
&= \sum_{i=1}^{n} \left(\hat{\mathbf{n}}_p^\top \frac{\partial R^0_{\mathbf{E}}}{\partial q_i} \hat{\mathbf{n}}^{\mathbf{E}}_m \right) \dot{q}_i
\end{aligned} \tag{5.31}$$

The term in the parenthesis in Equation (5.31) can be further simplified by recognizing that $\frac{\partial R^0_{\mathbf{E}}}{\partial q_i} {R^0_{\mathbf{E}}}^\top \in \mathfrak{so}(3)$ is skew-symmetric. Let $S(\boldsymbol{\omega}_i) = \frac{\partial R^0_{\mathbf{E}}}{\partial q_i} {R^0_{\mathbf{E}}}^\top$. We know that the vector $\boldsymbol{\omega}_i$ forms the bottom three rows of the ith column of the manipulator Jacobian J_R. Thus:

$$\begin{aligned}
\sum_{i=1}^{n} \left(\hat{\mathbf{n}}_p^\top \frac{\partial R^0_{\mathbf{E}}}{\partial q_i} {R^0_{\mathbf{E}}}^\top R^0_{\mathbf{E}} \hat{\mathbf{n}}^{\mathbf{E}}_m \right) \dot{q}_i &= \sum_{i=1}^{n} \left(\hat{\mathbf{n}}_p^\top S(\boldsymbol{\omega_i}) R^0_{\mathbf{E}} \hat{\mathbf{n}}^{\mathbf{E}}_m \right) \dot{q}_i \\
&= \sum_{i=1}^{n} \left[\hat{\mathbf{n}}_p^\top \left(\boldsymbol{\omega_i} \times R^0_{\mathbf{E}} \hat{\mathbf{n}}^{\mathbf{E}}_m \right) \right] \dot{q}_i \\
&= \sum_{i=1}^{n} \left[\left(R^0_{\mathbf{E}} \hat{\mathbf{n}}^{\mathbf{E}}_m \times \hat{\mathbf{n}}_p \right)^\top \boldsymbol{\omega_i} \right] \dot{q}_i \\
&= \left(R^0_{\mathbf{E}} \hat{\mathbf{n}}^{\mathbf{E}}_m \times \hat{\mathbf{n}}_p \right)^\top \sum_{i=1}^{n} \boldsymbol{\omega_i} \dot{q}_i \\
&= \left(R^0_{\mathbf{E}} \hat{\mathbf{n}}^{\mathbf{E}}_m \times \hat{\mathbf{n}}_p \right)^\top \tilde{J}_R \dot{\mathbf{q}}
\end{aligned}$$

where $\tilde{J}_R \in \mathbb{R}^{3\times n}$ is the matrix formed by taking the bottom three rows of J_R. The gradient ∇g is then given by

$$\nabla g = \left(\frac{\partial g}{\partial \mathbf{q}} \right)^\top = \tilde{J}_R^\top \left(R^0_{\mathbf{E}} \hat{\mathbf{n}}^{\mathbf{E}}_m \times \hat{\mathbf{n}}_p \right) \tag{5.32}$$

For proof-of-concept algorithm validation, we have utilized a dynamic simulation environment. This simulation is made in Gazebo; an open-source simulation environment with a physics engine. The simulation environment functions in conjunction with the Robot Operating System (ROS) [120] which allowed for seamlessly switching between running our software in simulation and on the real system. This enabled us to iterate and develop our algorithms faster in simulation before running them on the real system. As seen in Figure 5.4, the simulation includes the robot, capsule

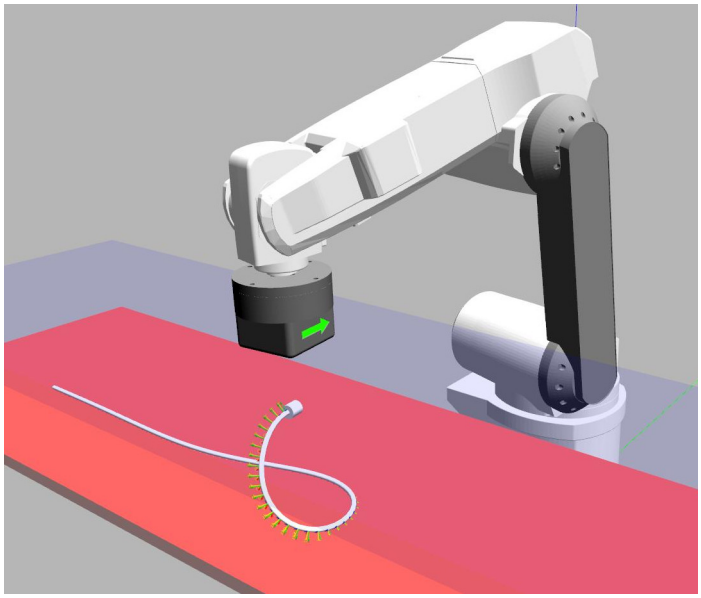

Figure 5.4: Gazebo simulation environment with built-in physics engine. A custom plug-in allows for simulation of magnetic interaction between the EPM and capsule.

with tether, a floor, and a vertical barrier. Simulation of physical phenomena such as gravity, inertia and friction (*e.g.* friction between capsule and vertical barrier) are natively supported by Gazebo. However, there is no native support for the soft body properties of the tether. As such, the tether's continuum configuration is modeled with the use of a finite number of rigid cylindrical links connected by universal joints. As shown in Figure 5.5, the two joint axes of the universal joint are orthogonal to the tangent of the tether.

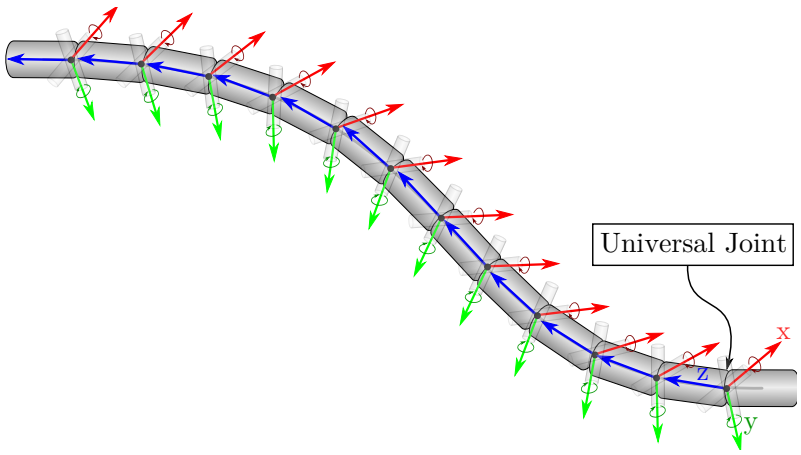

Figure 5.5: The soft tether is simulated in Gazebo by a chain of links connected by universal joints.

Both the tether's bending and torsional stiffness characteristics were simulated by tuning the error reduction parameter (ERP) and constraint force mixing (CFM) parameters of Gazebo. Internally, Open Dynamics Engine (ODE) [141], the physics engine used by Gazebo, solves linear complementarity problems (LCPs) to determine contact forces and enforce position and velocity constraints. As an added benefit, the specific formulation used by ODE enables users to create an equivalent spring-damper system by mapping the ERP and CFM parameters to stiffness k_p and damping k_d properties of the spring-damper system [55]:

$$\begin{aligned} \text{ERP} &= \frac{k_p \Delta t}{k_p \Delta t + k_d} \\ \text{CFM} &= \frac{1}{k_p \Delta t + k_d} \end{aligned} \tag{5.33}$$

The tether's bending stiffness is simulated by setting the joint limits to a small value and using the ERP and CFM parameters for the joint limit constraint of each axis of the universal joint. Likewise, the torsional stiffness is simulated by setting the appropriate values for the ERP and CFM parameters of the universal joint in the constrained direction. In other words, the constraints used for the bending stiffness pertain to the joint limits while the constraints for the torsional stiffness stem from

the "no rotation" constrain on third (z-axis in our case) of the universal joint. It is worth mentioning that joint stiffness has been experimentally chosen such that simulation behavior resembles that of the physical system when bending is induced magnetically, however, further work to characterize the stiffness is anticipated.

In addition, a custom Gazebo plug-in was developed to simulate the magnetic interaction between permanent magnets (open source [150]). The plugin computes the magnetic fields as well the forces and torques induced on magnetic objects using the dipole-dipole model. The magnetic field computation is published as sensor output on the ROS network allowing for development pose estimation algorithms while the computed forces and torques are applied on the magnetic object the motion of which is then computer by ODE(or any other underlying physics engine). Although the accuracy of the dipole-dipole model degrades as the two magnets come near each other, it is very simple and can be computed efficiently. As our control algorithms rely on pose estimation as feedback, the dipole-dipole model is sufficient for our application.

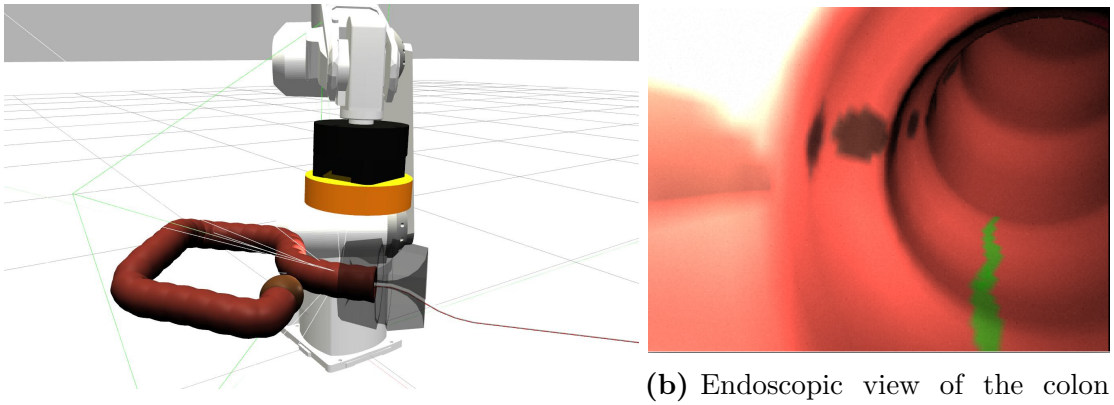

(a) Simulated environment with robot, tethered-capsule, colon mesh.

(b) Endoscopic view of the colon from simulated camera and light source.

Figure 5.6: Complete simulation system.

A complete simulation system can be achieved by further utilizing the functionalities provided by the Gazebo simulator. As shown in Figure 5.6, the simulation environment contains a light source and a camera simulating endoscopic view inside

a colon. The properties of the light source and the camera can be tuned to match the image characteristics found on the real MAC while the colon can be designed by a 3D CAD tool and imported into Gazebo as a mesh object.

Current limitations of the simulation environment stem from the increased computational cost of using a large number of joints. To speed up the simulation, it is necessary to limit the number of iterations which in turn introduces errors in the computation of contacts between objects. This results in unexpected oscillations the impact of which is primarily observed in the endoscopic view.

Furthermore, interaction of the MAC with the colon tissue is not simulated well owing to the difficulty of simulating soft body contact—a feature not supported by ODE. Further work is needed to add this capability, which will require using a different physics engine.

5.4 Experimental Validation

To assess the viability of our approach, the controllers were tasked with maneuvering the capsule along desired trajectories. The desired trajectories were first simulated using the simulation environment described in Section 5.3. The experimental setup was designed with transparent barriers to visualize the capsule and the tether while being manipulated by the robot. Although this is not how the MAC would be used in medical settings—the capsule would not be visible from outside the patient—the resulting motion from magnetic manipulation would still be valid for our experiments. During each trial, errors in position and velocity were computed using our pose estimation system. However, the enhanced pose estimation system described in Chapter 4 was only developed recently; therefore, some of our the earlier experiments were conducted with an implementation of the pose estimation system developed by Di Natali et al. [34]. Various workarounds for the limitations of the method in [34] have been used. For the singularity limitations, additional techniques such as low pass filters on

previous locations and constraints on the elevation of the capsule have been used. For the yaw initialization problem, we have exploited certain configurations of the EPM and placement of the capsule in known locations to speed up initialization. However, these workarounds are prone to errors and limit the viability of the system for clinical applications. Thus, an additional set of experimental results that utilized the enhanced pose estimation system of Chapter 4 with closed-loop control are provided.

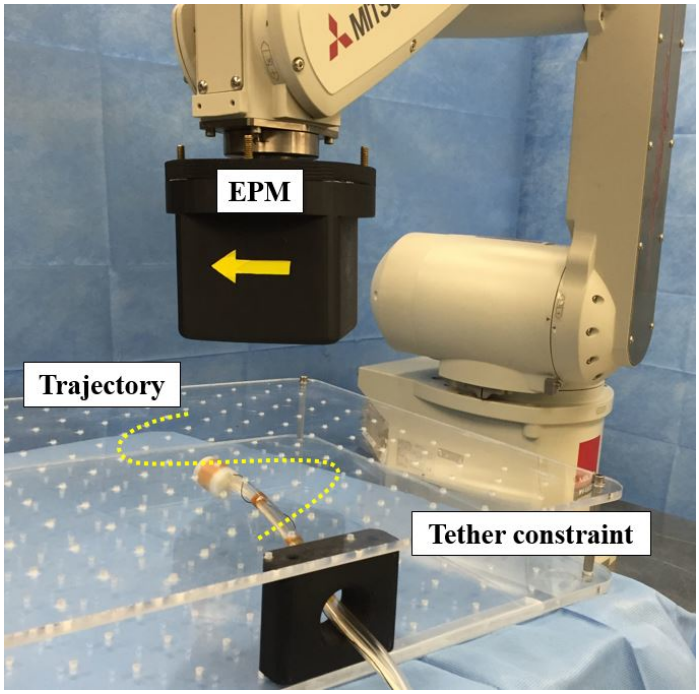

Figure 5.7: Experimental setup for trajectory following of the tethered capsule. The tether is constrained near the beginning of the trajectory. The sinusoidal trajectory is shown for visualization purposes only.

5.4.1 Closed-loop Position Control

For the closed-loop position experiments [151], the tethered capsule was inserted between two transparent horizontal planes acting as vertical barriers for the capsule as shown in Figure 5.7. In addition, the tether was passed through a constraint device with a circular hole that served to prevent lateral motion near the beginning of the planned trajectories. Two sets of trials were conducted on respective trajectory

paths. During each trial, the tethered capsule was commanded to approach a desired position and maintain a commanded heading. A linear proof-of-concept trajectory was used as an initial indicator of desired capsule motion, as was seen in simulation. A sinusoidal trajectory (amplitude = 5.5 cm, wavelength = 20 cm) was implemented to demonstrate the capability of both position and heading control in the presence of tether-induced disturbance. During both sets of trials, the capsule's heading was commanded to align tangentially with the trajectory path and maintain a horizontal orientation so that the capsule is in contact with the barrier along its length. This was implemented with a clinical consideration that necessitates clear visualization of the lumen.

As seen in Figures 5.8 and 5.9, the tethered capsule followed along the generated paths with acceptable accuracy. Four trials were conducted for each trajectory both in simulation and experiment with closed-loop control and localization running at 100 Hz. In the simulation environment, Gaussian noise with a standard deviation of 6 mm was added to simulate the localization errors reported in [34]. The same low pass filter was used in both the simulation and physical environment. For all trajectories, deviations were measured in the lateral (y) direction. Lower deviations were observed in the simulation environment owing to idealized mechanical and frictional properties that could not accurately model the tether's interaction with the environment.

In the straight line trajectory trials, the mean deviation in simulation was 1.1 ± 0.9 mm with a maximum error of 5.2 mm, while the mean deviation in the experiment was 1.2 ± 1.4 mm with a maximum error of 9.6 mm. For the sine wave trajectories, the mean deviation in simulation was 5.0 ± 4.3 mm with a maximum error of 21.9 mm. The mean error in the heading angle was 0.11 ± 0.11 rad with a maximum error of 0.48 rad. For the experimental data, the mean deviation was 10.3 ± 6.7 mm with a maximum error of 35.7 mm. The mean error in the heading angle was 0.26 ± 0.18 rad with a maximum error of 0.71 rad.

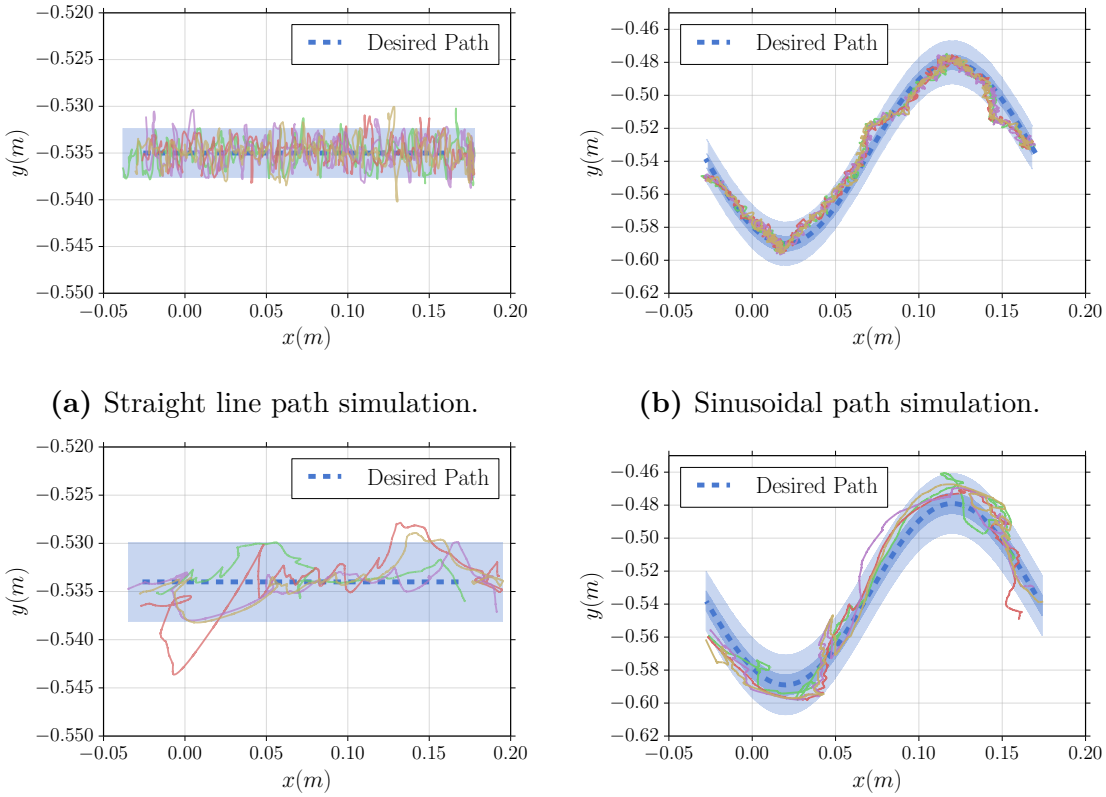

(a) Straight line path simulation.

(b) Sinusoidal path simulation.

(c) Straight line path experiment.

(d) Sinusoidal path experiment.

Figure 5.8: Results of four trials of the capsule being maneuvered through the two types of desired trajectories while maintaining an orientation that is parallel to the vertical barrier surface. The shaded region shows one (only for b, d) and three standard deviations from the mean. Simulation results are shown in (a) and (b) while experimental results are shown in (c) and (d).

The closed-loop control system was able achieve accurate motions within a ±10 mm average boundary. This meets our requirement considering that (a) this error spans the thickness of our capsule (20 mm diameter), and (b) the approximate colon diameter ranges from 34.5 to 75 mm. Although orientation errors of 0.26 rad (15°) were recorded in our experiments, these errors were computed along the trajectory and, therefore, do not fully characterize the static orientation accuracy that could be achieved with the system. Accurate angular motion is required for tissue sampling

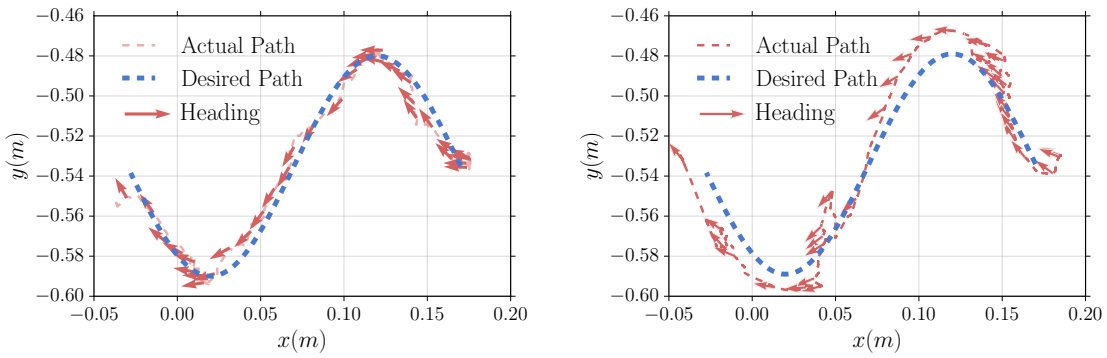

(a) Simulation **(b)** Experiment

Figure 5.9: The tethered capsule was commanded to follow this sinusoidal trajectory starting near $x = 0.2\,\text{m}$ and maintain a heading that was tangential to the sine curve. This heading is parallel to the vertical barrier.

(biopsy or polyp removal) commonly performed with the endoscope held in one stable position, making important to consider static orientation accuracy as a goal to characterize in future work. Larger errors at the start of each path (near $+x$) are due to the start points of each trajectory being set manually and letting the controller command the capsule to the desired path. Additionally, these errors in the sinusoidal trajectory trials can be attributed to the capsule being near the tether constraint where bending is difficult.

5.4.2 Closed-loop Hybrid Position and Velocity Control

The experimental setup for validating the hybrid position and velocity closed-loop controller [152] is shown in Figure 5.10. The setup consists of the 6 DOF serial manipulator, the soft-tethered capsule and an acrylic tube that provided physical constraints akin to the colon. In order to create an environment with realistic friction and resistance forces as would be found in a real colon, the tube was lubricated before the trials.

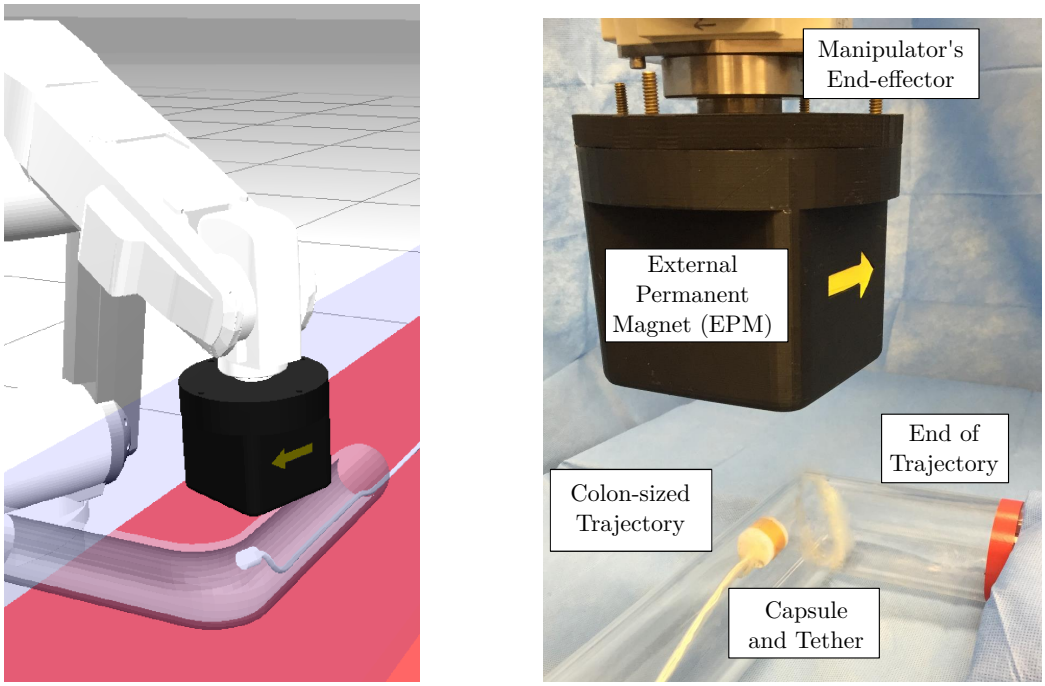

(a) **(b)**

Figure 5.10: (a) Gazebo simulation environment with physics engine and a custom built magnetic interaction plugin. (b) Experimental setup with tethered capsule, robot manipulator and, physical tube providing phyisical constraints. *Reproduced with permission from [152] © 2016 IEEE.*

5.4.2.1 Trajectory Generation

The colon has a diameter of approximately 7 cm that contains multiple bends and is deformable owing to mesentery fixation in only certain segments of the lumen [165]. Although the capsule is intended to be tele-operated when in clinical use, we now focus our attention on control and thus set a fixed trajectory that is commanded and followed autonomously. The input to the controller algorithm is a set of pre-defined trajectory points that roughly describe the trajectory. A spline is then generated once the control algorithm begins that fits a curve that is smooth up to second degree between the path points. A continuum in curvature allows calculating the necessary velocity and heading direction at each time step. A sample fitting between a few points is shown in Figure 5.11.

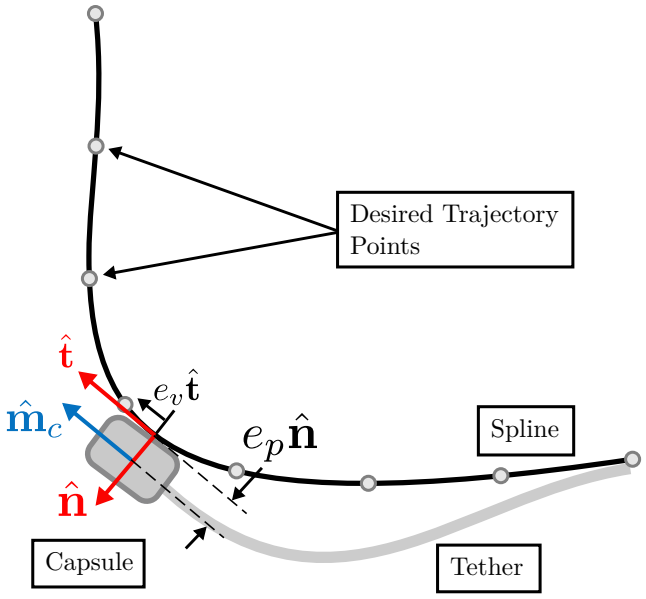

Figure 5.11: Spline fitted to a small number of desired trajectory points.

The use of cubic spline interpolation allows us to create a smooth curve that passes through any number of desired points, allowing us to specify trajectories by a variable number of waypoints. This curve is a stitching of cubic polynomials that join at knots (the waypoints) and, unlike Bezier curves, the order of polynomial functions does not increase with an increased number of waypoints and thus does not become computationally expensive [20]. An additional benefit is that the path, by definition, passes through all waypoints giving more controllability in path generation. This is especially important in ensuring that curve is not generated in an area outside of our desired path (i.e. experimental pseudo-colon acrylic tube). As infinite solutions are possible, one solution can be computed by imposing conditions such as the curve passing through the waypoint i and waypoint $i + 1$ with defined second and third order polynomial coefficients and minimizing bending throughout the path. We utilize the Python SciPy Interpolation package [68] based on algorithms developed by De Boor [29], Cox [27], and Dierckx [36].

5.4.2.2 Experimental Results

Two types of trajectories, each with five trials, were tested [152]. A straight line trajectory was used to asses the step response of the controller while a trajectory with a single bend was used to assess how well the controller followed a given trajectory.

The step response (conducted on the straight segment of the of the acrylic tube) of the velocity controller to a step input of 0.01 m/s is shown in Figure 5.12a. The velocity shown is computed by low pass filtering the discrete time derivative of the position output of the magnetic localization algorithm. The average rise time (time to 90 % of reference input) was 2.51 s, however, because this value is dependent on the cutoff frequency of the low pass filter, it is not a true representation of the rise time. The average maximum velocity error during the ten seconds after the rise time is 0.005 m/s while the average root mean square error during the same period is 0.002 m/s. The fluctuations seen in velocity result from random environmental variables such as friction that varies with the height of the external magnet and alignment of the tether. Although this fluctuation is acceptable considering that it is in velocity, the colon is highly lubricated and we hypothesize that this fluctuation will be reduced.

The results from five trials of the velocity controller following a curved trajectory are shown in Figure 5.12b. This trajectory was chosen as it exemplifies the challenges faced when attempting to maneuver the capsule around a corner in the lumen while maintaining a specified heading and pitch/tilt angle. The speed of the capsule during each trial remained reasonably close to the commanded speed except when making the turn. The deviation can be attributed to the sharp corner in the tube, which causes the capsule to get stuck until its heading is tangent to the lumen of the vertical segment of the tube. The corner also becomes a pivot about which a moment is developed by the tether. The capsule's drift to the left side of the spline in Figure 5.12b can be attributed to this disturbance in moment. A feed-forward torque

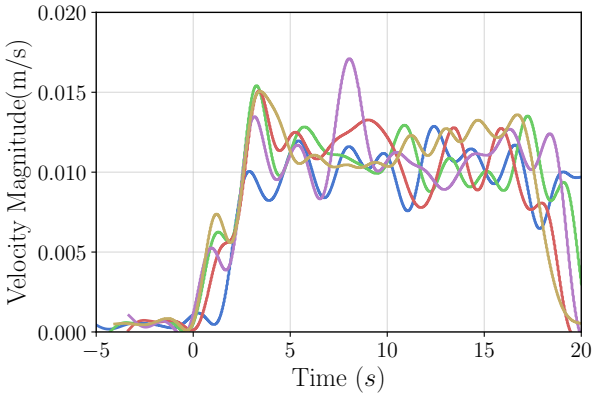

(a)

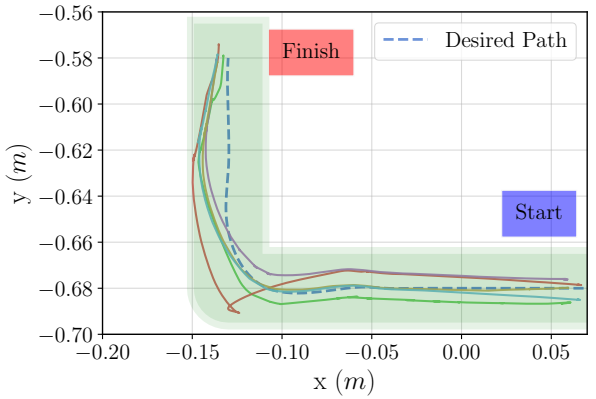

(b)

Figure 5.12: (a) Step response of velocity controller to a reference velocity of 0.01 m/s in a straight line trajectory. (b) Trajectory with a single bend demonstrating trajectory following. The shaded region indicates the physical tube (5 cm internal diameter). *Reproduced with permission from [152] © 2016 IEEE.*

compensation term is necessary to eliminate this error but requires further study of tether mechanics. The trajectory shown in red is an outlier with a loop in the corner of the trajectory. This odd shape resulted from the tether becoming stuck at the entrance of the tube, resulting in the EPM exerting a large force on the capsule, and once the tether's static friction was overcome, the capsule shot forward.

Considering the average length of the colon being 185 cm (187.7 ± 19.0 cm in men, 182.2 ± 18.1 cm in women) [2], our mock-trajectory (32 cm long) is about 17 % of the length of a colon. An average path traversal time of 33.38 s thus results in a

predicted total colon traversal time of 193 s, which is significantly less than open-loop driving of a tethered capsule in a phantom colon (556 ± 188 s) and matched the time to completion in the same phantom using a standard endoscope (194 ± 158 s) [4]. The experimental setup is significantly different and these figures are presented for conceptual comparison only. An additional study is necessary for true comparison.

5.4.3 Experimental Results with Enhanced Pose Estimation

The experimental setup for demonstrating hybrid position and velocity control utilizing the enhanced pose estimation system developed in Chapter 4 is shown in Figure 5.13. Once again, the tethered capsule was inserted between two horizontal planes made of clear acrylic serving as vertical barriers for the capsule. The two acrylic planes were lubricated with vegetable oil in order to reduce friction. A camera tracker was mounted below the bottom acrylic plane to provide ground truth on the 2D position of the capsule; however, its output was not used in the control algorithm. Since we do not have ground truth measurements for the heading of the capsule, we only report errors by comparing the commanded heading with the estimated heading provided by the enhanced pose estimation algorithm. The controller was implemented as a ROS node in Python and ran at a 100 Hz synchronized with the pose estimation algorithm. The two algorithms ran simultaneously on a single PC.

Two sets of 10 trials were conducted where the system was commanded to propel the capsule along a straight line trajectory at a speed of 5 mm/s. In both trials, the capsule's heading was commanded to align with the forward direction of the trajectory.

In the first set of trials (*initial offset experiments*), the initial capsule position was offset in the lateral direction by 55 mm. This experiment was used to assess the response of the controller to an initial offset and its ability to achieve a small steady state error. As seen in Figure 5.14a the capsule's lateral error, on average, was

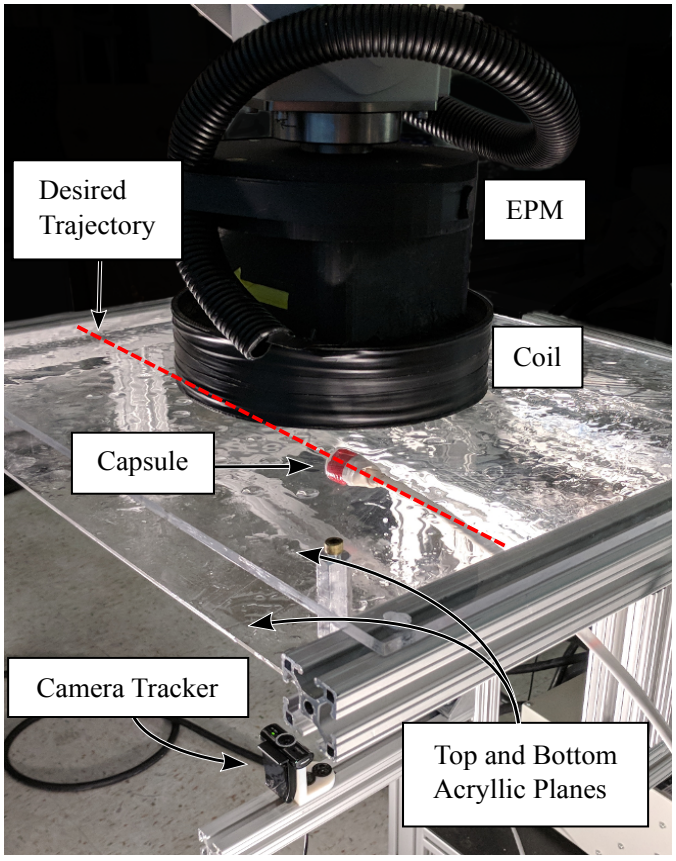

Figure 5.13: Experimental setup for demonstrating closed-loop control utilizing the enhanced pose estimation system. The capsule was painted so that it can be detected by the camera tracker with relative ease. The coil was covered with black tape to prevent erroneous color detection. The two acrylic planes were lubricated with vegetable oil in order to reduce friction.

reduced within the first 10 s of the trajectory. The steady state lateral error computed after the capsule has travelled 30 s was -5.30 ± 2.60 mm. The average heading error over the entire trajectory was $4.96 \pm 2.20°$. As shown in Figure 5.15a, the heading is consistently kept in the direction of forward motion.

In the second set of trials (*disturbance experiments*), the capsule starts without any intentional position error. Once the capsule has travelled 100 mm, a portion of the tether is manually pushed laterally thereby changing the position of the capsule by approximately 40 mm. This disturbance is maintained for approximately 10 s. This experiment was used to assess whether the controller was capable of compensating for

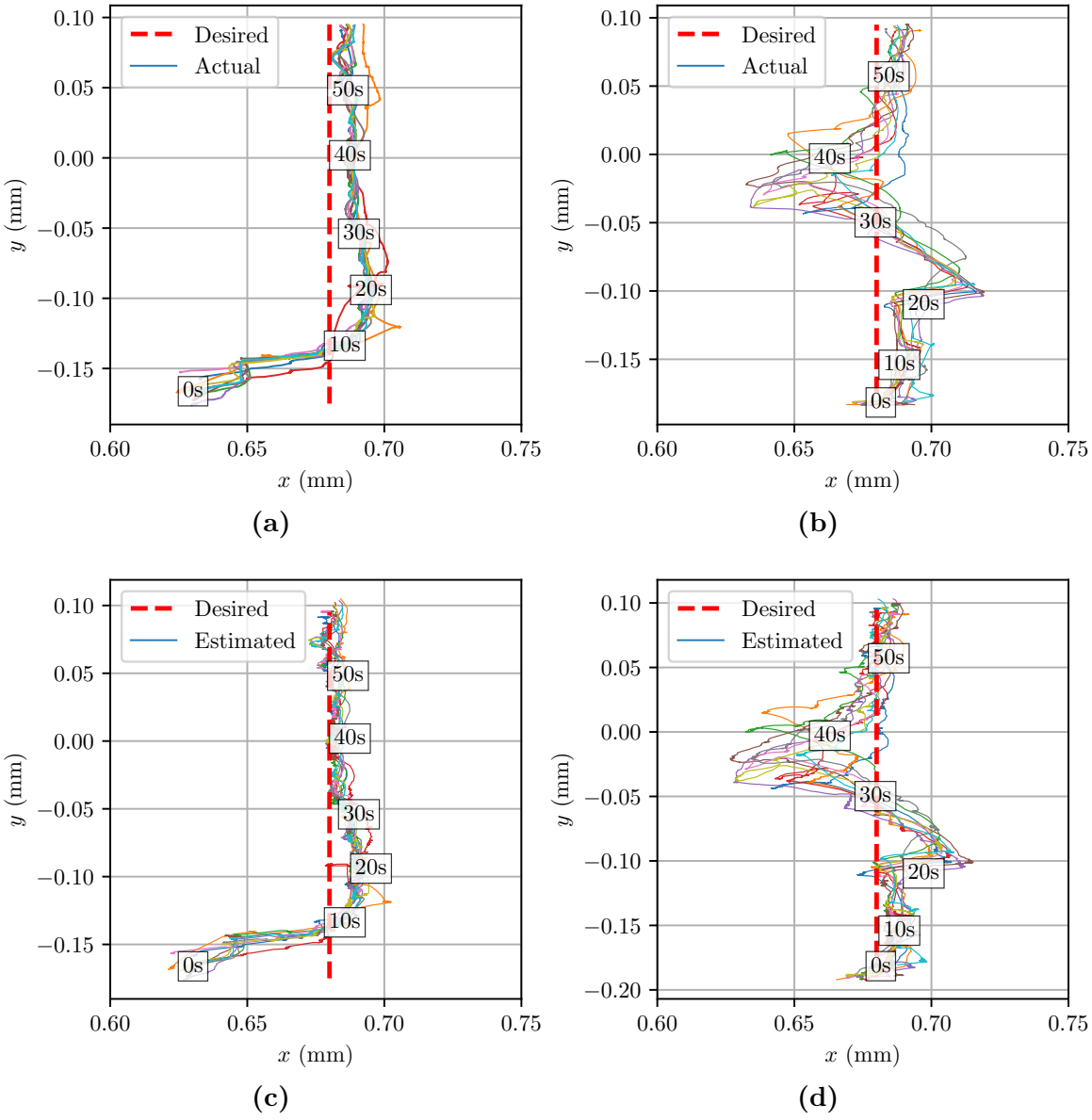

Figure 5.14: Traces of the capsule's trajectory as it was propelled by the EPM with a closed-loop controller. Each colored solid line represents one of the 10 trials. (a, b) Traces obtained using a camera tracker based on color detection. (a) At time 0 s, the capsule's position is offset from the trajectory in the x direction by approximately 55 mm. (b) The tether is pushed in the $+x$ direction as soon as capsule has travelled 100 mm. This is indicated by the spike at time 20 s. The disturbance is maintained for approximately 10 s. (c, d) Traces obtained from the pose estimation algorithm.

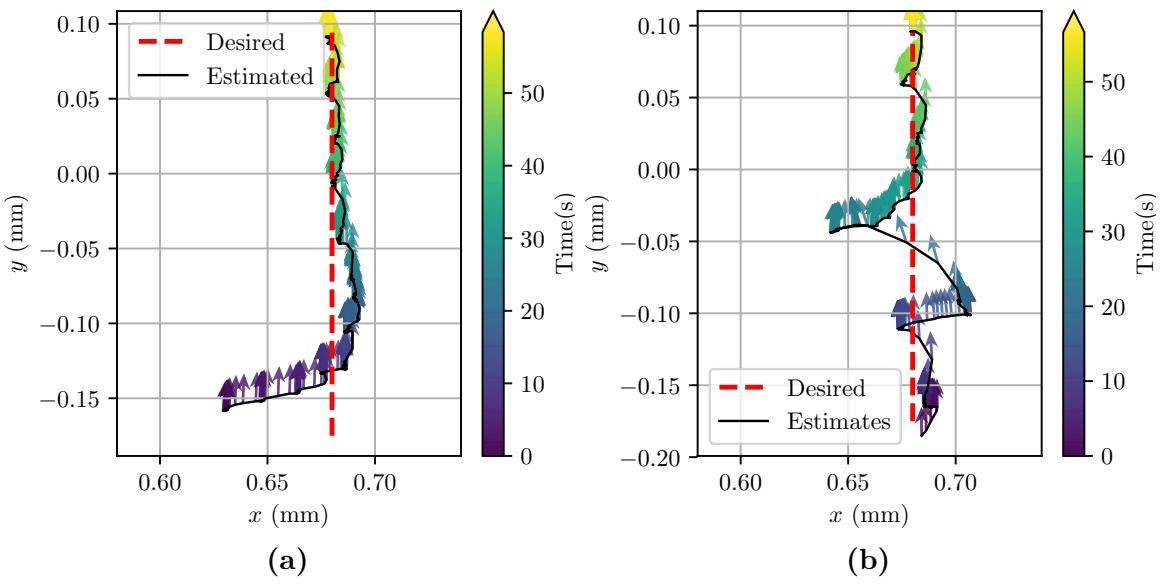

Figure 5.15: Arrows representing the heading direction of the capsule at selected points along the two types of trajectories. For the purposes of good visualization, only a single trial from each set is shown. The heading angles were obtained from the pose estimation algorithm. The color gradation shows the progression of time. (a) Initial offset experiments. (b) Disturbance experiments.

sustained disturbances with its integral component all the while maintaining a desired orientation of the capsule. Figure 5.14b shows traces of the capsule trajectory as the controller responds to the disturbance. The average position error after the controller has recovered from the disturbance at $T = 50\,\text{s}$ was $-7.90 \pm 3.39\,\text{mm}$. The average heading error over the entire trajectory was $7.34 \pm 1.77°$. As shown in Figure 5.15b, the heading error increased during the disturbance, but quickly returned to its desired direction.

The controller was commanded to maintain a vertical force of 0.45 N on the capsule, a value empirically determined to balance the weight of the capsule without exerting excessive force on the vertical barrier. The system computed the magnetic force using the point-dipole model and pose estimates from the enhanced pose estimation algorithm. Accordingly, the average vertical force on the two sets of trials was $0.494 \pm 0.093\,\text{N}$ and $0.502 \pm 0.097\,\text{N}$ respectively. These forces are clinically relevant as they would not cause tissue damage [138]. In maintaining this force, the vertical

distance between the centers of the EPM and the capsule was kept at an average of 158 ± 4 mm and 157 ± 6 mm for the two sets of trials respectively. Considering the size of our EPM, this leaves close to 100 mm of gap between the bottom of the EPM and the vertical barrier in the experiment.

In both sets of trials, it was observed that there was a constant offset between the position output of our pose estimation algorithm and the camera based ground truth. As Figures 5.14c and 5.14d show, the controller would have placed the capsule more accurately on the trajectory had this offset been absent. As mentioned in Section 4.5.2.2, further work is needed to determine the source of this error.

5.5 Conclusion

We have demonstrated closed-loop control of the MAC using two approaches. The position controller can be used for trajectory following, but due to its stop-and-go nature, is more suited for tasks that have a single destination. An example of such a task is holding the capsule in place and compensating for disturbances while the physician is inserting a tool through the instrument channel of the MAC. The hybrid velocity and position controller is better suited for trajectory following. This makes it a key component in implementing tele-operation where forward motion is controlled by the physician.

The successful implementation of magnetic pose estimation on the MAC system enabled the use of these control schemes to follow commanded position and orientation trajectories. The observed position errors were within the geometry of the capsule itself and well within the bounds of an average colon diameter and thus acceptable for the screening procedure. Previous studies have demonstrated trajectory following of untethered capsules with limitations such as mechanically constraining a capsule's motion [126] or submerging the capsule and controlling its orientation in open-loop [90].

Along with the development of these control algorithms, we have created a simulation environment by modeling our soft tether as a chain of rigid links and developing a custom magnetic interaction plug-in for Gazebo, an open source dynamic simulator. Once the controllers and the trajectory following experiments were successfully tested in simulation, they were implemented on our physical platform with minimal effort with the exception of requiring additional tuning of controller gains.

CHAPTER 6

Conclusion

Magnetic actuation is currently the most promising approach for actively and wirelessly manipulating capsule endoscopes. Once capsule endoscopes (CEs) can be actively actuated, they have the potential to transform current medical practice and significantly improve patient outcomes. With the ability to reach parts of the gastrointestinal (GI) that were previously difficult to reach, actively manipulated CEs can be used to diagnose pathologies that currently go undiagnosed. While biopsy and administration of therapy is currently difficult with wireless CEs, compromises can be made with soft tethers, as in the Magnetically Actuated Capsule (MAC) system described in Chapter 2, to gain these capabilities. In this dissertation, two fundamental problems in magnetic guidance have been addressed to achieve active actuation of the MAC and advance the system toward adoption in clinical practice.

A novel pose estimation algorithm that utilizes a hybrid assembly of a permanent magnet and an electromagnet was presented. This approach overcomes two important limitations that hinder the use of prior pose estimation systems for magnetically driven robotic capsule endoscopy in clinical settings: (1) magnetic singularity and (2) the need for accurate yaw angle initialization. Magnetic field singularities are inherent in all magnetic pose estimation methods that utilize a single source of magnetic field. An exception can be made if the method relies on motion of the magnet to obtain multiple measurements from different vantage points while the capsule remains stationary; however, this method would not be well suited for magnetic guidance. The magnetic field singularity problem was studied in this dissertation by analyzing the workspace of current pose estimation methods with the use of the point-dipole magnetic field model. We showed that singular regions exist in areas where the

capsule is nominally located during magnetic actuation. Since the dipole model can approximate most magnetic field sources, the problem, and therefore the solution, discussed in this dissertation pertains to a wider set of pose estimation techniques.

Another contribution of this dissertation is the development of closed-loop control algorithms that make use of magnetic pose estimation for real-time feedback. Two schemes of closed-loop control were explored for creating the necessary algorithmic building blocks for effective autonomous or human controlled tele-operation. Our pose estimation method was experimentally shown to fulfill the criteria needed for closed-loop control in terms of accuracy, update rate and size of workspace making it suitable for use in tele-operated or autonomous operation of magnetically actuated robotic capsule endoscopes in clinical settings. In particular, tele-operated robotic manipulation can now be approached by combining our pose estimation algorithm and the closed-loop control schemes described in this dissertation with intuitive user interfaces and user feedback mechanisms.

The simulation environment developed during the course of this dissertation can be used in developing these user interfaces. Preliminary work has shown promising results in integrating the simulation environment with custom designed user interfaces although more work is needed in enhancing the fidelity of the simulation (*e.g.* soft tissue interaction). However, even in its current state, the simulation environment can be valuable in creating training systems for users of the MAC system.

6.1 Future Directions

Although outcomes from our pose estimation and closed-loop manipulation experiments were promising, further work is necessary. In particular, more work is needed in modeling and characterization of the mechanical properties of the tether. Currently, all effects of the tether and capsule friction are treated implicitly as disturbances in capsule motion. We hypothesize that estimation and explicit incorporation

of these disturbing forces and torques in the control scheme will assist in maneuvering inside the space-constrained colon. However, it is not presently clear if there are cost effective and practical sensors for detecting the shape and position of the tether thus making modeling of the tether a challenging endeavor.

The nonlinear relationship between the pose of the external permanent magnet (EPM) and the resulting forces and torques on the capsule have been dealt with by linearizing the relationship at each time step. As a result, solutions as to where to move the EPM are, at best, only locally optimal. We anticipate that the complexity of the manipulation task will be increased when introducing humans into the equation (tele-operation). More complexity is also expected as additional constraints on the motion of the EPM, such as those needed to ensure collision avoidance, are added to the system. In these circumstances, our current methods may fail to find solutions due to local minima. Approaches such as model predictive control (MPC) might provide better solutions as they take multiple future time steps into account and are capable of handling state and input constraints [35, 130].

The long term goal of the MAC project is to create a viable alternative to the traditional endoscope that encourages patient participation in screening procedures by eliminating pain, discomfort, and the need for sedation. To this end, clinical trials involving unsedated human subjects is the necessary next step. These trials would not only inform the extent to which patients can undergo the procedure without sedation, but would also be invaluable in collecting feedback for the improvement of the design of the soft-tethered device, the control algorithms, and the user interfaces. We anticipate that these trials can be conducted in the next five to ten years. During that time, progress could also be made in preparing the system for commercialization, a major component of which is obtaining approval from the Food and Drug Administration (FDA). On the more technical perspective, progress could also be made in implementing fully autonomous navigation of the colon. Recent advances in deep learning and

computer vision have been demonstrated for polyp [12] and lumen detection [167] as well environment mapping [162]. Combined with closed-loop robotic control, these technologies can enable the next era of capsule endoscopy.

APPENDIX A

Nomenclature

Notation	**Description**
$\mathbf{f_m}$	Force induced by EPM on capsule.
I	Identity matrix $\in \mathbb{R}^3$.
M	Matrix (uppercase).
$\mathbf{m_E}$	Magnetic moment of EPM.
$\mathbf{m_\varsigma}$	Magnetic moment of capsule's magnet.
$\mathbf{p_E}$	Position of the EPM attached to robot end-effector.
$\mathbf{p_\varsigma}$	Capsule position.
$\mathbf{p} = \mathbf{p_\varsigma} - \mathbf{p_E}$	Relative capsule position vector.
$\boldsymbol{\tau}_\mathbf{m}$	Torque induced by EPM on capsule.
$\dot{\mathbf{v}}$	Rate of change of parameter with respect to time.
$\mathbf{v}$	Vector (lowercase, bold).
$\hat{\mathbf{v}}$	Unit vector.

APPENDIX B

Derivation of Jacobian

The following is a derivation of the terms of the Jacobian $J_{\mathcal{F}}(\mathbf{p}, \hat{\mathbf{m}}_\mathbf{a}, \hat{\mathbf{m}}_\mathbf{c})$. Each term of $J_{\mathcal{F}}$ represents a partial derivation of the force and torque equations of the dipole-dipole model.

$$J_{\mathcal{F}}(\mathbf{p}, \hat{\mathbf{m}}_\mathbf{a}, \hat{\mathbf{m}}_\mathbf{c}) = \begin{bmatrix} F_p & F_{ma} & F_{mc} \\ T_p & T_{ma} & T_{mc} \end{bmatrix} \tag{B.1}$$

where $G = I - \hat{\mathbf{p}}\hat{\mathbf{p}}^\top$, $Z = I - 5\hat{\mathbf{p}}\hat{\mathbf{p}}^\top$, and $D = 3\hat{\mathbf{p}}\hat{\mathbf{p}}^\top - I$. The terms of the Jacobian are defined as follows

$$\begin{aligned} F_p &= \frac{\partial \mathbf{f}_\mathbf{m}(\mathbf{p}, \hat{\mathbf{m}}_\mathbf{a}, \hat{\mathbf{m}}_\mathbf{c})}{\partial \mathbf{p}} \\ &= \frac{3\mu_0 \left\|\mathbf{m}_\mathbf{a}\right\| \left\|\mathbf{m}_\mathbf{c}\right\|}{4\pi \left\|\mathbf{p}\right\|^5} \Big(\hat{\mathbf{m}}_\mathbf{a}\hat{\mathbf{m}}_\mathbf{c}{}^\top Z + \hat{\mathbf{m}}_\mathbf{c}\hat{\mathbf{m}}_\mathbf{a}{}^\top Z + \hat{\mathbf{m}}_\mathbf{c}{}^\top \hat{\mathbf{m}}_\mathbf{a} Z \\ &\quad - 5\hat{\mathbf{p}}\hat{\mathbf{p}}^\top \hat{\mathbf{m}}_\mathbf{a}\hat{\mathbf{m}}_\mathbf{c}{}^\top G - 5\hat{\mathbf{p}}\hat{\mathbf{p}}^\top \hat{\mathbf{m}}_\mathbf{c}\hat{\mathbf{m}}_\mathbf{a}{}^\top G - 5\hat{\mathbf{m}}_\mathbf{c}{}^\top \hat{\mathbf{p}}\hat{\mathbf{p}}^\top \hat{\mathbf{m}}_\mathbf{a} Z \Big) \end{aligned} \tag{B.2}$$

$$\begin{aligned} F_{ma} &= \frac{\partial \mathbf{f}_\mathbf{m}(\mathbf{p}, \hat{\mathbf{m}}_\mathbf{a}, \hat{\mathbf{m}}_\mathbf{c})}{\partial \hat{\mathbf{m}}_\mathbf{a}} \\ &= \frac{3\mu_0 \left\|\mathbf{m}_\mathbf{a}\right\| \left\|\mathbf{m}_\mathbf{c}\right\|}{4\pi \left\|\mathbf{p}\right\|^4} \left(\hat{\mathbf{m}}_\mathbf{c}{}^\top \hat{\mathbf{p}} I + \hat{\mathbf{m}}_\mathbf{c}\hat{\mathbf{p}}^\top + \hat{\mathbf{p}}\hat{\mathbf{m}}_\mathbf{c}{}^\top Z \right) \end{aligned} \tag{B.3}$$

$$\begin{aligned} F_{mc} &= \frac{\partial \mathbf{f}_\mathbf{m}(\mathbf{p}, \hat{\mathbf{m}}_\mathbf{a}, \hat{\mathbf{m}}_\mathbf{c})}{\partial \hat{\mathbf{m}}_\mathbf{c}} \\ &= \frac{3\mu_0 \left\|\mathbf{m}_\mathbf{a}\right\| \left\|\mathbf{m}_\mathbf{c}\right\|}{4\pi \left\|\mathbf{p}\right\|^4} \left(\hat{\mathbf{m}}_\mathbf{a}\hat{\mathbf{p}}^\top + \hat{\mathbf{m}}_\mathbf{a}{}^\top \hat{\mathbf{p}} I + \hat{\mathbf{p}}\hat{\mathbf{m}}_\mathbf{a}{}^\top Z \right) \end{aligned} \tag{B.4}$$

$$\begin{aligned} T_p &= \frac{\partial \boldsymbol{\tau}_\mathbf{m}(\mathbf{p}, \hat{\mathbf{m}}_\mathbf{a}, \hat{\mathbf{m}}_\mathbf{c})}{\partial \mathbf{p}} \\ &= \frac{3\mu_0 \left\|\mathbf{m}_\mathbf{a}\right\| \left\|\mathbf{m}_\mathbf{c}\right\|}{4\pi} \Bigg(S\left(\frac{\hat{\mathbf{m}}_\mathbf{c}}{\left\|\mathbf{p}\right\|^3}\right) \left(\hat{\mathbf{p}}\hat{\mathbf{m}}_\mathbf{a}{}^\top \left(\frac{G}{\left\|\mathbf{p}\right\|}\right) \right. \\ &\quad \left. + \left(\frac{G}{\left\|\mathbf{p}\right\|}\right) \hat{\mathbf{p}}^\top \hat{\mathbf{m}}_\mathbf{a} \right) + S(D\hat{\mathbf{m}}_\mathbf{a}) \left(\frac{\hat{\mathbf{m}}_\mathbf{c}\hat{\mathbf{p}}^\top}{\left\|\mathbf{p}\right\|^4}\right) \Bigg) \end{aligned} \tag{B.5}$$

$$T_{ma} = \frac{\partial \boldsymbol{\tau}_{\mathbf{m}}(\mathbf{p}, \hat{\mathbf{m}}_{\mathbf{a}}, \hat{\mathbf{m}}_{\mathbf{c}})}{\partial \hat{\mathbf{m}}_{\mathbf{a}}}$$
$$= \frac{\mu_0 \left\|\mathbf{m}_{\mathbf{a}}\right\| \left\|\mathbf{m}_{\mathbf{c}}\right\|}{4\pi \left\|\mathbf{p}\right\|^3} S(\hat{\mathbf{m}}_{\mathbf{c}}) D \tag{B.6}$$

$$T_{mc} = \frac{\partial \boldsymbol{\tau}_{\mathbf{m}}(\mathbf{p}, \hat{\mathbf{m}}_{\mathbf{a}}, \hat{\mathbf{m}}_{\mathbf{c}})}{\partial \hat{\mathbf{m}}_{\mathbf{c}}}$$
$$= -\frac{\mu_0 \left\|\mathbf{m}_{\mathbf{a}}\right\| \left\|\mathbf{m}_{\mathbf{c}}\right\|}{4\pi \left\|\mathbf{p}\right\|^3} S(D\hat{\mathbf{m}}_{\mathbf{a}}) \tag{B.7}$$

REFERENCES

[1] M. Aghanouri, A. Ghaffari, and N. Dadashi. "Image-based localization of the active wireless capsule endoscope inside the stomach". In: *2017 IEEE EMBS International Conference on Biomedical and Health Informatics, BHI 2017*. 2017, pp. 13–16.

[2] A. Alazmani, A. Hood, D. Jayne, A. Neville, and P. Culmer. "Quantitative assessment of colorectal morphology: Implications for robotic colonoscopy". In: *Medical Engineering & Physics* 38.2 (2016), pp. 148–154.

[3] I. Aoki, A. Uchiyama, K. Arai, K. Ishiyama, and S. Yabukami. *Detecting system of position and posture of capsule medical device*. US Patent 7,815,563. 2010.

[4] A. Arezzo, A. Menciassi, P. Valdastri, G. Ciuti, G. Lucarini, M. Salerno, C. Di Natali, M. Verra, P. Dario, and M. Morino. "Experimental assessment of a novel robotically-driven endoscopic capsule compared to traditional colonoscopy." In: *Digestive and Liver Disease* 45.8 (Aug. 2013), pp. 657–62.

[5] K. Arshak and F. Adepoju. "Adaptive linearized methods for tracking a moving telemetry capsule". In: *IEEE International Symposium on Industrial Electronics* (2007), pp. 2703–2708.

[6] M. S. Arulampalam, S. Maskell, N. Gordon, and T. Clapp. "A Tutorial on Particle Filters for Online Nonlinear/Non-Gaussian Bayesian Tracking". In: *IEEE Transactions on Signal Processing* 50.2 (2002), pp. 174–188.

[7] K. S. Arun, T. S. Huang, and S. D. Blostein. "Least-Squares Fitting of Two 3-D Point Sets". In: *IEEE Transactions on Pattern Analysis and Machine Intelligence* 9.5 (1987), pp. 698–700.

[8] G. Bao, K. Pahlavan, and L. Mi. "Hybrid Localization of Microrobotic Endoscopic Capsule Inside Small Intestine by Data Fusion of Vision and RF Sensors". In: *IEEE Sensors Journal* 15.5 (2015), pp. 2669–2678.

[9] M. Beccani, C. Di Natali, M. E. Rentschler, and P. Valdastri. "Wireless tissue palpation: Proof of concept for a single degree of freedom". In: *2013 IEEE International Conference on Robotics and Automation*. May 2013, pp. 711–717.

[10] G. Berci and K. A. Forde. "History of endoscopy: What lessons have we learned from the past?" In: *Surgical Endoscopy* 14.1 (2000), pp. 5–15.

[11] R. Bozzi, A. Inzirillo, V. D. I. Martino, M. Sannino, F. Piantadosi, D. Cattaneo, U. O. C. Chirurgia, E. D. Endoscopia, D. Azienda, O. Dei, and C. Napoli. "Endotics System , a New Way To Undergo the Endoscopic Valuation of Lower Gi Tract : Our Initial Experience ." In: (2013), p. 2013.

[12] P. Brandao, O. Zisimopoulos, E. Mazomenos, G. Ciuti, J. Bernal, M. Visentini-Scarzanella, A. Menciassi, P. Dario, A. Koulaouzidis, A. Arezzo, et al. "Towards a Computed-Aided Diagnosis System in Colonoscopy: Automatic Polyp Segmentation Using Convolution Neural Networks". In: *Journal of Medical Robotics Research* 3.02 (2018), p. 1840002.

[13] F. Carpi, N. Kastelein, M. Talcott, and C. Pappone. "Magnetically controllable gastrointestinal steering of video capsules". In: *IEEE Transactions on Biomedical Engineering* 58.2 (2011), pp. 231–234.

[14] F. Carpi and H. Shaheed. "Grand challenges in magnetic capsule endoscopy". In: *Expert Review of Medical Devices* 10.4 (2013), pp. 433–436.

[15] F. Carpi, S. Galbiati, and A. Carpi. "Controlled navigation of endoscopic capsules: Concept and preliminary experimental investigations". In: *IEEE Trans. Biomed. Eng.* 54.11 (2007), pp. 2028–2036.

[16] F. Carpi, S. Galbiati, and A. Carpi. “Magnetic shells for gastrointestinal endoscopic capsules as a means to control their motion”. In: *Biomed. Pharmacother.* 60.8 (2006), pp. 370–374.

[17] F. Carpi and C. Pappone. “Stereotaxis Niobe magnetic navigation system for endocardial catheter ablation and gastrointestinal capsule endoscopy.” In: *Expert Review of Medical Devices* 6.5 (2009), pp. 487–98.

[18] Centers for Disease Control and Prevention. *Colorectal Cancer Tests Save Lives*. URL: `https://www.cdc.gov/vitalsigns/colorectalcancerscreening/index.html` (visited on 09/25/2017).

[19] T. F. Chan and R. V. Dubey. “A weighted least-norm solution based scheme for avoiding joint limits for redundant joint manipulators”. In: *IEEE Transactions on Robotics and Automation* 11.2 (1995), pp. 286–292.

[20] Y. Chen. “High-Order Polynomial Interpolation Based on the Interpolation Center’s Neighborhood The Amendment to the Runge Phenomenon”. In: *Software Eng., 2009. WCSE’09. WRI World Congress on*. Vol. 2. IEEE. 2009, pp. 345–348.

[21] Z. H. E. Chen. “Bayesian Filtering: From Kalman Filters to Particle Filters, and Beyond VI Sequential Monte Carlo Estimation: Particle Filters”. In: *Statistics* 182.1 (2003), pp. 1–69.

[22] G. Ciuti, R. Donlin, P. Valdastri, A. Arezzo, A. Menciassi, M. Morino, and P. Dario. “Robotic versus manual control in magnetic steering of an endoscopic capsule”. In: *Endoscopy* 42.02 (Dec. 2009), pp. 148–152.

[23] G. Ciuti, M. Salerno, G. Lucarini, P. Valdastri, A. Arezzo, A. Menciassi, M. Morino, and P. Dario. “Comparative evaluation study of control methodologies and user interfaces for a robotic-aided endoscopic platform”. In: *International Journal of Computer Assisted Radiology and Surgery* 6.2 (2011), S288–S289.

[24] G. Ciuti, R. Caliò, D. Camboni, L. Neri, F. Bianchi, A. Arezzo, A. Koulaouzidis, S. Schostek, D. Stoyanov, C. M. Oddo, B. Magnani, A. Menciassi, M. Morino, M. O. Schurr, and P. Dario. "Frontiers of robotic endoscopic capsules: a review". In: *J. Micro-Bio Robot.* 11.1-4 (June 2016), pp. 1–18.

[25] G. Ciuti, P. Valdastri, A. Menciassi, and P. Dario. "Robotic magnetic steering and locomotion of capsule endoscope for diagnostic and surgical endoluminal procedures". In: *Robotica* 28.02 (Oct. 2009), p. 199.

[26] F. Cosentino. "Functional evaluation of the Endotics System , a new disposable self-propelled robotic colonoscope : In vitro tests and clinical trial Functional evaluation of the Endotics System , a new disposable self-propelled robotic colonoscope : in vitro tests and". In: *The International Journal of Artificial Organs* 32.8 (2009), pp. 517–527.

[27] M. G. Cox. "The numerical evaluation of B-splines". In: *IMA Journal of Applied Mathematics* 10.2 (1972), pp. 134–149.

[28] P. Dario, C. Stefanini, and A. Menciassi. "Modeling and experiments on a legged microrobot locomoting in a tubular, compliant and slippery environment". In: *Springer Tracts Adv. Robot.* 21 (2006), pp. 165–174.

[29] C. De Boor. "On calculating with B-splines". In: *Journal of Approximation Theory* 6.1 (1972), pp. 50–62.

[30] U. W. Denzer, T. Rösch, B. Hoytat, M. Abdel-Hamid, X. Hebuterne, G. Vanbiervielt, J. Filippi, H. Ogata, N. Hosoe, K. Ohtsuka, N. Ogata, K. Ikeda, H. Aihara, S.-e. Kudo, H. Tajiri, A. Treszl, K. Wegscheider, M. Greff, and J.-f. Rey. "Magnetically Guided Capsule Versus Conventional Gastroscopy for Upper Abdominal Complaints". In: *Journal of Clinical Gastroenterology* 49.2 (Feb. 2015), pp. 101–107.

[31] N. Derby and S. Olbert. “Cylindrical Magnets and Ideal Solenoids”. In: *American Journal of Physics* 78.229 (2009), p. 12. arXiv: 0909.3880.

[32] C. Di Natali, M. Beccani, K. L. Obstein, and P. Valdastri. “A wireless platform for in vivo measurement of resistance properties of the gastrointestinal tract”. In: *Physiological Measurement* 35.7 (2014), p. 1197.

[33] C. Di Natali, M. Beccani, N. Simaan, and P. Valdastri. “Jacobian-based iterative method for magnetic localization in robotic capsule endoscopy”. In: *IEEE Transactions on Robotics* 32.2 (2016), pp. 327–338.

[34] C. Di Natali, M. Beccani, and P. Valdastri. “Real-time pose detection for magnetic medical devices”. In: *IEEE Transactions on Magnetics* 49.7 (2013), pp. 3524–3527.

[35] M. Diehl, H. J. Ferreau, and N. Haverbeke. “Efficient Numerical Methods for Nonlinear MPC and Moving Horizon Estimation”. In: *Nonlinear Model Predictive Control: Towards New Challenging Applications*. Ed. by L. Magni, D. M. Raimondo, and F. Allgöwer. Berlin, Heidelberg: Springer Berlin Heidelberg, 2009, pp. 391–417.

[36] P. Dierckx. *An improved algorithm for curve fitting with spline functions*. Department of Computer Science, KU Leuven, Leuven, Belgium, 1981.

[37] E. Diller, J. Giltinan, and M. Sitti. “Independent control of multiple magnetic microrobots in three dimensions”. In: *Int. J. Rob. Res.* 32.5 (2013), pp. 614–631.

[38] K. Duda, T. Zielinski, R. Fraczek, J. Bulat, and M. Duplaga. “Localization of Endoscopic Capsule in the GI Tract Based on MPEG-7 Visual Descriptors”. In: *2007 IEEE International Workshop on Imaging Systems and Techniques* (2007), pp. 1–4.

[39] C. L. Dumoulin, S. P. Souza, and R. D. Darrow. "Real-time position monitoring of invasive devices using magnetic resonance". In: *Magnetic Resonance in Medicine* 29.3 (Mar. 1993), pp. 411–415.

[40] A. Eickhoff, R. Jakobs, A. Kamal, S. Mermash, J. Riemann, and J. van Dam. "In vitro evaluation of forces exerted by a new computer-assisted colonoscope (the NeoGuide Endoscopy System)". In: *Endoscopy* 38.12 (Dec. 2006), pp. 1224–1229.

[41] D. Fischer, R. Shreiber, G. Meron, M. Frisch, H. Jacob, and A. Glukhovsky. "Localization of the wireless capsule endoscope in its passage through the GI tract". In: *Gastrointestinal Endoscopy* 53.5 (Apr. 2001), AB126.

[42] M. Flückiger and B. J. Nelson. "Ultrasound emitter localization in heterogeneous media". In: *Annual International Conference of the IEEE Engineering in Medicine and Biology - Proceedings*. 2007, pp. 2867–2870.

[43] T. W. R. Fountain, P. V. Kailat, and J. J. Abbott. "Wireless control of magnetic helical microrobots using a rotating-permanent-magnet manipulator". In: *2010 IEEE International Conference on Robotics and Automation*. 2010, pp. 576–581.

[44] A. M. Franz, T. Haidegger, W. Birkfellner, K. Cleary, T. M. Peters, and L. Maier-Hein. "Electromagnetic tracking in medicine -A review of technology, validation, and applications". In: *IEEE Transactions on Medical Imaging* 33.8 (2014), pp. 1702–1725.

[45] E. P. Furlani. *Permanent Magnet and Electromechanical Devices: Materials, Analysis, and Applications*. Electromagnetism. Elsevier Science, 2001.

[46] Y. Geng and K. Pahlavan. "Design, Implementation, and Fundamental Limits of Image and RF Based Wireless Capsule Endoscopy Hybrid Localization". In: *IEEE Transactions on Mobile Computing* 15.8 (2016), pp. 1951–1964.

[47] G. G. Ginsberg, M. L. Kochman, I. D. Norton, and C. J. Gostout. *Clinical Gastrointestinal Endoscopy E-Book*. Elsevier Health Sciences, 2011.

[48] G. Goertzel. "An Algorithm for the evaluation of finite trigonometric series". In: *American Mathematical Monthly* 65.1 (1958), pp. 34–35.

[49] S. T. Goh, S. A. Zekavat, and K. Pahlavan. "DOA-based endoscopy capsule localization and orientation estimation via unscented kalman filter". In: *IEEE Sensors Journal* 14.11 (2014), pp. 3819–3829.

[50] N. J. Gordon, D. J. Salmond, and A. F. Smith. "Novel approach to nonlinear/non-Gaussian Bayesian state estimation". In: *IEE Proceedings F (Radar and Signal Processing)*. Vol. 140. 2. IET. 1993, pp. 107–113.

[51] U. Hany and L. Akter. "Non-Parametric Approach of Video Capsule Endoscope Localization Using Suboptimal Method of Position Bounded CWCL". In: *IEEE Sensors Journal* 17.20 (Oct. 2017), pp. 6806–6815.

[52] F. J. Harris. "On the Use of Windows with the Discrete for Harmonic Analysis Fourier Transform". In: *Proceedings of the IEEE* 66.1 (1978), pp. 51–83.

[53] X. He, Z. Zheng, and C. Hu. "Magnetic localization and orientation of the capsule endoscope based on a random complex algorithm". In: *Medical Devices: Evidence and Research* 8 (2015), pp. 175–184.

[54] H. H. Hopkins and N. S. Kapany. "A Flexible Fibrescope, using Static Scanning". In: *Nature* 173 (1954), pp. 39–41.

[55] J. M. Hsu and S. C. Peters. "Extending Open Dynamics Engine for the DARPA Virtual Robotics Challenge". In: *Simulation, Model. Program. Auton. Robot.* Ed. by D. Brugali, J. F. Broenink, T. Kroeger, and B. A. MacDonald. Cham: Springer International Publishing, 2014, pp. 37–48.

[56] C. Hu, M. Li, S. Song, W. Yang, R. Zhang, and M.-H. Meng. "A Cubic 3-Axis Magnetic Sensor Array for Wirelessly Tracking Magnet Position and Orientation". In: *Sensors Journal, IEEE* 10.5 (2010), pp. 903–913.

[57] C. Hu, M. Q.-H. Meng, and M. Mandal. "The Calibration of 3-Axis Magnetic Sensor Array System for Tracking Wireless Capsule Endoscope". In: *2006 IEEE/RSJ International Conference on Intelligent Robots and Systems* (2006), pp. 162–167.

[58] C. Hu, M. Q. Meng, and M. Mandal. "Efficient magnetic localization and orientation technique for capsule endoscopy". In: *2005 IEEE/RSJ International Conference on Intelligent Robots and Systems, IROS* (2005), pp. 3365–3370.

[59] C. Hu, M.-H. Meng, and M. Mandal. "Efficient Linear Algorithm for Magnetic Localization and Orientation in Capsule Endoscopy". In: *Engineering in Medicine and Biology Society, 2005. IEEE-EMBS 2005. 27th Annual International Conference of the* (2005), pp. 7143–7146.

[60] D. K. Iakovidis, E. Spyrou, D. Diamantis, and I. Tsiompanidis. "Capsule endoscope localization based on visual features". In: *13th IEEE International Conference on BioInformatics and BioEngineering* (2013), pp. 1–4.

[61] G. Iddan, G. Meron, A. Glukhovsky, and P. Swain. "Wireless Capsule Endoscopy". In: *Nature* 405.6785 (May 2000), pp. 417–417.

[62] Invendo Medical GmbH. *Invendo Medical GmbH*. URL: `http://www.invendo-medical.com/for-patients/invendo-your-personal-colonoscope/` (visited on 10/19/2017).

[63] M. N. Islam and A. J. Fleming. "A novel and compatible sensing coil for a capsule in wireless capsule endoscopy for real time localization". In: *Proceedings of IEEE Sensors* 2014-Decem.December (2014), pp. 1607–1610.

[64] T. Ito, D. Anzai, and J. Wang. “A Modified Particle Filter Algorithm for Wireless Capsule Endoscope Location Tracking”. In: *Proceedings of the 8th International Conference on Body Area Networks* (2013), pp. 536–540.

[65] T. Ito, T. Ogushi, and T. Hayashi. “Impulse-driven capsule by coil-induced magnetic field implementation”. In: *Mech. Mach. Theory* 45.11 (Nov. 2010), pp. 1642–1650.

[66] A. Jemal, M. M. Center, C. DeSantis, and E. M. Ward. “Global patterns of cancer incidence and mortality rates and trends”. In: *Cancer Epidemiology Biomarkers and Prevention* 19.8 (2010), pp. 1893–1907.

[67] A. M. Johansen. “SMCTC: sequential Monte Carlo in C++”. In: *Journal of Statistical Software* 30.6 (2009), pp. 1–41.

[68] E. Jones, T. Oliphant, P. Peterson, et al. *SciPy: Open source scientific tools for Python – Interpolation package.* 2001–. URL: `http://www.scipy.org/doc/scipy/reference/interpolate.html` (visited on 03/01/2016).

[69] N. Kameda, K. Higuchi, M. Shiba, H. Machida, H. Okazaki, H. Yamagami, T. Tanigawa, K. Watanabe, T. Watanabe, K. Tominaga, Y. Fujiwara, N. Oshitani, and T. Arakawa. “A prospective, single-blind trial comparing wireless capsule endoscopy and double-balloon enteroscopy in patients with obscure gastrointestinal bleeding”. In: *J. Gastroenterol.* 43.6 (2008), pp. 434–440.

[70] M. Kawasaki and R. Kohno. “Position estimation method of medical implanted devices using estimation of propagation velocity inside human body”. In: *IEICE Transactions on Communications* E92-B.2 (2009), pp. 403–409.

[71] H. Keller, A. Juloski, H. Kawano, M. Bechtold, A. Kimura, H. Takizawa, and R. Kuth. “Method for navigation and control of a magnetically guided capsule

endoscope in the human stomach". In: *2012 4th IEEE RAS/EMBS International Conference on Biomedical Robotics and Biomechatronics*. June 2012, pp. 859–865.

[72] B. Kim, S. Lee, J. H. Park, and J.-o. Park. "Inchworm-Like Microrobot for Capsule Endoscope". In: *2004 IEEE Int. Conf. Robot. Biomimetics* (2004), pp. 458–463.

[73] B. Kim, S. Park, C. Y. Jee, and S. J. Yoon. "An earthworm-like locomotive mechanism for capsule endoscopes". In: *2005 IEEE/RSJ Int. Conf. Intell. Robot. Syst. IROS* (2005), pp. 4092–4097.

[74] H. M. Kim, S. Yang, J. Kim, S. Park, J. H. Cho, J. Y. Park, T. S. Kim, E. S. Yoon, S. Y. Song, and S. Bang. "Active locomotion of a paddling-based capsule endoscope in an in vitro and in vivo experiment (with videos)". In: *Gastrointest. Endosc.* 72.2 (2010), pp. 381–387.

[75] M.-g. Kim, Y.-s. Hong, and E.-j. Lim. "Position and orientation detection of capsule endoscopes in spiral motion". In: *Int. J. Precis. Eng. Manuf.* 11.1 (Feb. 2010), pp. 31–37.

[76] J.-Y. Kim, Y.-C. Kwon, and Y.-S. Hong. "Automated alignment of rotating magnetic field for inducing a continuous spiral motion on a capsule endoscope with a twistable thread mechanism". In: *Int. J. Precis. Eng. Manuf.* 13.3 (Mar. 2012), pp. 371–377.

[77] G. Kósa, P. Jakab, F. Jólesz, and N. Hata. "Swimming capsule endoscope using static and RF magnetic field of MRI for propulsion". In: *Proc. - IEEE Int. Conf. Robot. Autom.* (2008), pp. 2922–2927.

[78] G. Kósa, P. Jakab, G. Székely, and N. Hata. "MRI driven magnetic microswimmers". In: *Biomed. Microdevices* 14.1 (Feb. 2012), pp. 165–178. arXiv: NIHMS150003.

[79] K. Kume, N. Sakai, and T. Goto. “Development of a novel endoscopic manipulation system: the Endoscopic Operation Robot ver.3”. In: *Endoscopy* 47.09 (Apr. 2015), pp. 815–819.

[80] M. P. Kummer, J. J. Abbott, B. E. Kratochvil, R. Borer, A. Sengul, and B. J. Nelson. “OctoMag: An Electromagnetic System for 5-DOF Wireless Micromanipulation”. In: *IEEE Transactions on Robotics* 26.6 (Dec. 2010), pp. 1006–1017.

[81] C. Lee, H. Choi, G. Go, H. Leon-Rodriguez, S. Jeong, K. Kwon, S. Y. Ko, J. O. Park, and S. Park. “Helical motion and 2D locomotion of magnetic capsule endoscope using precessional and gradient magnetic field”. In: *Proc. IEEE RAS EMBS Int. Conf. Biomed. Robot. Biomechatronics* (2014), pp. 1063–1067.

[82] J.-S. Lee, B. Kim, and Y.-S. Hong. “A flexible chain-based screw propeller for capsule endoscopes”. In: *Int. J. Precis. Eng. Manuf.* 10.4 (Oct. 2009), pp. 27–34.

[83] M. Li, S. Song, C. Hu, W. Yang, L. Wang, and M.-H. Meng. “A new calibration method for magnetic sensor array for tracking capsule endoscope”. In: *Robotics and Biomimetics (ROBIO), 2009 IEEE International Conference on* (2009), pp. 1561–1566.

[84] A. Liegeois. “Automatic supervisory control of the configuration and behavior of multibody mechanisms”. In: *IEEE Transactions on Systems, Man, and Cybernetics* 7.12 (1977), pp. 868–871.

[85] G. S. Lien, C. W. Liu, J. A. Jiang, C. L. Chuang, and M. T. Teng. “Magnetic control system targeted for capsule endoscopic operations in the stomach - Design, fabrication, and in vitro and ex vivo evaluations”. In: *IEEE Trans. Biomed. Eng.* 59.7 (2012), pp. 2068–2079.

[86] L. Liu, W. Liu, C. Hu, M. Q. Meng, Li Liu, Wei Liu, Chao Hu, and M. Q. Meng. "Hybrid magnetic and vision localization technique of capsule endoscope for 3D recovery of pathological tissues". In: *2011 9th World Congress on Intelligent Control and Automation*. IEEE, June 2011, pp. 1019–1023.

[87] W. Liu, C. Hu, Q. He, M. Q. Meng, and L. Liu. "An hybrid localization system based on optics and magnetics". In: *2010 IEEE International Conference on Robotics and Biomimetics, ROBIO 2010* (2010), pp. 1165–1169.

[88] A. Loeve, P. Breedveld, and J. Dankelman. "Scopes Too Flexible...and Too Stiff". In: *IEEE Pulse* 1.3 (2010), pp. 26–41.

[89] G. Lucarini, M. Mura, G. Ciuti, R. Rizzo, and A. Menciassi. "Electromagnetic Control System for Capsule Navigation: Novel Concept for Magnetic Capsule Maneuvering and Preliminary Study". In: *Journal of Medical and Biological Engineering* 35.4 (2015), pp. 428–436.

[90] A. W. Mahoney and J. J. Abbott. "Five-degree-of-freedom manipulation of an untethered magnetic device in fluid using a single permanent magnet with application in stomach capsule endoscopy". In: *The International Journal of Robotics Research* (2015), p. 19.

[91] A. W. Mahoney and J. J. Abbott. "Generating rotating magnetic fields with a single permanent magnet for propulsion of untethered magnetic devices in a Lumen". In: *IEEE Transactions on Robotics* 30.2 (2014).

[92] A. W. Mahoney, D. L. Cowan, K. M. Miller, and J. J. Abbott. "Control of untethered magnetically actuated tools using a rotating permanent magnet in any position". In: *2012 IEEE Int. Conf. Robot. Autom.* IEEE, May 2012, pp. 3375–3380.

[93] R. Mahony, T. Hamel, and J. M. Pflimlin. "Nonlinear complementary filters on the special orthogonal group". In: *IEEE Transactions on Automatic Control* 53.5 (2008), pp. 1203–1218.

[94] L. R. Maul and G. Alici. "A magnetically actuated endoscopic capsule robot based on a rolling locomotion mechanism". In: *2013 IEEE/ASME International Conference on Advanced Intelligent Mechatronics* (2013), pp. 50–55.

[95] a. Menciassi, C. Stefanini, S. Gorini, G. Pernorio, B. Kim, J. O. Park, and P. Dario. "Locomotion of a legged capsule in the gastrointestinal tract: theoretical study and preliminary technological results." In: *Conf. Proc. IEEE Eng. Med. Biol. Soc.* 4 (2004), pp. 2767–70.

[96] K. M. Miller, A. W. Mahoney, T. Schmid, and J. J. Abbott. "Proprioceptive magnetic-field sensing for closed-loop control of magnetic capsule endoscopes". In: *IEEE International Conference on Intelligent Robots and Systems* (Oct. 2012), pp. 1994–1999.

[97] Mingyuan Gao, Chengzhi Hu, Zhenzhi Chen, Honghai Zhang, and Sheng Liu. "Design and Fabrication of a Magnetic Propulsion System for Self-Propelled Capsule Endoscope". In: *IEEE Trans. Biomed. Eng.* 57.12 (Dec. 2010), pp. 2891–2902.

[98] E. Morita, N. Ohtsuka, Y. Shindo, S. Nouda, T. Kuramoto, T. Inoue, M. Murano, E. Umegaki, and K. Higuchi. "In vivo trial of a driving system for a self-propelling capsule endoscope using a magnetic field (with video)". In: *Gastrointest. Endosc.* 72.4 (2010), pp. 836–840.

[99] M. Mura, Y. Abu-Kheil, G. Ciuti, M. Visentini-Scarzanella, A. Menciassi, P. Dario, J. Dias, and L. Seneviratne. "Vision-based haptic feedback for capsule endoscopy navigation: a proof of concept". In: *Journal of Micro-Bio Robotics* 11.1-4 (2016), pp. 35–45.

[100] R. M. Murray, Z. Li, and S. S. Sastry. *A Mathematical Introduction to Robotic Manipulation*. Boca Raton, FL, USA: CRC Press, Inc., 1994, p. 480.

[101] A. R. Nafchi, S. T. Goh, and S. A. Zekavat. "High performance DOA/TOA-based Endoscopy Capsule localization and tracking via 2D circular arrays and inertial measurement unit". In: *IEEE International Conference on Wireless for Space and Extreme Environments, WiSEE 2013 - Conference Proceedings* (2013), pp. 1–6.

[102] NDI Medical. *NDI Aurora*. 2017. URL: `https://www.ndigital.com/medical/products/aurora/`.

[103] K. L. Obstein and P. Valdastri. "Advanced endoscopic technologies for colorectal cancer screening". In: *World J. Gastroenterol.* 19.4 (2013), pp. 431–439.

[104] OpenMP Architecture Review Board. *OpenMP Application Program Interface Version 3.1*. July 2011. URL: `www.openmp.org/wp-content/uploads/OpenMP3.1.pdf`.

[105] E. Paperno, I. Sasada, and E. Leonovich. "A new method for magnetic position and orientation tracking". In: *IEEE Transactions on Magnetics* 37.4 I (2001), pp. 1938–1940.

[106] H. Park, S. Park, E. Yoon, B. Kim, J. Park, and S. Park. "Paddling based Microrobot for Capsule Endoscopes". In: *Proc. 2007 IEEE Int. Conf. Robot. Autom.* IEEE, Apr. 2007, pp. 3377–3382.

[107] A. J. Petruska and J. J. Abbott. "Omnimagnet: An Omnidirectional Electromagnet for Controlled Dipole-Field Generation". In: *IEEE Transactions on Magnetics* 50.7 (July 2014), pp. 1–10.

[108] A. J. Petruska and J. J. Abbott. "Optimal permanent-magnet geometries for dipole field approximation". In: *IEEE Transactions on Magnetics* 49.2 (2013), pp. 811–819.

[109] A. J. Petruska and B. J. Nelson. "Minimum Bounds on the Number of Electromagnets Required for Remote Magnetic Manipulation". In: *IEEE Transactions on Robotics* 31.3 (June 2015), pp. 714–722.

[110] B. V. Pham, G. S. Raju, I. Ahmed, D. Brining, S. Chung, P. Cotton, C. J. Gostout, R. H. Hawes, A. N. Kalloo, S. V. Kantsevoy, and P. J. Pasricha. "Immediate endoscopic closure of colon perforation by using a prototype endoscopic suturing device: feasibility and outcome in a porcine model (with video){A figure is presented}". In: *Gastrointest. Endosc.* 64.1 (2006), pp. 113–119.

[111] D. Pham and S. M. Aziz. "A Real-Time Localization System for an Endoscopic Capsule Using Magnetic Sensors". In: *Sensors* 14.11 (Nov. 2014), pp. 20910–20929.

[112] L. Phee, D. Accoto, A. Menciassi, C. Stefanini, M. C. Carrozza, and P. Dario. "Analysis and development of locomotion devices for the gastrointestinal tract". In: *IEEE Transactions on Biomedical Engineering* 49.6 (2002), pp. 613–616.

[113] A. Plotkin and E. Paperno. "3-D Magnetic Tracking of a Single Subminiature Coil with a Large 2-D Array of Uniaxial Transmitters". In: *IEEE Transactions on Magnetics* 39.5 II (2003), pp. 3295–3297.

[114] K. M. Popek and J. J. Abbott. "6-D Localization of a Magnetic Capsule Endoscope Using a Stationary Rotating Magnetic Dipole Field". In: *Hamlyn Symposium on Medical Robotics* (2015), pp. 47–48.

[115] K. M. Popek, T. Hermans, and J. J. Abbott. "First demonstration of simultaneous localization and propulsion of a magnetic capsule in a lumen using a single rotating magnet". In: *2017 IEEE Int. Conf. Robot. Autom.* IEEE, May 2017, pp. 1154–1160.

[116] K. M. Popek, A. W. Mahoney, and J. J. Abbott. “Localization method for a magnetic capsule endoscope propelled by a rotating magnetic dipole field”. In: *2013 IEEE International Conference on Robotics and Automation* (2013), pp. 5348–5353.

[117] K. M. Popek, T. Schmid, and J. J. Abbott. “Six-Degree-of-Freedom Localization of an Untethered Magnetic Capsule Using a Single Rotating Magnetic Dipole”. In: *IEEE Robotics and Automation Letters* 2.1 (Jan. 2017), pp. 305–312.

[118] M. Pourhomayoun, Z. Jin, and M. L. Fowler. “Accurate localization of in-body medical implants based on spatial sparsity”. In: *IEEE Transactions on Biomedical Engineering* 61.2 (2014), pp. 590–597.

[119] H. J. M. Pullens, N. van der Stap, E. D. Rozeboom, M. P. Schwartz, F. van der Heijden, M. G. H. van Oijen, P. D. Siersema, and I. A. M. J. Broeders. “Colonoscopy with robotic steering and automated lumen centralization: a feasibility study in a colon model”. In: *Endoscopy* (2015), pp. 286–290.

[120] M. Quigley, K. Conley, B. Gerkey, J. Faust, T. Foote, J. Leibs, R. Wheeler, and A. Y. Ng. “ROS: an open-source Robot Operating System”. In: *ICRA Workshop Open Source Software*. Vol. 3. 3.2. 2009.

[121] M. Quirini, S. Scapellato, P. Valdastri, A. Menciassi, and P. Dario. “An approach to capsular endoscopy with active motion”. In: *Annu. Int. Conf. IEEE Eng. Med. Biol. - Proc.* 2007, pp. 2827–2830.

[122] T. Rösch, A. Adler, H. Pohl, E. Wettschureck, M. Koch, B. Wiedenmann, and N. Hoepffner. “A motor-driven single-use colonoscope controlled with a hand-held device: a feasibility study in volunteers”. In: *Gastrointestinal Endoscopy* 67.7 (2008), pp. 1139–1146.

[123] J. Ruiter, E. Rozeboom, M. Van Der Voort, M. Bonnema, and I. Broeders. "Design and evaluation of robotic steering of a flexible endoscope". In: *Proceedings of the IEEE RAS and EMBS International Conference on Biomedical Robotics and Biomechatronics* (2012), pp. 761–767.

[124] P. Ryan and E. Diller. "Five-degree-of-freedom magnetic control of microrobots using rotating permanent magnets". In: *2016 IEEE International Conference on Robotics and Automation (ICRA)*. May 2016, pp. 1731–1736.

[125] S. Saha, Y. Boers, H. Driessen, P. Mandal, and a. Bagchi. "Particle based MAP state estimation: A comparison". In: *2009 12th International Conference on Information Fusion* (2009), pp. 278–283.

[126] M. Salerno, R. Rizzo, E. Sinibaldi, and A. Menciassi. "Force calculation for localized magnetic driven capsule endoscopes". In: *IEEE International Conference on Robotics and Automation*. 2013, pp. 5354–5359.

[127] M. Salerno, G. Ciuti, G. Lucarini, R. Rizzo, P. Valdastri, A. Menciassi, A. Landi, and P. Dario. "A discrete-time localization method for capsule endoscopy based on on-board magnetic sensing". In: *Measurement Science and Technology* 23.1 (Jan. 2012), p. 015701.

[128] D. E. Schinstock, T. N. Faddis, and R. B. Greenway. "Robust inverse kinematics using damped least squares with dynamic weighting". In: *NASA. Johnson Space Center, Conference on Intelligent Robotics in Field, Factory, Service and Space*. Vol. 2. 1994.

[129] V. Schlageter, P. A. Besse, R. S. Popovic, and P. Kucera. "Tracking system with five degrees of freedom using a 2D-array of Hall sensors and a permanent magnet". In: *Sensors and Actuators, A: Physical* 92.1-3 (2001), pp. 37–42.

[130] J. Schulman, Y. Duan, J. Ho, A. Lee, I. Awwal, H. Bradlow, J. Pan, S. Patil, K. Goldberg, and P. Abbeel. "Motion planning with sequential convex optimization and convex collision checking". In: *International Journal of Robotics Research* 33.9 (2014), pp. 1251–1270.

[131] M. Sendoh, K. Ishiyama, and K. I. Arai. "Fabrication of Magnetic Actuator for Use in a Capsule Endoscope". In: *IEEE Transactions on Magnetics* 39.5 II (2003), pp. 3232–3234.

[132] P. K. Sharma and S. K. Guha. "Transmission of time varying magnetic field through body tissue". In: *Journal of Biological Physics* 3.2 (1975), pp. 95–102.

[133] A. K. Shergill, K. R. McQuaid, and D. Rempel. "Ergonomics and GI endoscopy". In: *Gastrointest. Endosc.* 70.1 (July 2009), pp. 145–153.

[134] R. L. Siegel, K. D. Miller, and A. Jemal. "Cancer statistics". In: *CA: A Cancer Journal for Clinicians* 66.1 (2016), pp. 7–30.

[135] M. Simi, P. Valdastri, C. Quaglia, A. Menciassi, and P. Dario. "Design, Fabrication, and Testing of a Capsule With Hybrid Locomotion for Gastrointestinal Tract Exploration". In: *IEEE/ASME Trans. Mechatronics* 15.2 (Apr. 2010), pp. 170–180.

[136] P. R. Slawinski, K. L. Obstein, and P. Valdastri. "Capsule endoscopy of the future: What's on the horizon?" In: *World J. Gastroenterol.* 21.37 (2015), pp. 10528–10541.

[137] P. R. Slawinski, K. L. Obstein, and P. Valdastri. "Emerging issues and future developments in capsule endoscopy". In: *Techniques in Gastrointestinal Endoscopy* 17.1 (2015), pp. 40–46.

[138] P. R. Slawinski, A. Z. Taddese, K. B. Musto, K. L. Obstein, and P. Valdastri. "Autonomous Retroflexion of a Magnetic Flexible Endoscope". In: *IEEE Robotics and Automation Letters* 2.3 (July 2017), pp. 1352–1359.

[139] L. J. Sliker and G. Ciuti. “Flexible and capsule endoscopy for screening, diagnosis and treatment”. In: *Expert Review of Medical Devices* 11.6 (2014), pp. 649–666.

[140] L. Sliker, G. Ciuti, M. Rentschler, and A. Menciassi. “Magnetically driven medical devices: a review”. In: *Expert Review of Medical Devices* 12.6 (2015), pp. 737–752.

[141] R. Smith. *Open Dynamics Engine ODE*. May 2018. URL: `https://www.ode.org`.

[142] D. Son, S. Yim, and M. Sitti. “A 5-D Localization Method for a Magnetically Manipulated Untethered Robot using a 2-D Array of Hall-effect Sensors”. In: *Mechatronics, IEEE/ASME Transactions on* PP.99 (2015), p. 1.

[143] S. Song, C. Hu, M. Li, W. Yang, and M. Q. Meng. “Real time algorithm for magnet’s localization in capsule endoscope”. In: *2009 IEEE International Conference on Automation and Logistics*. IEEE, Aug. 2009, pp. 2030–2035.

[144] S. Song, B. Li, W. Qiao, C. Hu, H. Ren, H. Yu, Q. Zhang, M. Q. H. Meng, and G. Xu. “6-D magnetic localization and orientation method for an annular magnet based on a closed-form analytical model”. In: *IEEE Transactions on Magnetics* 50.9 (2014).

[145] S. Song, X. Qiu, J. Wang, and M. Q. Meng. “Real-Time Tracking and Navigation for Magnetically Manipulated Untethered Robot”. In: *IEEE Access* 4 (2016), pp. 7104–7110.

[146] STMicroelectronics. *AN4508: Parameters and calibration of a low-g 3-axis accelerometer*. URL: `www.st.com/resource/en/application_note/dm00119044.pdf` (visited on 06/05/2018).

[147] Z.-J. Sun, X.-G. Cheng, S. Cao, B. Ye, H.-H. Zhang, and S. Liu. "Multi-applications of a magnet configuration in actuating capsule endoscope". In: *2014 IEEE/ASME Int. Conf. Adv. Intell. Mechatronics*. Besançon, France: IEEE, July 2014, pp. 106–111.

[148] P. Swain. "Wireless capsule endoscopy". In: *Gut* 52.90004 (June 2003), pp. 48iv–50.

[149] P. Swain, A. Toor, F. Volke, J. Keller, J. Gerber, E. Rabinovitz, and R. I. Rothstein. "Remote magnetic manipulation of a wireless capsule endoscope in the esophagus and stomach of humans (with videos)". In: *Gastrointest. Endosc.* 71.7 (2010), pp. 1290–1293.

[150] A. Z. Taddese. *STORM Lab Gazebo magnet plugin*. May 2018. URL: `https://github.com/vustormlab/storm_gazebo_ros_magnet`.

[151] A. Z. Taddese, P. R. Slawinski, K. L. Obstein, and P. Valdastri. "Closed Loop Control of a Tethered Magnetic Capsule Endoscope". In: *Robotics: Science and Systems XII*. Vol. 12. June 2016, p. 380.

[152] A. Z. Taddese, P. R. Slawinski, K. L. Obstein, and P. Valdastri. "Nonholonomic closed-loop velocity control of a soft-tethered magnetic capsule endoscope". In: *2016 IEEE/RSJ International Conference on Intelligent Robots and Systems (IROS)*. Daejeon, South Korea: IEEE, Oct. 2016, pp. 1139–1144.

[153] S. Tamaz, R. Gourdeau, A. Chanu, J. B. Mathieu, and S. Martel. "Real-time MRI-based control of a ferromagnetic core for endovascular navigation". In: *IEEE Trans. Biomed. Eng.* 55.7 (2008), pp. 1854–1863.

[154] T. D. Than, G. Alici, S. Harvey, G. O'Keefe, H. Zhou, W. Li, T. Cook, and S. Alam-Fotias. "An effective localization method for robotic endoscopic capsules using multiple positron emission markers". In: *IEEE Transactions on Robotics* 30.5 (2014), pp. 1174–1186.

[155] T. D. Than, G. Alici, H. Zhou, and W. Li. "A review of localization systems for robotic endoscopic capsules". In: *IEEE Transactions Biomededical Engineering* 59.9 (Sept. 2012), pp. 2387–2399.

[156] J. L. Toennies, G. Tortora, M. Simi, P. Valdastri, and R. J. Webster. "Swallowable medical devices for diagnosis and surgery: the state of the art". In: *Proc. Inst. Mech. Eng. Part C J. Mech. Eng. Sci.* 224.7 (Jan. 2010), pp. 1397–1414.

[157] L. A. Torre, F. Bray, R. L. Siegel, J. Ferlay, J. Lortet-tieulent, and A. Jemal. "Global Cancer Statistics, 2012". In: *CA: A Cancer Journal for Clinicians* 65.2 (2015), pp. 87–108.

[158] G. Tortora, P. Valdastri, E. Susilo, A. Menciassi, P. Dario, F. Rieber, and M. O. Schurr. "Propeller-based wireless device for active capsular endoscopy in the gastric district." In: *Minim. Invasive Ther. Allied Technol.* 18.5 (Jan. 2009), pp. 280–90.

[159] J. Tugwell, P. Brennan, C. O'Shea, K. O'Donoghue, T. Power, M. O'Shea, J. Griffiths, R. Cahill, and P. Cantillon-Murphy. "Electropermanent magnetic anchoring for surgery and endoscopy". In: *IEEE Transactions on Biomededical Engineering* 62.3 (2015), pp. 842–848.

[160] E. Tumino, G. Parisi, M. Bertoni, M. Bertini, S. Metrangolo, E. Ierardi, R. Cervelli, G. Bresci, and R. Sacco. "Use of robotic colonoscopy in patients with previous incomplete colonoscopy". In: *Eur Rev Med Pharmacol Sci* 21.4 (2017), pp. 819–826.

[161] E. Tumino, R. Sacco, M. Bertini, M. Bertoni, G. Parisi, and A. Capria. "Endotics system vs colonoscopy for the detection of polyps." In: *World journal of gastroenterology* 16.43 (Nov. 2010), pp. 5452–6.

[162] M. Turan, Y. Almalioglu, H. Araujo, E. Konukoglu, and M. Sitti. "A non-rigid map fusion-based direct SLAM method for endoscopic capsule robots".

In: *International Journal of Intelligent Robotics and Applications* 1.4 (Dec. 2017), pp. 399–409.

[163] C. Turner. "Recursive discrete-time sinusoidal oscillators". In: *IEEE Signal Processing Magazine* 20.3 (May 2003), pp. 103–111.

[164] P. Valdastri, G. Ciuti, A. Verbeni, A. Menciassi, P. Dario, A. Arezzo, and M. Morino. "Magnetic air capsule robotic system: proof of concept of a novel approach for painless colonoscopy". In: *Surgical Endoscopy* 26.5 (May 2012), pp. 1238–1246.

[165] P. Valdastri, M. Simi, and R. J. Webster III. "Advanced technologies for gastrointestinal endoscopy". In: *Annual Review of Biomedical Engineering* 14 (2012), pp. 397–429.

[166] P. Valdastri, R. Webster, C. Quaglia, M. Quirini, A. Menciassi, and P. Dario. "A New Mechanism for Mesoscale Legged Locomotion in Compliant Tubular Environments". In: *IEEE Trans. Robot.* 25.5 (Oct. 2009), pp. 1047–1057.

[167] D. Vázquez, J. Bernal, F. J. Sánchez, G. Fernández-Esparrach, A. M. López, A. Romero, M. Drozdzal, and A. Courville. "A Benchmark for Endoluminal Scene Segmentation of Colonoscopy Images". In: *Journal of healthcare engineering* 2017 (2017).

[168] F. Volke, J. Keller, A. Schneider, J. Gerber, M. Reimann-Zawadzki, E. Rabinovitz, C. a. Mosse, and P. Swain. "In-Vivo Remote Manipulation of Modified Capsule Endoscopes Using An External Magnetic Field". In: *Gastrointest. Endosc.* 67.5 (Apr. 2008), AB121–AB122.

[169] B. Vucelic, D. Rex, R. Pulanic, J. Pfefer, I. Hrstic, B. Levin, Z. Halpern, and N. Arber. "The Aer-O-Scope: Proof of concept of a pneumatic, skill-independent, self-propelling, self-navigating colonoscope". In: *Gastroenterology* 130.3 (2006), pp. 672–677.

[170] X. Wang and M. Q. H. Meng. "An inchworm-like locomotion mechanism based on magnetic actuator for active capsule endoscope". In: *IEEE Int. Conf. Intell. Robot. Syst.* (2006), pp. 1267–1272.

[171] X. Wang, M. Q. H. Meng, and X. Chen. "A locomotion mechanism with external magnetic guidance for active capsule endoscope". In: *2010 Annual International Conference of the IEEE Engineering in Medicine and Biology*. Aug. 2010, pp. 4375–4378.

[172] Y. Wang, R. Fu, Y. Ye, U. Khan, and K. Pahlavan. "Performance bounds for RF positioning of endoscopy camera capsules". In: *2011 IEEE Radio and Wireless Week, RWW 2011 - 2011 IEEE Topical Conference on Biomedical Wireless Technologies, Networks, and Sensing Systems, BioWireleSS 2011* (2011), pp. 71–74.

[173] W. Weitschies, R. Kötitz, D. Cordini, and L. Trahms. "High-resolution monitoring of the gastrointestinal transit of a magnetically marked capsule". In: *Journal of Pharmaceutical Sciences* 86.11 (1997), pp. 1218–1222.

[174] K. J. Wernli, A. T. Brenner, C. M. Rutter, and J. M. Inadomi. "Risks Associated with Anesthesia Services during Colonoscopy". In: *Gastroenterology* 150.4 (2016), pp. 888–894. arXiv: 15334406.

[175] X. Wu, W. Hou, C. Peng, X. Zheng, X. Fang, and J. He. "Wearable magnetic locating and tracking system for MEMS medical capsule". In: *Sensors and Actuators, A: Physical* 141.2 (2008), pp. 432–439.

[176] W. Yang, C. Hu, M. Q. Meng, S. Song, and H. Dai. "A six-dimensional magnetic localization algorithm for a rectangular magnet objective based on a particle swarm optimizer". In: *IEEE Transactions on Magnetics* 45.8 (2009), pp. 3092–3099.

[177] B. Ye, W. Zhang, Z. J. Sun, L. Guo, C. Deng, Y. Q. Chen, H. H. Zhang, and S. Liu. "Study on a magnetic spiral-type wireless capsule endoscope controlled by rotational external permanent magnet". In: *Journal of Magnetism and Magnetic Materials* 395 (2015), pp. 316–323.

[178] B. P. M. Yeung and P. W. Y. Chiu. "Application of robotics in gastrointestinal endoscopy: A review". In: *World J. Gastroenterol.* 22.5 (2016), pp. 1811–1825.

[179] S. Yim and M. Sitti. "Design and analysis of a magnetically actuated and compliant capsule endoscopic robot". In: *Proc. - IEEE Int. Conf. Robot. Autom.* (2011), pp. 4810–4815.